

2006

Computation of electromagnetic backscattered field with the coupling of aerodynamic performance in a multidisciplinary design optimization of aircraft

Seng Muy Hong
University of Dayton

Follow this and additional works at: https://ecommons.udayton.edu/graduate_theses

Recommended Citation

Hong, Seng Muy, "Computation of electromagnetic backscattered field with the coupling of aerodynamic performance in a multidisciplinary design optimization of aircraft" (2006). *Graduate Theses and Dissertations*. 3359.

https://ecommons.udayton.edu/graduate_theses/3359

This Dissertation is brought to you for free and open access by the Theses and Dissertations at eCommons. It has been accepted for inclusion in Graduate Theses and Dissertations by an authorized administrator of eCommons. For more information, please contact mschlange1@udayton.edu, ecommons@udayton.edu.

COMPUTATION OF ELECTROMAGNETIC
BACKSCATTERED FIELD WITH THE COUPLING OF
AERODYNAMIC PERFORMANCE IN A
MULTIDISCIPLINARY DESIGN OPTIMIZATION OF
AIRCRAFT

DISSERTATION

Submitted to
the Engineering School of the
UNIVERSITY OF DAYTON

In Partial Fulfillment of the Requirements for
The Degree
Doctor of Philosophy in Electrical Engineering

by

Seng Muy Hong, B.S., M.S.

UNIVERSITY OF DAYTON

Dayton, Ohio

May 2006

COMPUTATION OF ELECTROMAGNETIC BACKSCATTERED FIELD
WITH THE COUPLING OF AERODYNAMIC PERFORMANCE IN A
MULTIDISCIPLINARY DESIGN OPTIMIZATION OF AIRCRAFT

APPROVED BY:



Dr. Gary A. Thiele, PhD.
Adviser Committee Chairman
Professor, Department of Electrical
and Computer Engineering



Dr. Robert P. Penno, PhD.
Committee Member, Co-Chair
Associate Professor, Department
of Electrical and Computer
Engineering



Dr. Krishna M. Pasala, PhD.
Committee Member
Professor, Department of Electrical
and Computer Engineering



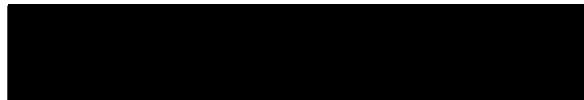
Prof. Gerald Shaughnessy
Committee Member
Associate Professor, Department
of Mathematics



Dr. Vipperla B. Venkayya, PhD.
Committee Member
Principal Scientist, Emeritus
Air Vehicle Directorate
Air Force Research Laboratory,
WPAFB



Dr. Donald L. Moon, PhD.
Associate Dean, Graduate
Engineering Programs and
Research
School of Engineering



Dr. Joseph E. Saliba, PhD., P.E.
Dean, School of Engineering

© Copyright by

Seng Muy Hong

2006

ABSTRACT

COMPUTATION OF ELECTROMAGNETIC BACKSCATTERED FIELD WITH
THE COUPLING OF AERODYNAMIC PERFORMANCE IN A
MULTIDISCIPLINARY DESIGN OPTIMIZATION OF AIRCRAFT

Name: Hong, Seng Muy

University of Dayton

Advisor: Gary A. Thiele, Ph.D.

The computation or prediction of plane wave scattering widths is one of the major design considerations of future aircraft and weapon systems. The control of scattering and penetration of electromagnetic waves is the primary objective of emerging low observable technology. The task in computing the electromagnetic backscattered field of an airframe structure is by no means a new endeavor. Whereas predicting a minimal backscattered field return under the manipulation of airframe geometry in the context of multidisciplinary design is considered the most prudent approach to obtain the optimal solution. The objective of this paper is to develop a mathematical method to couple the backscattered field with the defined aerodynamic performance constraints in the design process of future airframes.

This paper will address the basic concept of integrating the radio frequency (RF) backscattered field or electromagnetic (EM) discipline with the Multidisciplinary Design Optimization (MDO) methodology. The development of the MDO system is complex and the result appears to be intractable and time consuming despite the availability of high-speed super computers. Due to the fact that many disciplines and analyses were implemented with various optimization methods and techniques, such as the Finite Element Method (FEM), Method of Moment (MoM), the Finite Difference Time Domain (FDTD) method, the integration of multiple individual disciplines with various software coding formats would be the most difficult task. In spite of this expected challenge, this paper will address:

- a) The effects and benefits of employing the EM discipline in MDO systems in preliminary configuration design of aircraft structure.

- b) The criteria to minimize backscattered field return while maximizing aerodynamic performance and the methods of optimization, trade-off, and implementation.

- c) The integration issue of electromagnetic discipline into the grand scheme of MDO. Furthermore, this paper explores the techniques or approaches that facilitate a minimum return of backscattered field while satisfying the constraints imposed by the aerodynamics performance.

I dedicate this dissertation to those who seek knowledge, understanding, and wisdom, all things are possible to those who first seek out the purpose in life and hold on to the hope for it nurtures courage.

"It takes courage to be a refugee. Courage not to give up hope and to make the most of the hand that has been dealt. Courage to start a new life against daunting odds, eventually to become contributing and enriching members of society once more."

-the United Nations High Commissioner for Refugees

ACKNOWLEDGEMENTS

It has been a long journey in completing this research and I am grateful for the opportunity that many would deem impossible. As a refugee from Cambodia, I came to United States in August 1979 with six years of formal education and English was the last language I learned.

My heartfelt appreciation goes to my advisor and committee chair, Prof. Gary Thiele and advisor Dr. Bob Penno for their insightful guidance, encouragement, and constant source of advice. I am deeply indebted to Prof. Thiele, whom even after this retirement, continues to guide and provide helpful insights. This research could not have been accomplished without the spiritual encouragement from Dr. Penno, and I am forever thankful. I would like to thank the committee members, Dr. Krishna Pasala, Prof. Gerald Shaughnessy, Dr. Vipperla Venkayya, for their patience and constancy through this journey, especially to Dr. Donald Moon for his support and understanding, and Marilyn Knisley for her timely assistant.

This research was conducted concurrently with my previous full time employment as a defense contractor and current position as a research engineer at Air Force Research Laboratory (AFRL), Wright-Patterson Air Force Base. I could not have done without many support and encouragement from my colleagues and managements. I would like to thank Dr. Donald Hanson (former Director of Sensors Directorate) for his provision in allotting time away for me to work off-site and

concentrate on my research. His words of inspiration and belief have been and will be treasured. Much appreciation to the AFRL Sensors Directorate (SN) Director Mr. Joe Sciabica, Radio Frequency Sensor Technology (SNR) Division Chief, Mr. Bill Moore, and the Branch management team: Mr. Anton (Mike) Gardner, Ms. Denice Jacobs, and Mr. Tracy Johnston for their support and stimulus of this research. Many thanks extended to Radio Frequency Countermeasures Test Facility (RFCTF) staff members for their encouragement, especially, Maj. Abel Nunez for his insightful discussion, proofreading, and document formatting; and Lt. John Glett for his suggestions, thorough and timely proofreading. I am grateful to my colleagues, Mr. Bob Kissell and Mr. Bob McRaven, for their intriguing "think outside the box" and "what if" scenario discussions at numerous lunch-hours that led to the mutation concept; Mr. Boyd Norris for his remarks on real-life facts that prompted my course of action, rather than conforming to the norm.

My earnest appreciation goes to Dr. Charles Brown and Mr. John MacAulay (co-founders of MacAulay-Brown, Inc.) for their vision in academic pursuit and educational funding support in graduate studies. I am grateful for having the opportunity and privilege as a Dayton Area Graduate Studies Institute (DAGSI) scholarship recipient. I applaud DAGSI's mission "to increase and improve the quantity and quality of graduate educational and research opportunities", and University of Dayton in providing the nurturing environment.

I would like to thank my tutors: Donna Cunningham, Nancy Mitchell, Martha Kirby, Darlene Bane, Bert Haaga, and Mary Stringer for they had overcome the challenge in teaching me English by drawing and hand expression. To the owner & operator of former Southern Orchards, Inc., Edward & Edna Joy Prisock, I would

like to acknowledge that it was the Prisock who registered and paid for the English as Second Language (ESL) course at Mississippi State University (MSU) in spring of 1980, and subsequently received my GED diploma in June 1981. There are no better friends who seek out the best in others and speak with truth without reservation. Ed's belief in me and his remark "Can't is not in Seng's vocabulary" paved the way in receiving my BSEE from MSU in 1985. Obviously I would not be here, or writing this acknowledgement without my sponsors, Dr. & Mrs. Roland Byrd and Mr. & Mrs. Donald McNeill for they sponsored us from Refugee Camp in Thailand. My wife and I, will forever be grateful for they took us as strangers into their home, showered us with their southern hospitality, and taught us English and consequently, were responsible for my southern drawl... and what I have become. To Mr. & Mrs. John Randle, the guardians to my family, for their love and wise council; I draw my strength from their Christian walk and kindness, and much more... For them I thank God.

Education improves a person's understanding and knowledge, but family nurtures the soul and well being. I could not have done this work without the support of my wife, Kim, my son Fulter, and my daughter Amanda. Their love and understanding are a source of comfort and encouragement. Time is of essence an asset many may overlook or fail to cherish. Most of all, I thank God for His provision to my family far and near, and our children for they are healthy and "perfect" since both of them are now away from home and attending college. Yes, this has been a long journey, yet a rewarding one as I have been surrounded by many caring people for whom I have so much to be thankful for.

TABLE OF CONTENTS

	Page
Abstract	iii
List of Tables	xi
List of Figures	xii
Chapters:	
1. Introduction	1
1.1 EARLY RESEARCH ON MULTIDISCIPLINARY DESIGN OPTI- MIZATION	3
1.2 INTEGRATION OF MULTIDISCIPLINARY DESIGN OPTIMIZA- TION	4
2. MULTIDISCIPLINARY DESIGN OPTIMIZATION OVERVIEW	7
2.1 STOCHASTIC MUTATION ALGORITHM MULTIDISCIPLINARY OPTIMIZATION CONCEPT	9
2.2 BASIC CONCEPTS IN MULTIDISCIPLINARY DESIGN OPTI- MIZATION FOR PRELIMINARY DESIGN	12
3. ELECTROMAGNETIC SCATTERING FIELDS COMPUTATIONAL AP- PROACHES AND APPROXIMATION METHODS	16
3.1 INTRODUCTION	16
3.1.1 NUMERICAL METHODS	16
3.1.2 METHOD OF MOMENTS	17
3.1.3 FINITE DIFFERENCE TIME DOMAIN	17
3.1.4 FINITE ELEMENTS	18
3.2 ASYMPTOTIC METHODS	19
3.2.1 PHYSICAL OPTICS AND PHYSICAL THEORY OF DIFFRAC- TION APPROACH	19

3.2.2	GEOMETRICAL OPTICS AND GEOMETRICAL THEORY OF DIFFRACTION APPROACH	20
3.2.3	UNIFORM THEORY OF DIFFRACTION APPROACH . .	21
4.	BACKSCATTER COMPUTATION METHOD	22
4.1	UNIFORM THEORY OF DIFFRACTION	29
4.2	BACKSCATTERED RETURN OF PLATE	32
5.	WING OF FINITE PLANFORM	43
5.1	LIFT COEFFICIENT	45
5.2	DRAG COEFFICIENT	47
5.3	LIFT DISTRIBUTION OF A FINITE WING PLANFORM	50
5.4	LIFT AND DRAG ANALYSIS	53
6.	DESIGN OPTIMIZATION IN COUPLING AERO AND ELECTROMAG- NETIC DISCIPLINES	64
6.1	MODELS CRITERIA IN AERODYNAMIC AND ELECTROMAG- NETIC DISCIPLINES	69
6.2	COMPUTATIONAL DATA OF A RECTANGULAR WING PLAN- FORM	72
6.3	COMPUTATIONAL DATA OF A TAPERED WING PLANFORM	104
7.	CONCLUSION AND ADDITIONAL RESEARCH	131
7.1	CHALLENGES	135
7.2	CONTRIBUTIONS	137
Appendices:		
A.	SOFTWARE CODES	139
A.1	Fresnel Integral	139
A.2	Induced Drag Factor	140
A.3	Geometrical Optics / Geometrical Theory of Diffraction	142
	Bibliography	144
	Vita	154

LIST OF TABLES

Table	Page
5.1 C_ℓ as Function of α for $AR = 2$ and $\alpha_{lo} = -1.2^\circ$	55
5.2 C_ℓ as Function of AR for $\alpha = 5^\circ$ and $\alpha_{lo} = -1.2^\circ$	56
6.1 Control Parameters of a Rectangular Wing Optimization: RectProb- Set1	78
6.2 Computed MDO Data of Table 6.1 Controlled Parameters	87
6.3 Control Parameters of a Rectangular Wing Optimization: RectProb- Set2	89
6.4 Computed MDO Data of Table 6.3 Controlled Parameters	95
6.5 Control Parameters of a Rectangular Wing Optimization: RectProb- Set3	97
6.6 Computed MDO Data of Table 6.5 Controlled Parameters	105
6.7 Control Parameters of a Tapered Wing Optimization: TapProbSet1 .	108
6.8 Simulated Tapered Wing Data of TapProbSet1 (Table 6.7)	113
6.9 Control Parameters of a Tapered Wing Optimization: TapProbSet2 .	116
6.10 Simulated Tapered Wing Data of TapProbSet2 (Table 6.9)	122
6.11 Control Parameters of a Tapered Wing Optimization: TapProbSet3 .	123
6.12 Simulated Tapered Wing Data of TapProbSet3 (Table 6.11)	130

LIST OF FIGURES

Figure	Page
2.1 Stochastic Mutation Algorithm MDO Block Diagram	10
2.2 Multidisciplinary design optimization elements interaction	12
2.3 Backscattered field return contributors	14
4.1 Surface current of an edge shape body	23
4.2 Field Regions of a Conducting Wedge	24
4.3 Diffracted fields in the shadow boundary (SB)	27
4.4 Total field of a conducting Half-Plane	28
4.5 Fresnel magnitude and phase transition function	31
4.6 Backscattered field of an infinite strip	32
4.7 Scattering width of an infinite strip (Vertical-Pol)	35
4.8 Scattering Width of an infinite Strip (Horizontal-Pol)	36
4.9 Backscattered echo width of an infinite strip	37
4.10 A finite rectangular flat plate target	38
4.11 Backscattered field of a rectangular plate	39
4.12 Diffractive field of a flat plate (a) Single Order; (b)&(c): 1st order multiple; (d)&(e): 2nd order multiple	40
4.13 Backscattered return of a 6.5 x 6.5 inch flat plate [1]	41
4.14 Backscattered return of a 6.5 x 6.5 inch flat plate (Vertical Pol.) . .	41
4.15 Backscattered width of a 6.5 x 6.5 inch flat plate (Horizontal Pol.) .	42
5.1 Various geometric wing planforms	44
5.2 Rectangular wing spanwise distribution	45
5.3 Symmetric spanwise lift distribution presented by a Fourier Sine series [2]	46
5.4 Induced flow on a finite wing	48
5.5 Simple geometry Illustrating Lift Force of an aeroplane	50
5.6 Linearly Tapered Wing	52
5.7 NASA FoilSim II Simulator Data Display	54
5.8 Theoretical and experimental C_l as function of α of unswept tapered wing [2]	57
5.9 Theoretical and measured C_l as function of C_d of unswept tapered wing [2]	57
5.10 Calculated C_l as function of α of unswept tapered wing [3]	58

5.11	Calculated C_l as function of C_d of unswept tapered wing [3]	58
5.12	Computed lift coefficients of unswept tapered wing	59
5.13	Computed induced drag coefficients of unswept tapered wing	59
5.14	Numerical induced drag factor for a linearly tapered wing [4]	60
5.15	Computed induced drag factor of a tapered wing	61
5.16	Computed induced drag C_d as function of lift C_l and aspect ratio of tapered wing	62
5.17	Theoretical induced drag C_d variation with lift C_l and wing aspect ratio	63
6.1	Stochastic Mutation Algorithm Optimization state flow	66
6.2	Stochastic Mutation Algorithm Optimization decision tree flow	67
6.3	Modal of a zeroth (0^{th}) order mode wing planform	71
6.4	Low aspect ratio of a finite thin rectangular wing	73
6.5	High aspect ratio of a finite thin rectangular wing	74
6.6	$C_l - \alpha$ curve of infinite and finite wing planform [2]	75
6.7	Lift force (L_i) of a rectangular wing; RectProbSet1	80
6.8	Current Max L_i and W_{Norm} of a rectangular wing; RectProbSet1	80
6.9	Current Drag force D_i of a rectangular wing; RectProbSet1	81
6.10	Optimal: Max(L_i) & Min(R_i) WRT Aero Discipline of a rectangular wing; RectProbSet1	83
6.11	Optimal: Max(L_i) & Min(R_i) w/ 10° median WRT Aero Discipline of a rectangular wing; RectProbSet1	83
6.12	Current R_i @ Max(L_i) WRT Aero Discipline of a rectangular wing; RectProbSet1	84
6.13	Current Min(R_i) @ Max(L_i) WRT EM Discipline of a rectangular wing; RectProbSet1	84
6.14	Optimal: Min(R_i) & Max(L_i) WRT EM Discipline of a rectangular wing; PProbSet1	85
6.15	Optimal: Min(R_i) w/ 10° median & Max(L_i) WRT EM Discipline of a rectangular wing; RectProbSet1	85
6.16	Lift force (L_i) of a rectangular wing; RectProbSet2	90
6.17	Current Max L_i and W_{Norm} of a rectangular wing; RectProbSet2	90
6.18	Current Drag force D_i of a rectangular wing; RectProbSet2	91
6.19	Current R_i @ Max(L_i) WRT Aero Discipline of a rectangular wing; RectProbSet2	91
6.20	Optimal: Max(L_i) & Min(R_i) WRT Aero Discipline of a rectangular wing; RectProbSet2	92
6.21	Optimal: Max(L_i) & Min(R_i) w/ 10° median WRT Aero Discipline of a rectangular wing; RectProbSet2	92
6.22	Current Min(R_i) @ Max(L_i) WRT EM Discipline of a rectangular wing; RectProbSet2	93

6.23 Optimal: $\text{Min}(R_i)$ & $\text{Max}(L_i)$ WRT EM Discipline of a rectangular wing; PProbSet2	93
6.24 Optimal: $\text{Min}(R_i)$ w/ 10° median & $\text{Max}(L_i)$ WRT EM Discipline of a rectangular wing; RectProbSet2	94
6.25 Current Max L_i and W_{Norm} of a rectangular wing; RectProbSet3	98
6.26 Current Drag force D_i of a rectangular wing; RectProbSet3	99
6.27 Lift Coeff. C_ℓ vs. Drag Coeff. C_d of a rectangular wing; RectProbSet3	99
6.28 Lift force (L_i) of a rectangular wing; RectProbSet3	100
6.29 Current R_i @ $\text{Max}(L_i)$ WRT Aero Discipline of a rectangular wing; RectProbSet3	100
6.30 Optimal: $\text{Max}(L_i)$ & $\text{Min}(R_i)$ WRT Aero Discipline of a rectangular wing; RectProbSet3	101
6.31 Optimal: $\text{Max}(L_i)$ & $\text{Min}(R_i)$ w/ 10° median WRT Aero Discipline of a rectangular wing; RectProbSet3	101
6.32 Current $\text{Min}(R_i)$ @ $\text{Max}(L_i)$ WRT EM Discipline of a rectangular wing; RectProbSet3	102
6.33 Optimal: $\text{Min}(R_i)$ & $\text{Max}(L_i)$ WRT EM Discipline of a rectangular wing; PProbSet3	102
6.34 Optimal: $\text{Min}(R_i)$ w/ 10° median & $\text{Max}(L_i)$ WRT EM Discipline of a rectangular wing; RectProbSet3	103
6.35 Low aspect ratio of a finite thin tapered wing	107
6.36 High aspect ratio of a finite thin tapered wing	107
6.37 Lift force (L_i) of a tapered wing; TapProbSet1	109
6.38 Current Max L_i and W_{Norm} of a tapered wing; TapProbSet1	109
6.39 Current Drag force D_i of a tapered wing; TapProbSet1	110
6.40 Current R_i @ $\text{Max}(L_i)$ WRT Aero Discipline of a tapered wing; TapProbSet1	110
6.41 Optimal: $\text{Max}(L_i)$ & $\text{Min}(R_i)$ WRT Aero Discipline of a tapered wing; TapProbSet1	111
6.42 Optimal: $\text{Min}(R_i)$ & $\text{Max}(L_i)$ WRT EM Discipline of a tapered wing; TapPProbSet1	111
6.43 Current $\text{Min}(R_i)$ @ $\text{Max}(L_i)$ WRT EM Discipline of a tapered wing; TapProbSet1	112
6.44 Optimal: $\text{Max}(L_i)$ & $\text{Min}(R_i)$ w/ 10° median WRT Aero Discipline of a tapered wing; TapProbSet1	112
6.45 Optimal: $\text{Min}(R_i)$ w/ 10° median & $\text{Max}(L_i)$ WRT EM Discipline of a tapered wing; TapProbSet1	114
6.46 Lift force (L_i) of a tapered wing; TapProbSet2	115
6.47 Current Max L_i and W_{Norm} of a tapered wing; TapProbSet2	117
6.48 Current Drag force D_i of a tapered wing; TapProbSet2	117
6.49 Lift Coeff. C_ℓ vs. Drag Coeff. C_d of a tapered wing; TapProbSet2	118

6.50	Optimal: $\text{Max}(L_i)$ & $\text{Min}(R_i)$ WRT Aero Discipline of a tapered wing; TapProbSet2	119
6.51	Optimal: $\text{Max}(L_i)$ & $\text{Min}(R_i)$ w/ 10° median WRT Aero Discipline of a tapered wing; TapProbSet2	119
6.52	Optimal: $\text{Min}(R_i)$ & $\text{Max}(L_i)$ WRT EM Discipline of a tapered wing; TapPProbSet2	120
6.53	Optimal: $\text{Min}(R_i)$ w/ 10° median & $\text{Max}(L_i)$ WRT EM Discipline of a tapered wing; TapProbSet2	120
6.54	Lift force (L_i) of a tapered wing; TapProbSet3	124
6.55	Current Max L_i and W_{Norm} of a tapered wing; TapProbSet3	124
6.56	Current Drag force D_i of a tapered wing; TapProbSet3	125
6.57	Lift Coeff. C_ℓ vs. Drag Coeff. C_d of a tapered wing; TapProbSet3	125
6.58	Current R_i @ $\text{Max}(L_i)$ WRT Aero Discipline of a tapered wing; TapProbSet3	126
6.59	Optimal: $\text{Max}(L_i)$ & $\text{Min}(R_i)$ WRT Aero Discipline of a tapered wing; TapProbSet3	127
6.60	Optimal: $\text{Max}(L_i)$ & $\text{Min}(R_i)$ w/ 10° median WRT Aero Discipline of a tapered wing; TapProbSet3	127
6.61	Current $\text{Min}(R_i)$ @ $\text{Max}(L_i)$ WRT EM Discipline of a tapered wing; TapProbSet3	128
6.62	Optimal: $\text{Min}(R_i)$ & $\text{Max}(L_i)$ WRT EM Discipline of a tapered wing; TapPProbSet3	128
6.63	Optimal: $\text{Min}(R_i)$ w/ 10° median & $\text{Max}(L_i)$ WRT EM Discipline of a tapered wing; TapProbSet3	129
7.1	System design optimization flow	133

CHAPTER 1

INTRODUCTION

The design of aircraft, weapon or spacecraft structures requires a collaboration of many team members from varied disciplines to satisfy the design criteria and objectives. A typical design cycle includes many stages of refinement or modification as more knowledge is gained from laboratory testing or as new requirements are imposed. Many of these efforts consist of employing “trial and error” processes where the design is being re-analyzed many times because two or more disciplines have conflicting variables, which require compromises. Over the last two decades, the Air Force has underwritten many significant projects for the development of stealth technology in future fighter aircraft. With success comes the demand for reducing the cost in research and development time from concept to finished product.

The need remains for a method to compute or predict the electromagnetic backscattered field of an airframe and integrate the electromagnetic (EM) discipline into the Multidisciplinary Design Optimization (MDO) system design tool (a project undertaken by Dr. Vipperla Venkayya at the Air Force Research Laboratory, Wright-Patterson Air Force Base). MDO is a complex system design tool used in the implementation of multiple disciplines simultaneously with design libraries, data, and allows input variables and structure constraints to interchange

within the simulation. This paper will address the coupling of the electromagnetics discipline in an MDO scheme that includes the mathematical optimization of aerodynamics, otherwise known as the Aero discipline.

The technique to couple the computational electromagnetic backscattered field into MDO will provide an expanded opportunity to explore future aircraft configuration and performance variables, and to revolutionize the aerospace industry. Furthermore, the development of MDO methodology is not limited to aircraft design. Korte et al. [5] utilized MDO methodology to solve a preliminary design problem for a High-Speed Civil Transport (HSCT) project. Walsh et al. [6] described the combined performance, dynamics, and structural analyses using multi-level decomposition optimization techniques in the design of helicopter rotor blades. A survey by J. Sobieszczanski-Sobieski and R. T. Haftka [7] discovered that the bulk of references focus on the simultaneous optimization of structures and aerodynamics, or the simultaneous optimization of structures combined with active control. Another challenging issue will be the computational time required as additional design disciplines are integrated into the MDO system design tool.

The major emphasis of this paper will be to study the coupling effects of aerodynamic performance (maximum value) with backscattered field return (minimal value) of a specified structural shape. Thus, an understanding or background in aerodynamic performance is necessary during the course of this research.

1.1 EARLY RESEARCH ON MULTIDISCIPLINARY DESIGN OPTIMIZATION

Research projects and technical papers in the area of multidisciplinary optimization methods for aircraft design have been previously introduced to the aerospace industry. Air Force program project developed an automated design and analysis tool that performs the trade-off and synthesis tasks in a systematic way. The Automated STRuctural Optimization System (ASTROS) Enhancements [8], a software program for multidisciplinary design and analysis of aircraft structures, was the result of this effort. ASTROS is a finite element-based software tool combining mathematical optimization algorithms with traditional analysis disciplines (such as static forces, normal modes, static aeroelasticity and dynamic aeroelasticity) to perform automated preliminary design of aircraft structures. ASTROS supports the multidisciplinary nature of design by implementing the disciplines into separate modules and by using Matrix Analysis Problem Oriented Language (MAPOL), a high level language, to direct the interactions among the modules. ASTROS can treat multiple boundary conditions and multiple subcases within each boundary condition. Data transfer is accomplished using the Computer Automated Design DataBase (CADDB), a database used to recognize and handle the voluminous data and types. From the analytical aspect of ASTROS, the practical limitations on problem size are determined by available Random Access Memory (RAM), hard disk space, and data processing time.

Another technique, discussed in research paper by Kroo et al. [9] involved a new approach to system decomposition, inter-discipline communication, and methods of exploiting coarse-grained parallelism for analysis and optimization. The architecture

involved a tight coupling between optimization and analysis. Kroo described an improved method to enhance efficiency while simplifying the structure of multidisciplinary, computation-intensive design problems involving hundreds of design variables.

Later, the Framework for Interdisciplinary Design Optimization (FIDO) project was developed by Weston et al. [10] to execute multidisciplinary computations on a networked cluster of heterogeneous workstations and parallel computers. The concept being used for FIDO was course-grained parallelism (with instances of disciplinary codes, such as aerodynamics, structures, etc.) used to solve aircraft design problems. The software was written in modular form, and each disciplinary code runs on a high-speed separate processor under the control of an executive of another processor and exchanging data through a centralized data manager on yet a third processor.

1.2 INTEGRATION OF MULTIDISCIPLINARY DESIGN OPTIMIZATION

Integrating the electromagnetic solution into the preliminary design process of MDO methodology [11] has been an objective for future aircraft design by the United States, Air Force Research Laboratory at Wright-Patterson AFB. The need to evaluate electromagnetic disciplines or the backscattered field return is one of the major design considerations of future aircraft and weapon systems. Control of scattering and penetration of electromagnetic fields is the major objective of emerging low observable technologies. Various MDO methodologies were developed and employed in the design of airframe structures, such as aerospike rocket engine [5], large-scale structures optimization [12], launch vehicles [13], and

spacecraft and expert systems design [14]. On the other hand, there are numerous computer programs and techniques to compute or predict backscattered field return. Techniques such as Asymptotic Waveform Evaluation (AWE) [15,16], Finite Element Method/Method of Moment (FEM/MoM) [17], Model Based Parameter Estimation [18], Finite Difference Time Domain (FDTD) [19], Finite Element Method (FEM) [20], and Finite Element Models (FEMS) of current and future USAF aircraft [21] are available. However, none of the MDO methodologies or the techniques used in predicting the return of backscattered field address the mutual coupling effects between electromagnetic and aerodynamic performance in preliminary aircraft design.

A survey of recent MDO developments in aerospace design [22] did not address the coupling and integrating of the calculated backscattered field return of the aircraft structure as an add-on design criteria to the MDO system design tool. A review in structural optimization [23] described the wing loading design method using optimality criterion and numerical search. The needs to integrate the electromagnetic discipline with ASTROS, an USAF project initiated by Dr. V. B. Venkayya at Air Force Research Laboratory in 1987, as an integral part of the MDO system design tool for future aircraft preliminary configuration designs.

The backscattered field return of a given physical shape is computed by Xpatch software tools developed by S. W. Lee (Univ. of Illinois). The Xpatch toolset is used by the Air Force Research Laboratory and Defense Advanced Research Projects Agency (DARPA) to produce and analyze scattering data for realistic aircraft, missiles, ships, spacecraft, and ground vehicles. Xpatch is a high-frequency radar signature prediction tool based on the Shooting and Bouncing Ray (SBR)

technique. In the SBR technique, rays are traced according to geometrical optics theory as they bounce around within the target. This tracing includes the effects of polarization, ray divergence factors, and layered material transmission or reflection properties. At the point where a ray exits the target a physical optics integration is done to calculate the scattered far-field that is radiated from the target. Thus, in using the SBR technique, all single and multiple bounce contributions are accounted for by geometrical or physical optics theory.

Inputs required by Xpatch to predict the backscattered field return are very inclusive. The input files contain data parameters such as structural geometry, antenna position, frequency range, target range profile, first bounce and high bounces rays, scattered energy from edge diffraction, divergence factor for curve fitting approximation, composite materials, and coating properties. Other advanced features include spherical coordinates, moving gimbal antenna, polarization rotation, adaptive ray tracing for large facet target, scattering contribution from gaps and cracks, fixed angle bi-static scatterer, partial backscattered field return of facet target, and rough ground plane with first bounce effects.

CHAPTER 2

MULTIDISCIPLINARY DESIGN OPTIMIZATION OVERVIEW

The utilization of Multidisciplinary Design Optimization (MDO) in aircraft designs is by no means a new endeavor. The concept of MDO has been developed and advanced for over three decades. However, more work is needed in order to meet the required add-on of newly defined disciplines into MDO and to take advantage of the available high-speed, high-performance computing machines. A number of software packages have been written and procedures developed to maximize impact on the preliminary aircraft structural design stage in which the configuration has been defined and the composite material has been selected. The goal of MDO was to determine the performance of an aircraft with a varying structure, size, and shape that will satisfy the constraint parameters imposed by other disciplines. MDO has been employed as a system design tool that integrates existing disciplines and methodologies into a unified multidisciplinary package. Some of the key benefits of MDO are the shortened design cycle time, improved aerodynamic performance, and better structural designs as composite materials come into widespread use. For example, MDO is used in balancing conflicting requirements for the strength and stiffness of the structure while exploiting the benefits of anisotropy. Some tasks, such as the analytical sensitivity of aeroelasticity are perhaps impossible tasks without MDO.

Recent development of MDO introduces a lot of optimization methodologies into air vehicle conceptual and preliminary design [24]. The Multi-Objective approach responds to the increasing demands in high-performance supersonic transport [25] where drag reduction in conflict with sonic boom minimization and the trade-offs among aerodynamic performance, structural strength and weight are considered. Obayashi et al. [25] described the utility of Multi-Objective Genetic Algorithms (MOGA) in wing shape design optimization by employing Pareto ranking, crossover, and fitness approaches.

MDO that treats only design variables as optimization variables, known as the Multiple Discipline Feasible (MDF) [26] approach, maintains complete multidisciplinary feasibility each and every design cycle. The drawback of MDF is that it can be a time-consuming and costly procedure. MDO approaches such as Simultaneous Analysis and Design (SAND) [27], and Individual-Discipline-Feasible (IDF) [28] are intermediate approaches in which each individual subsystem is independently feasible at every optimization iteration. All-at-Once (AAO) [29] treats the entire multidisciplinary design cycle as one large optimization problem that eliminates the costly iteration cycle and is a complicated MDO problem.

A number of previous research efforts involving MDF, IDF, and AAO solutions have been limited to a classical two subsystem multidisciplinary optimization. Distribute Coevolutionary Multidisciplinary Design Optimization (DCMDO) [30] is a flexible MDO framework that accepts whatever design variables and multiple objective functions using a coevolutionary algorithm. In DCMDO, multidisciplinary coupled system design optimization is divided into parallel subsystem optimizations

implemented on multiple computers. It required additional analysis compared to traditional mathematical programming based MDO.

2.1 STOCHASTIC MUTATION ALGORITHM MULTIDISCIPLINARY OPTIMIZATION CONCEPT

The key concept in MDO methods is decomposition of design task into subtasks which are performed independently and computation intensive. The solution in piecewise based optimization method, known as Optimization by a Mix of Dissimilar Analysis and Approximations (OMDAA) [31] uses up to 254 concurrently operating processors. If the analysis is executed on a single processor and repeated the number of times this optimization required, it would have taken 257 days of elapsed computing time. Employing parallel processing has reduced the elapsed time to one day. Current effort to couple electromagnetic backscattered field among the aerodynamic performance function [32] for high frequency application is undertaken at the Air Force Research Laboratory.

Approaches to the design optimization of complex, coupled disciplines give rise to the need of creating an unique MDO process. The Stochastic Mutation Algorithm (SMA) shown in Figure 2.1 leverages the concurrent multiprocessing approach in which each iteration or trial is evaluated according to "Q" cycles, where "Q" is the number of disciplines in multidisciplinary optimization. SMA utilizes a mutating scheme to retain an optimum solution under the best-case scenario performance function simultaneously. In SMA, the constraint variables are randomized to exploit the "what if" scenarios and require no prior knowledge of the performance functions.

In addition to Genetic Algorithms (GA), Evolution Algorithms (EA), other algorithms, such as the Torus Algorithm [33], Simplex Algorithm [34], Adaptive

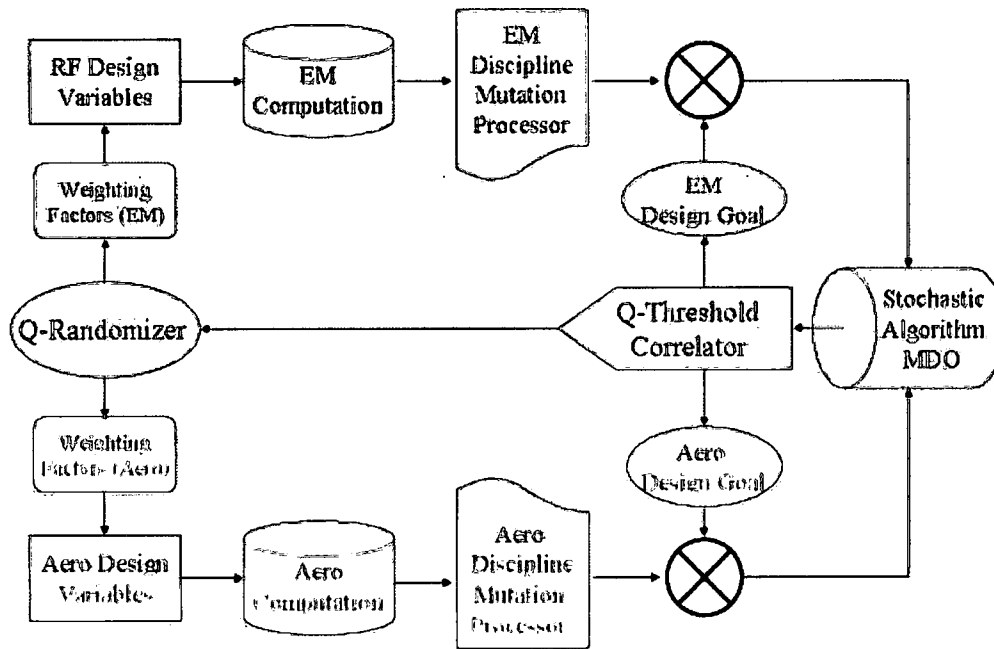


Figure 2.1: Stochastic Mutation Algorithm MDO Block Diagram

Random Search Algorithm [35], and Simulated Annealing Algorithm [36] have been developed to solve optimization problems. A study using Stochastic Algorithms for generating an optimal jamming waveform for electronic countermeasures [37] showed promise. Optimization problems are complex in nature and application specific in terms of search criteria, multimodal functions, mathematical functions, numerical analysis, design robustness, and most importantly, computational feasibility.

The advantage of using SMA in optimization problems is that there is no order or rank required on the variable constraints, and no parent-child association is needed to render an optimum solution with respect to MDO. The SMA optimization process pursues a concurrent approach to achieve fast convergence using mutation method among the Aero and EM disciplines and attains an optimum solution with

respect to the Aero & EM disciplines. The primary objective of this paper is to solve multi-performance functions to attain a maximum lift (with nominal induced drag due to lift) and a minimum backscattered field return with respect to the EM discipline under a given arbitrary wing planform. The coupling effect among the Aero and EM disciplines can be classified as an adaptive mutation process and requires an initial set of design variables to kick start the iteration procedures until an optimum solution is reached. The process re-iterates and derives a best-case scenario within the design criteria to obtain an optimal solution set. A built-in weighting function, which can be used to mitigate sensitive design variables, allows designers to assess the effecting components among design variables and constraints.

Like many algorithms, the intermediate stage of SMA process is not well understood since the relationship among the design variables and constraints is arbitrary. In particular, solving Maxwell's equations for boundary conditions, geometry description, physical shape and orientation is a challenging task. Numerical analysis and approximation that determines the accuracy of predicting backscattered field return with respect to the Aero discipline is complex and computationally expensive. The coupling of concurrent synchronized data among the Aero and EM disciplines in the context of MDO is often time consuming.

The uniqueness of SMA in reference to MDO perspective is that by employing dynamic threshold limits it avoids spiral effect, the probability of being trapped by local minima or maxima. Since SMA optimization seeks to maximize Aero lift or minimize EM backscattered return monotonically, the computation converges at each and every iteration or trial. Furthermore, since the constraints and design variables are random in nature (not in any particular ranking order), the method

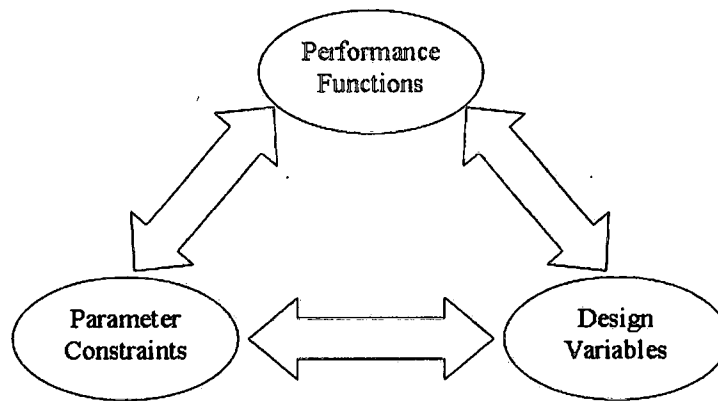


Figure 2.2: Multidisciplinary design optimization elements interaction

allows a robust design optimization with a large degree of freedom while improving convergence. The formulation of SMA in MDO lies in the interdisciplinary interaction in which both Aero and EM disciplines satisfy the performance functions individually and “complete multidisciplinary” optimization is maintained.

2.2 BASIC CONCEPTS IN MULTIDISCIPLINARY DESIGN OPTIMIZATION FOR PRELIMINARY DESIGN

The implementation of the electromagnetic discipline into MDO can be viewed as an interaction of three MDO library elements as shown in Figure 2.2, where the performance functions and environmental parameter constraints are interchangeable. The environmental parameter constraints impose a range of values ($\text{Min}(x) - \text{Max}(x)$) onto design variables.

The objective of a performance function is to optimize each discipline under the controlled environmental parameters. For an air vehicle design, the optimal

performance function would be to maximize the aerodynamic performance and minimize its backscattered field return. Typical aero design variables include mass, surface area, thickness, stiffness, physical size, geometrical configuration, etc; where design constraints may be described in term of strength, stress, strain, stiffness, displacement, frequency, flutter, lift force, roll, payload, etc. By expanding and contracting the basis of the three MDO elements shown in Figure 2.2, the design problem can be tailored according to needs. The knowledge gained on the requirements as new conditions are imposed allows further refinement to improve future aircraft design. There is no explicit procedure to decide which combination of constraints and variables will yield an optimal solution. The design effort is iterated $2m+n$ times, where "m" is the number of constraints and "n" is the number of variables. The process is labor intensive and time consuming because two or more disciplines may have incoherent demands that require compromise and resetting the optimization threshold of the interacting disciplines. Thus, assigning a weighting factor associated with each discipline is essential to rank its priority among them. It is of great value to realize that analysis methods developed in the past can be used for evaluating the performance and constraint functions while the critical variables of interest are generally part of the optimal equations. Furthermore, each interacting discipline does not limit itself to the number of constraints of variables, which refers to the problem size as it directly relates to computation power, dynamic memory capacity, and data storage space. However, each discipline must conform to the design criteria as shown in Figure 2.2. The problem size is not of major concern since computing technology has advanced rapidly.

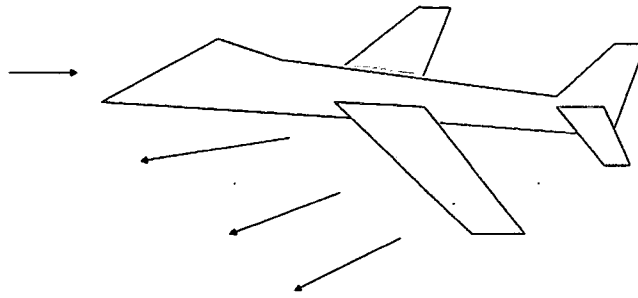


Figure 2.3: Backscattered field return contributors

A Stochastic Mutation Algorithm (SMA) of a MDO block diagram that coupled the radio frequency (RF) or electromagnetic (EM) backscattered field solution with air vehicle design (Aero discipline) is shown in Figure 2.1. The SMA model consists of a Q-element parallel computation process under a given set of constraints and variables, where “Q” is the number of disciplines. The goal of SMA is to develop a method in which each discipline can be defined and analyzed in parallel while attaining the best yield to meet the overall design requirements.

The Aero discipline shown in Figure 2.3 was simplified to demonstrate the inter-coupling and inter-effect between electromagnetic and aerodynamic. The Aero discipline in itself is a complex structural and architectural design issue containing many disciplines within. In fact, the backscattered field return solution is generally sought after the aero parameters have been fully defined and the performance function has been developed and simulated. The cause and effect process known as the “hit or miss” approach is ineffective. The objective of this paper is to develop a cross-over method to minimize the backscattered field return while maintaining the optimal aero performance simultaneously. The goal of the EM solution is to

minimize the return of backscattering field under the defined constraints and design variables of the object under consideration. It is not a case of RCS reduction, where applying radio frequency (RF) absorbing material on the object introduces an additional foreign variable (additional weight) to the original design variables.

To illustrate the EM solution within the context of aerodynamic optimization environment, an air vehicle shown in Figure 2.3 is used to describe the backscattered field contribution, the computational methods, and the application of Stochastic Mutation Algorithm in MDO process. Various numerical approaches in computing or predicting the return of backscattered field are complimentary. A description of the numerical methods and its application will be addressed in brief, since the intention of the author is to develop an approach utilizing those well-defined methods for the application specified.

CHAPTER 3

ELECTROMAGNETIC SCATTERING FIELDS COMPUTATIONAL APPROACHES AND APPROXIMATION METHODS

3.1 INTRODUCTION

Many analytical tools and computational approaches available for predicting the backscattered field contribution are well defined for certain specific application and physical size. Computer Aided Design (CAD) tools or computer codes provide predictions of experimentally measured backscatter vs. angle. These computer codes offer an insight into the scattering effect and helps to give a better understanding of the interaction of the electromagnetic with the aero structure and ultimately enhances the MDO process. Two analytical methods (Numerical and Asymptotic) which are widely used to approximate electromagnetic backscatter fields are listed below.

3.1.1 NUMERICAL METHODS

Numerical and analytical techniques are powerful tools to aid in the understanding of electromagnetic field scattering. The notions of specular, end region, edge diffraction, surface waves, shadowing, and multiple ray bouncing do not emerge from numerical solutions. In order to fully understand the underlying processes, both numerical and analytical solutions are needed to describe surface

currents, near electric fields, and most importantly, form images from these solutions. The numerical solutions to Maxwell's equations in integral or differential form are listed below:

- i. Method of Moments (MoM)
- ii. Finite Difference Time Domain (FDTD)
- iii. Finite Elements (FE)

3.1.2 METHOD OF MOMENTS

Method of Moments (MoM) is a numerical technique used to solve Electromagnetic radiation problems expressed in the forms of integral equations [38–40] which describe the field incident on a surface to the current induced on the surface of the scatterer. MoM is suitable for solving the unknown induced current density and is generally thought of as low-frequency technique due to its application to arbitrarily small objects in term of wavelength.

Computer solutions for solving Maxwell's integral equations were made possible by Harrington's classic book [41] on MoM in the late 1960. MoM provides accurate backscatter predictions by solving the direct integral Maxwell's equations in the frequency domain. It is well suited for modeling surface currents of arbitrarily small structures in fine detail. Because MoM represents the numerical solution for an exact formulation, it is required whenever the high-frequency specular, end-region, and diffraction approximation are no longer adequate.

3.1.3 FINITE DIFFERENCE TIME DOMAIN

Another numerical approach to compute the "exact" solution to Maxwell's differential form is the Finite Difference Time Domain (FDTD) method. The early

FDTD only allowed incident radiation in one direction [42] with limited step time. The development of absorbing outer boundary conditions [43, 44] levitated the step time limit where fields scattered from one body could propagate away from the target without bouncing back into the interaction region. Recent results by Yee [45] illustrated how to have a curved boundary condition that transitions to a rectangular grid, and an arbitrary 3-dimensional scatter FDTD [46] offset computational grid for E and H fields used to satisfied Ampere's and Faraday's laws. Note that the basic FDTD code uses Maxwell's curl equations in derivative form in the time domain. Thus the small grid spacing used in the integral in FDTD results in large data size and is computationally intensive.

3.1.4 FINITE ELEMENTS

Finite Elements (FE), like Finite Difference, are also based on the differential form of Maxwell's equations in the frequency domain. Its application to the classical waveguide mode problem was published in a special issue of the Italian journal *Alta Frequenza* [47], and rapid development on magnetic fields FE was soon applied to integral operators in antenna problems, electromagnetic scattering, and backscattered field return calculations [48]. Adaptive FE boundary integral analysis is suitable for the time-harmonic, electromagnetic analysis of three-dimensional inhomogeneous scatterers [49] of both electric and magnetic field solutions for low frequency applications. Whereas the numerical method in FM applications on scattering and radiation problems for high frequency and boundary conditions are difficult problems to be analyzed. The accuracy of FE solutions can at times be challenged and requires special shape functions with singular behavior near edges or

corners to approximate the electromagnetic fields [50]. This problem was cited in FE applications to electromagnetic problems [51]. Additional studies to evaluate numerical errors in FE methods [52] in terms of higher order shape functions are not applicable for the radiation condition. Hence, FE application to electromagnetic scattering problems is viewed as a numerical technique for evaluating Green's function of a bounded, complex structure with known boundary conditions and required the Sommerfeld radiation condition into the problem formulation.

3.2 ASYMPTOTIC METHODS

Asymptotic methods are high-frequency approximation methods, suitable for treating electromagnetic scattering from targets of large extent where poor convergence properties of eigenfunction solutions or solutions based on Rayleigh's method occur. A brief description of some asymptotic methods used in predicting the backscattered field return for high frequency scattering problems is shown below:

- i. Physical Optics / Physical Theory of Diffraction
- ii. Geometrical Optics / Geometrical Theory of Diffraction
- iii. Uniform Theory of Diffraction

3.2.1 PHYSICAL OPTICS AND PHYSICAL THEORY OF DIFFRACTION APPROACH

Physical Optics (PO) high-frequency approximation, is based on the application of image theory to large structures. This affords assumption that the tangential magnetic fields at the target surface are equal to twice the incident magnetic field in the directly illuminated region and that they are zero elsewhere (no surface current in the shadow region). For high frequency application (small λ), physical optics

becomes unsuitable for predicting the scattering field where the neglected surface currents will be the main producer of the field. Thus Physical Optics cannot account for higher order mechanisms including edge diffraction, tip diffraction, and surface waves. Physical Theory of Diffraction (PTD) for treating edges [53] is the corrective form of Physical Optics, with the inclusion of fringe currents (the difference between the true currents and the physical optics currents). In other words, PTD is an extension of PO that includes specular diffraction as well as non-specular diffraction (edge diffraction) effects.

3.2.2 GEOMETRICAL OPTICS AND GEOMETRICAL THEORY OF DIFFRACTION APPROACH

Geometrical Optics (GO) were originally developed to analyze the propagation of light where the frequency is sufficiently high that the wave nature of the light need not be considered. GO uses the ray path method, an easily understood concept, to compute the amplitude of reflected fields from one point to another without any reference to whether the transport mechanism is a particle or a wave in nature, and is accurate for high frequency analysis. However, GO ignores the polarization and wave nature of the electromagnetic field and is not capable of calculating a non-zero field in the shadow region where diffracted fields exist.

Geometric Theory of Diffraction (GTD), developed by Keller [54,55] in the 1950s as an extension to GO which is well known and is an easily applied approximate method for estimating the scattered field energy based on the ray theory of field propagation. Unlike GO, which only considered the direct, reflected, and refracted rays, GTD includes the diffracted rays that exist in the shadow region. The inclusion of diffracted rays will remove the field discontinuities at the boundaries for

the geometrical optics rays, and introduce proper field corrections in the regions between these boundaries, especially in the zero-field regions predicted by Geometrical Optics.

3.2.3 UNIFORM THEORY OF DIFFRACTION APPROACH

Uniform Theory of Diffraction (UTD) developed by Kouyoumjian and Pathak [56] strives to accurately represent the diffracted field by overcoming the diffraction coefficient singularities. However, UTD does not eliminate the difficulties of the caustics of geometrical theory of diffraction where an infinity of rays converge. As such, UTD fails when the incident field is not a ray optical field and cannot be applied when reflection and diffraction no longer are local phenomena. UTD is a high frequency method for solving electromagnetic scattering problems from electrically small discontinuities or discontinuities in more than one dimension at the same point. UTD approximates near field electromagnetic fields as Quasi-Optical and uses Ray diffraction to determine diffraction coefficients for each diffracting object - source combination. These coefficients are then used to calculate the field strength and phase for each direction away from the diffracting point. These fields are added to the incident fields and reflected fields to obtain a total solution.

CHAPTER 4

BACKSCATTER COMPUTATION METHOD

Asymptotic methods are suitable techniques for predicting scattered fields of a large arbitrary object. Physical Optics (PO) is applicable for radiated field currents in the illuminated region, where the direct or specular reflection fields are dominant (with the assumption that no current in the shadow regions are zero). Whereas Physical Theory of Diffraction (PTD), an extension of PO was developed to include the specular diffraction as well as edge diffraction (non-specular) effects [57]. However, PTD does not account for the non-specular effects by travelling waves and creeping waves, and has no explicit expression for the non-uniform component current. Thus, its application is limited to those edged shape bodies [58] such as the one shown in Figure 4.1. The surface current is evaluated directly by the integral over the surface of the scatterer, where \mathbf{n} is a unit normal vector outward from the surface of interest.

Geometrical Optics (GO), a ray optics method, was developed to analyze the propagation of a small wavelength with respect to the scatterer size under consideration. GO characterizes how fields behave in the presence of geometrical discontinuities, and quantifies the field contribution from a source through direct, reflected, or refracted rays. In examining the manner in which fields are diffracted by edges of a general case, let's assume a line source is placed near the conducting

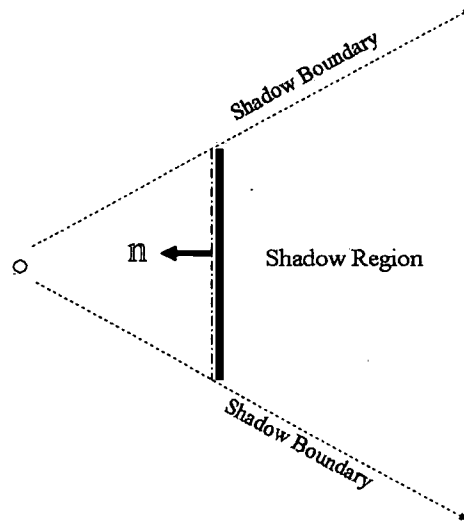


Figure 4.1: Surface current of an edge shape body

wedge of interior angle $(2 - n)\pi$ as shown in Figure 4.2 where $0 < n \leq 2$. The observation point P is made with a constant radius from the edge of the wedge. By geometrical optics radiation mechanisms, the fields surrounding the wedge are separated into three regions (I, II, III) as shown.

In region I, besides the direct ray from source to observation point P , there are reflected rays from the side of the wedge and the trajectory rays that pass through the edge of the wedge leading to the generalized Fermat [59] principle, designated as diffracted rays. Hence region I consists of direct, reflected, and diffracted fields. In a similar perspective, region II contains direct, and diffracted fields, and Region III only consists of diffracted field. Due to the field discontinuities that form along the reflected shadow and incident shadow boundaries where diffracted fields are included to fill the gaps in all three regions, the field in any one of the three regions consists of a reflected field and a incident field which is shown as

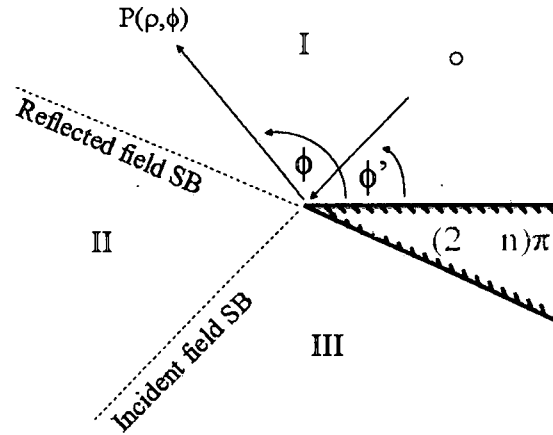


Figure 4.2: Field Regions of a Conducting Wedge

$$E(\rho, \phi) = V^i(\rho, \phi^-) \pm V^r(\rho, \phi^+) \quad (4.1)$$

where $\phi^\pm = \phi \pm \phi'$, and in the second term on the right side of equation, the plus sign (+) represents the incident field in perpendicular to the diffracting edge, and the minus sign (-) in parallel to the diffracted edge. In Equation (4.1), the first term on the right side, is the incident field which consists of geometrical optics incident field and a diffracted field, while the second term represents the reflected field, also consisting of two parts: the geometrical optics reflected field and a diffracted field.

$$V^i(\rho, \phi^-) = V_g^i(\rho, \phi^-) + V_d^i(\rho, \phi^-, n) \quad (4.2)$$

$$\pm V^r(\rho, \phi^+) = \pm [V_g^r(\rho, \phi^+) + V_d^r(\rho, \phi^+, n)] \quad (4.3)$$

Equations (4.2) and (4.3) each satisfy the wave equation individually except at the reflection and incident shadow boundary regions. The total geometrical optics

fields on a constant phase wave front consist of incident and reflected fields and are given by

$$V_g^i(\rho, \phi^-) = e^{j\beta\rho \cos(\phi^-)} \quad (4.4)$$

$$V_g^r(\rho, \phi^+) = e^{j\beta\rho \cos(\phi^+)} \quad (4.5)$$

The total diffracted field expressed by an asymptotic evaluation of a contour integral (consists of diffracted fields of incident and reflected regions) is given by

$$V_d(\rho, \phi^\mp, n) = V_d^i(\rho, \phi^-, n) + V_d^r(\rho, \phi^+, n) \quad (4.6)$$

where

$$V_d^{i,r}(\rho, \phi^\mp, n) = I_{-\pi}(\rho, \phi^\mp, n) + I_{+\pi}(\rho, \phi^\mp, n) \quad (4.7)$$

$$I_{\pm\pi}(\rho, \phi^\mp, n) = e^{-j(\beta\rho + \frac{\pi}{4})} \sqrt{a^\pm} \cot\left(\frac{\pi \pm \phi^\mp}{2n}\right) e^{j\beta\rho a^\pm} \int_{\sqrt{\beta\rho a^\pm}}^{\infty} e^{-j\tau^2} d\tau + (\text{high - order terms}) \quad (4.8)$$

$$a^+ = 1 + \cos(\phi^\mp - 2n\pi N^+) \quad (4.9)$$

$$a^- = 1 + \cos(\phi^\mp - 2n\pi N^-) \quad (4.10)$$

$$2n\pi N^+ - \phi^\mp = +\pi \quad \text{for } a^+ \quad (4.11)$$

$$2n\pi N^- - \phi^\mp = +\pi \quad \text{for } a^- \quad (4.12)$$

where N^+ and N^- are functions of $\phi^\pm = \phi \pm \phi'$ and n . For $0 \leq \phi \leq n\pi$ and $0 \leq \phi' \leq n\pi$ with $1 \leq n \leq 2$, N^+ takes on values 0 and +1, and N^- takes on values

-1, 0, and +1 which most closely satisfies the equation. Note that a^+ and N^+ are associated with the top surface of the conducting wedge; whereas a^- and N^- are associated with the lower surface.

If observation is made away from each of the shadow boundaries so that $\beta\rho a^\pm \gg 1$, then Equations (4.7), (4.8), (4.9), (4.10), (4.11), (4.12) reduce to (4.13). The condition in which $\beta\rho a^\pm \gg 1$ can be attained by:

- a) $\beta\rho$ and a^\pm large (observation point distance is large, and observation angle ϕ is far away from the reflected or incident shadow boundaries.
- b) $\beta\rho$ large and a^\pm small (observation point distance is large, and observation angle ϕ is near either or both shadow boundaries.
- c) $\beta\rho$ small and a^\pm large (observation point distance is small, and observation angle ϕ is far away from either the reflected or incident shadow boundaries.

$$V_d(\rho, \phi^\mp, n) = \frac{e^{-j(\beta\rho + \frac{\pi}{4})} \sin(\frac{\pi}{n})}{\sqrt{2\pi\beta\rho}} \frac{1}{n} \left(\frac{1}{\cos(\frac{\pi}{n}) - \cos(\frac{\phi^-}{n})} \pm \frac{1}{\cos(\frac{\pi}{n}) - \cos(\frac{\phi^+}{n})} \right) \quad (4.13)$$

However, the asymptotic form yields infinite fields in the immediate vicinity of the transition region or shadow boundary [60]. Figure 4.3 illustrates a plane wave of incident angle ϕ' , impinging on a half-plane ($n = 2$) as how ray contributions in the three classified regions (I, II, and III). Regions I and II are divided by the reflected shadow boundary, where Regions II and III are divided by the direct or incident field shadow boundary. Region I consists of direct, diffracted, and reflected fields. Region II contains the direct and diffracted fields, and Region III contains only the diffracted field.

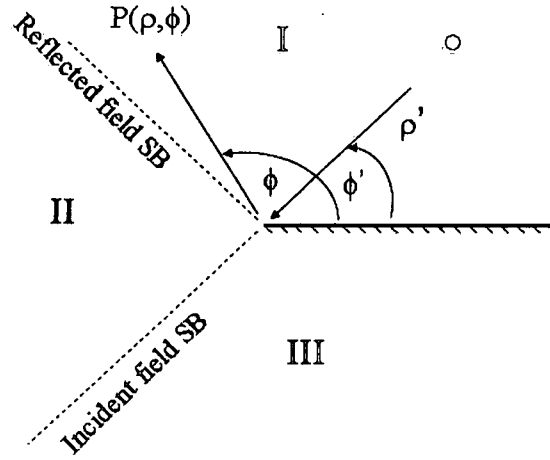


Figure 4.3: Diffracted fields in the shadow boundary (SB)

In the past several decades, mathematical expressions for the diffracted field have gained substantial attention and research interest in an effort to improve upon the classical work of Sommerfeld [61]. For the half-plane problem, Sommerfeld obtained an expression for the diffracted field observed at a distance, due to the incident plane wave in term of Fresnel integral, is given by

$$V_d(\rho, \phi^\pm) = -e^{j(\frac{\pi}{4})} \sqrt{\frac{2}{\pi a}} e^{j\beta\rho \cos(\phi^\pm)} \cos\left(\frac{\phi^\pm}{2}\right) \int_{\sqrt{\alpha\beta\rho}}^{\infty} e^{j\tau^2} d\tau \quad (4.14)$$

where $\phi^\pm = \phi \pm \phi'$, $\alpha = 1 + \cos(\phi^\pm)$, and $\beta = \frac{2\pi}{\lambda}$. Figure 4.4 shows the total electric field and diffracted fields of a half-plane ($n = 2$) which yielded two infinite fields near the reflected and incident shadow boundary. Field in any regions consists of reflected field and incident field.

Equation 4.1 is only valid outside the transition region and the observation point, P , is at a large electrical distance from the diffracted edge. In Region I, where $\phi < 105^\circ$, the total field are composed of incident and reflected fields. For $105^\circ < \phi < 255^\circ$, the total field oscillation is due the interference between the

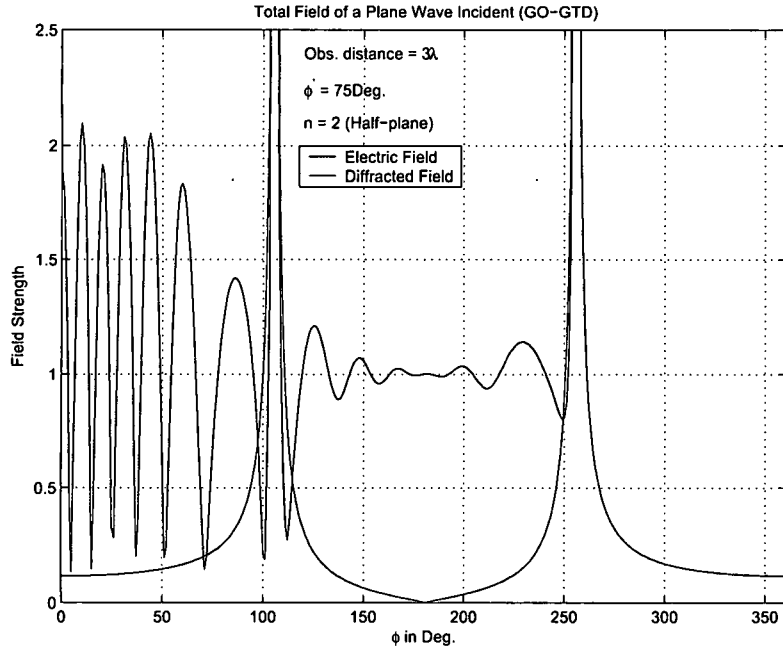


Figure 4.4: Total field of a conducting Half-Plane

incident field and the diffracted field. For $\phi > 255^\circ$, the diffracted field is the total field.

Pauli [62] included the high order terms (H.O.T.) of Sommerfield's contour integral to yield a more accurate solution near the shadow boundary regions than Equation (4.6) and (4.13). Pauli's result is given by

$$v(\rho, \phi^\pm) = \frac{2e^{j(\frac{\pi}{4})}}{n\sqrt{\pi}} \left| \cos\left(\frac{\phi^\pm}{2}\right) \right| \frac{\sin(\frac{\pi}{n})}{\cos(\frac{\pi}{n}) - \cos(\frac{\phi^\pm}{n})} e^{j\beta\rho\cos(\phi^\pm)} \int_{\sqrt{\alpha\beta\rho}}^{\infty} e^{j\tau^2} d\tau + [\text{H.O.T}] \quad (4.15)$$

The expression is valid for $0 < n \leq 2$. For the half-plane case where $n = 2$, the high order terms in Equation (4.15) are zero, which has the similar result of Equation (4.14).

4.1 UNIFORM THEORY OF DIFFRACTION

The uniqueness of the Uniform Theory of Diffraction (UTD) is that the transition function in the diffraction coefficients enforces continuity across the incident and reflected shadow boundaries and remains bounded at the immediate vicinity. The transition function approaches zero at the same rate as cotangent terms in the diffraction coefficients approach infinity at the shadow boundaries. For high-frequency analysis, GTD is a useful tool for predicting the diffracted fields in the regions away from the shadow boundaries, but becomes singular in the transition regions surrounding the boundaries. Kouyoumjian and Pathak [56] show that the diffracted fields remain bounded across the shadow boundaries by multiplying the diffraction coefficients by a transition function that approaches zero at the same rate as the diffraction coefficients become singular at the shadow boundaries. The incident and reflected diffraction function of Equation (4.6) can also be written as

$$v_d^i(\rho, \phi^-, n) = \frac{e^{-j\beta\rho}}{\sqrt{\rho}} D^i(\rho, \phi^-, n) \quad (4.16)$$

$$v_d^r(\rho, \phi^+, n) = \frac{e^{-j\beta\rho}}{\sqrt{\rho}} D^r(\rho, \phi^+, n) \quad (4.17)$$

where $D^i(\rho, \phi^-, n)$ and $D^r(\rho, \phi^+, n)$ are the incident and reflected diffraction coefficient for an incident plan wave respectively, and the total diffraction function of Equation (4.6) can now be written as

$$v_d(\rho, \phi, \phi', n) = \frac{e^{-j\beta\rho}}{\sqrt{\rho}} [D^i(\rho, \phi^-, n) \mp D^r(\rho, \phi^+, n)] \quad (4.18)$$

and

$$D^i(\rho, \phi^-, n) = \frac{e^{-j\frac{\pi}{4}}}{2n\sqrt{2\pi\beta}} \left[\cot\left(\frac{\pi + \phi^-}{2n}\right) F[\beta\rho a^+(\phi^-)] + \cot\left(\frac{\pi - \phi^-}{2n}\right) F[\beta\rho a^-(\phi^-)] \right] \quad (4.19)$$

$$D^r(\rho, \phi^+, n) = \frac{e^{-j\frac{\pi}{4}}}{2n\sqrt{2\pi\beta}} \left[\cot\left(\frac{\pi + \phi^+}{2n}\right) F[\beta\rho a^+(\phi^+)] + \cot\left(\frac{\pi - \phi^+}{2n}\right) F[\beta\rho a^-(\phi^+)] \right] \quad (4.20)$$

where $a^\pm(\phi^\pm) = a^\pm(\phi \pm \phi')$ is the angular separation between the field point and a shadow or reflection boundary, and is defined as

$$a^\pm(\phi^\pm) = 2 \cos^2 \left[\frac{2n\pi N^\pm - \phi^\pm}{2} \right] \quad (4.21)$$

with N^+ and N^- being a +1, -1, or 0 which most closely satisfies the equation

$$2n\pi N^+ - (\phi \pm \phi') = \pi \quad (4.22)$$

$$2n\pi N^- - (\phi \pm \phi') = -\pi \quad (4.23)$$

whereas $F[\beta\rho a^\pm(\phi^\pm)]$ is the Fresnel integral being used as the correction factor in the transition regions of the shadow boundaries and is given by

$$F[U] = 2j\sqrt{U}e^{jU} \int_{\sqrt{U}}^{\infty} e^{-j\tau^2} d\tau \quad (4.24)$$

where by variable substitution

$$\int_{\sqrt{U}}^{\infty} e^{-j\tau^2} d\tau = \sqrt{\frac{\pi}{2}} \left(\frac{1}{2} - \frac{j}{2} \right) - \sqrt{\frac{\pi}{2}} \int_0^U \frac{e^{-j\tau}}{\sqrt{2\pi\tau}} d\tau \quad (4.25)$$

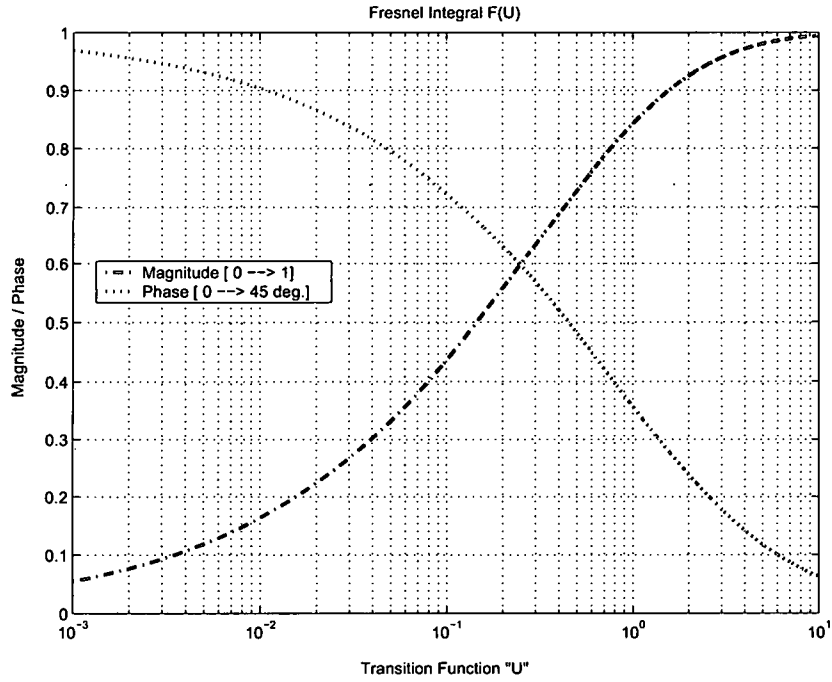


Figure 4.5: Fresnel magnitude and phase transition function

The argument of the transition function $U = \beta \rho a^\pm(\phi^\pm)$ can be determined for a given known value $\beta \rho$ if $a^\pm(\phi^\pm)$ is known. The magnitude and phase of the transition function of Equation (4.25) are shown in Figure 4.5.

Hence, the expanded form of the diffraction coefficient for soft (parallel) and hard (perpendicular) can be written as

$$D_s(\rho, \phi, \phi', n) = [D^i(\rho, \phi^-, n) - D^r(\rho, \phi^+, n)] \quad (4.26)$$

$$D_h(\rho, \phi, \phi', n) = [D^i(\rho, \phi^-, n) + D^r(\rho, \phi^+, n)] \quad (4.27)$$

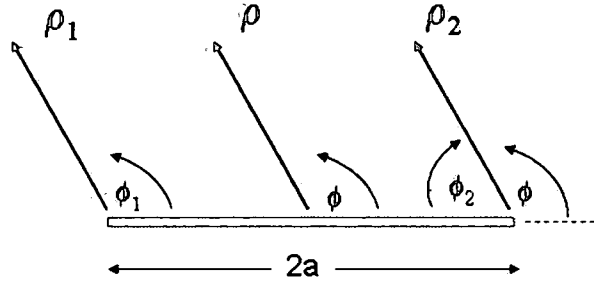


Figure 4.6: Backscattered field of an infinite strip

Thus the total diffracted field for a parallel or perpendicular of a given plane wave are defined as

$$E_s^d(\rho, \phi, \phi', n) = D_s(\rho, \phi, \phi', n) E_s^i(\rho', \phi') \frac{e^{-j\beta\rho}}{\sqrt{\rho}} \quad (4.28)$$

$$E_h^d(\rho, \phi, \phi', n) = D_h(\rho, \phi, \phi', n) E_h^i(\rho', \phi') \frac{e^{-j\beta\rho}}{\sqrt{\rho}} \quad (4.29)$$

Equations (4.28) and (4.29) are much simpler forms of expressions in terms of incident and reflected diffracted coefficients, incident field at reference point, phase factor, and spatial attenuation.

4.2 BACKSCATTERED RETURN OF PLATE

An infinitely thin perfectly conducting plate of width $2a$, as shown in Figure 4.6, illustrates the Geometrical Theory of Diffraction (GTD) where the scattered fields are defined by stationary phase arguments [1] or by abrupt geometric discontinuities. Refer to Keller's expression for scattered fields due to edge of an infinite half-plane [63].

Diffracted ray contributions are due to single diffraction when an incident plane wave is perpendicular to the left or right edge of the infinite strip. Double diffraction

occurs when the incident ray is diffracted at one edge and travels across to the other edge, and then travelling back, produces higher-order multiple diffracted rays.

However, the backscattered fields contribution derived from higher-order rays is not significant. The total backscattered fields expression for vertical and horizontal polarization in [1] did not account for the diffracted fields at both edges.

For large ρ , the backscattered field of a monostatic system ($\phi = \phi'$) reduced to the form of Keller as in Equation (4.13) where $n = 2$.

$$E_1^d = -\frac{e^{-j\frac{\pi}{4}}e^{-j\beta a \cos(\phi)}}{2\sqrt{2\pi\beta}} \left[1 - \frac{1}{\cos(\phi)} \right] \frac{e^{-j\beta\rho_1}}{\sqrt{\rho_1}} \quad (4.30)$$

$$E_2^d = -\frac{e^{-j\frac{\pi}{4}}e^{-j\beta a \cos(\phi)}}{2\sqrt{2\pi\beta}} \left[1 + \frac{1}{\cos(\phi)} \right] \frac{e^{-j\beta\rho_2}}{\sqrt{\rho_2}} \quad (4.31)$$

The phase and amplitude of backscattered field diffracted from edge 1 ($\phi_1 = \phi$) and edge 2 ($\phi_2 = \pi - \phi$) are defined as

$$\rho_1 = \rho - a \cos(\pi - \phi) = \rho + a \cos(\phi) \quad (4.32)$$

$$\rho_2 = \rho + a \cos(\pi - \phi) = \rho - a \cos(\phi) \quad (4.33)$$

where $\rho_1 \approx \rho_2 \approx \rho$, then the total diffracted field is

$$E^d = E_1^d + E_2^d = \frac{e^{-j\frac{\pi}{4}}}{\sqrt{2\pi\beta}} \left[\cos(\beta 2a \cos(\phi)) \pm j\beta 2a \frac{\sin(\beta 2a \cos(\phi))}{\beta 2a \cos(\phi)} \right] \frac{e^{-j\beta\rho}}{\sqrt{\rho}} \quad (4.34)$$

The positive (+) on the right side second term is referred as the soft (parallel) polarization, and negative (-) is the hard (vertical) polarization.

For a monostatic system ($\phi = \phi'$), the backscattered field of Physical Optic of an infinite strip (both parallel and vertical polarization) of Figure 4.6 is given as

$$E^d = 2a\sqrt{\frac{j\beta}{2\pi}}e^{j\beta 2a \cos(\phi)} \left[\sin(\phi) \frac{\sin(\beta 2a \cos(\phi))}{\beta 2a \cos(\phi)} \right] \frac{e^{-j\beta\rho}}{\sqrt{\rho}} \quad (4.35)$$

The diffraction coefficient of an infinite strip defined by Equation (4.19) and (4.20) for edge 1 and edge 2 are shown below

$$D_1^d = \frac{-e^{-j\frac{\pi}{4}}}{2n\sqrt{2\pi}\beta} \left[\left(\cot\left(\frac{\pi}{2n}\right) F(\beta\rho a^+(\phi^-)) + \cot\left(\frac{\pi}{2n}\right) F(\beta\rho a^-(\phi^-)) \right) \mp \left(\cot\left(\frac{\pi + 2\phi_1}{2n}\right) F(\beta\rho a^+(\phi^+)) + \cot\left(\frac{\pi - 2\phi_1}{2n}\right) F(\beta\rho a^-(\phi^+)) \right) \right] \quad (4.36)$$

$$D_2^d = \frac{-e^{-j\frac{\pi}{4}}}{2n\sqrt{2\pi}\beta} \left[\left(\cot\left(\frac{\pi}{2n}\right) F(\beta\rho a^+(\phi^-)) + \cot\left(\frac{\pi}{2n}\right) F(\beta\rho a^-(\phi^-)) \right) \mp \left(\cot\left(\frac{\pi + 2\phi_2}{2n}\right) F(\beta\rho a^+(\phi^+)) + \cot\left(\frac{\pi - 2\phi_2}{2n}\right) F(\beta\rho a^-(\phi^+)) \right) \right] \quad (4.37)$$

For a monostatic system where $\phi_1 = \phi$, and $\phi_2 = \pi - \phi$. The negative (-) on the second term is referred to as soft (parallel) polarization. The positive (+) is referred to as hard (vertical) polarization. The backscattered field for soft and hard polarization is defined as

$$E_{s,h}^d = - \left[D_1^d \frac{e^{-j\beta(\rho+a \cos(\phi))}}{\sqrt{\rho}} + D_2^d \frac{e^{-j\beta(\rho-a \cos(\phi))}}{\sqrt{\rho}} \right] \quad (4.38)$$

The vertical and horizontal polarization backscattered return of an infinite strip of width $2a$ were computed using GTD (Keller), PO, and PO coupled with UTD are

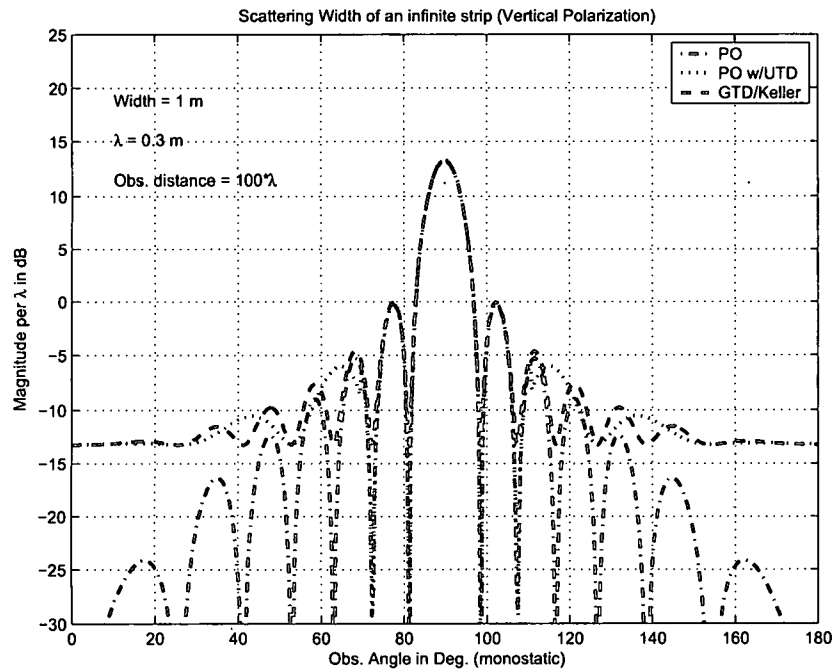


Figure 4.7: Scattering width of an infinite strip (Vertical-Pol)

shown in Figure 4.7 and 4.8 respectively. The beam width decreases as frequency increases, and is limited to low frequency applications or small physical size.

The Geometrical Diffraction Theory assumes localization of the scattering at points defined by stationary phase derived from Keller's expression for scattering from the edge of infinite half-plane [63, 64]. The vertical and horizontal polarization fields backscattered by a perfectly conducting infinite strip are given by [1]

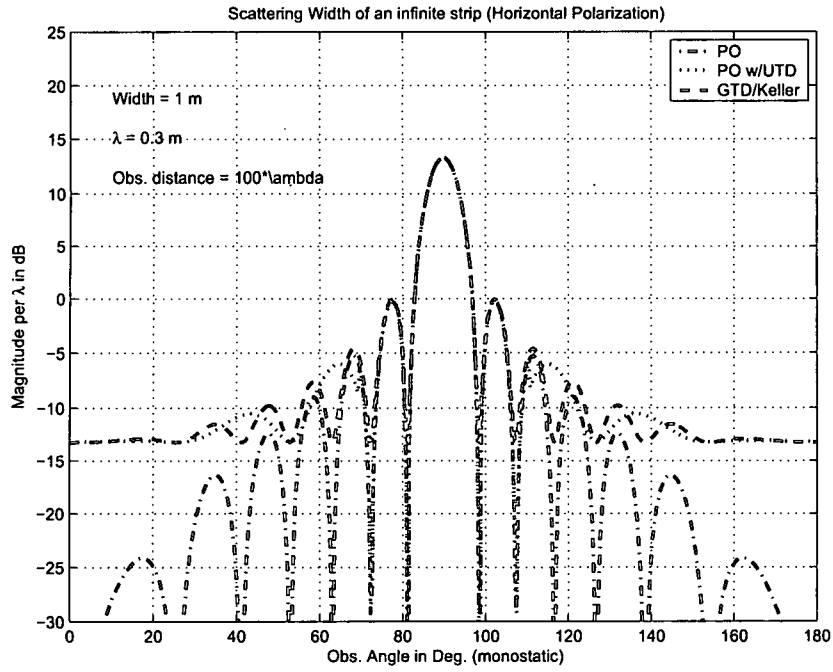


Figure 4.8: Scattering Width of an infinite Strip (Horizontal-Pol)

$$E_v^i = \frac{E_i e^{j(k\rho + \frac{\pi}{4})}}{2\sqrt{2\pi k\rho}} \left\{ \left[\frac{(1 + \sin(\phi))e^{-j2ka \sin(\phi)}}{\sin(\phi)} - \frac{(1 - \sin(\phi))e^{j2ka \sin(\phi)}}{\sin(\phi)} \right] + \left[\frac{E_i e^{jk(\rho 2a)}}{2\pi\sqrt{k\rho}(2ka)^{\frac{3}{2}} \cos(\phi)} + \frac{E_i e^{j(k\rho + 4ka - \frac{\pi}{4})}}{8\pi\sqrt{2\pi k\rho}(2ka)^3} \left(\frac{(1 + \sin(\phi))e^{-j2ka \sin(\phi)}}{(1 - \sin(\phi))^2} + \frac{(1 - \sin(\phi))e^{j2ka \sin(\phi)}}{(1 + \sin(\phi))^2} \right) \right] \left[1 - \frac{e^{j(4ka - \frac{\pi}{2})}}{8\pi(2ka)^3} \right]^{-1} \right\} \quad (4.39)$$

$$E_h^i = \frac{-E_i e^{j(k\rho + \frac{\pi}{4})}}{2\sqrt{2\pi k\rho}} \left\{ \left[\frac{(1 + \sin(\phi))e^{j2ka \sin(\phi)}}{\sin(\phi)} - \frac{(1 - \sin(\phi))e^{-j2ka \sin(\phi)}}{\sin(\phi)} \right] - \left[\frac{2E_i e^{j(k\rho + 2ka + \frac{\pi}{4})}}{\pi\sqrt{k\rho}(2ka)^{\frac{1}{2}} \cos(\phi)} - \frac{E_i e^{j(k\rho + 4ka + \frac{3\pi}{4})}}{\pi\sqrt{2\pi k\rho}(2ka)} \left(\frac{e^{-j2ka \sin(\phi)}}{(1 - \sin(\phi))} + \frac{e^{j2ka \sin(\phi)}}{(1 + \sin(\phi))} \right) \right] \left[1 - \frac{e^{j(4ka + \frac{\pi}{2})}}{2\pi(2ka)} \right]^{-1} \right\} \quad (4.40)$$

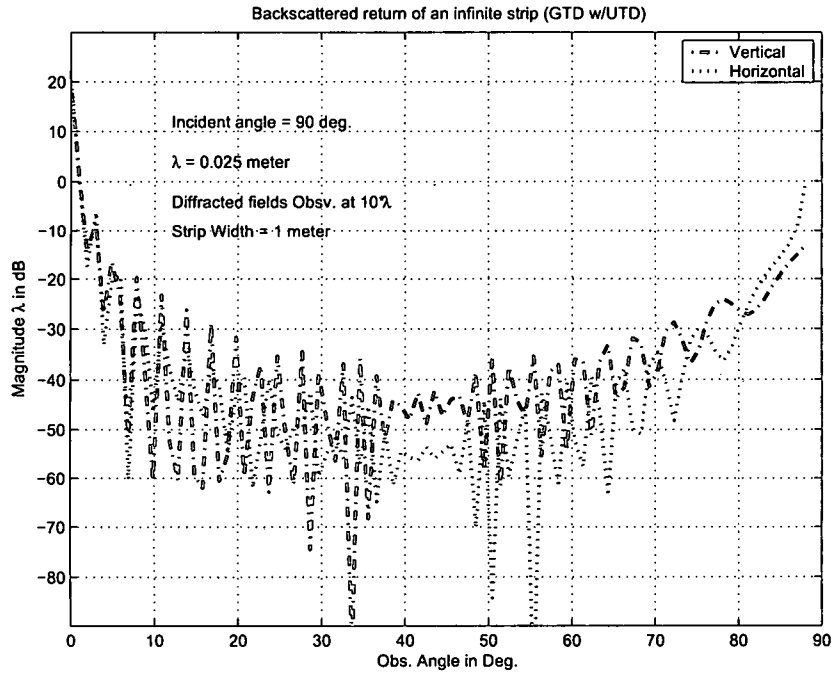


Figure 4.9: Backscattered echo width of an infinite strip

where E_i is the amplitude of incident plane wave, and ρ is the distance from the center of infinite strip to the observation point. The backscattered return of an infinite strip of a width of 1.0 meter is shown in Figure 4.9

A rectangular flat plate of $2a$ by $2b$, derived from the infinite strip flat plate with unit length $2b$ is shown in Figure 4.10

The expression for a rectangular flat plate shown in Figure 4.10 is based on the geometrical diffraction defined by [1] and the vertical and horizontal polarization are given as:

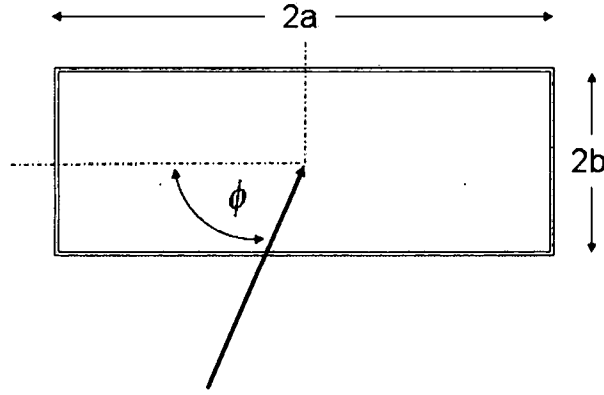


Figure 4.10: A finite rectangular flat plate target

$$\sigma_v(\theta) \approx \frac{4b^2}{\pi} \left| \left[\cos(2ka \sin(\phi)) - j \frac{\sin(2ka \sin(\phi))}{\sin(\phi)} \right] - \left(\frac{e^{j(2ka - \frac{\pi}{4})}}{\sqrt{2\pi}(2ka)^{\frac{3}{2}}} \right) \left[\frac{1}{\cos(\phi)} + \frac{e^{j(2ka - \frac{\pi}{4})}}{4\sqrt{2\pi}(2ka)^{\frac{3}{2}}} \left(\frac{(1 + \sin(\phi))e^{-j2ka \sin(\phi)}}{(1 - \sin(\phi))^2} + \frac{(1 - \sin(\phi))e^{j2ka \sin(\phi)}}{(1 + \sin(\phi))^2} \right) \right] \right|^{-1} \left(1 - \frac{e^{j(4ka - \frac{\pi}{2})}}{8\pi(2ka)^3} \right)^{-1} \right|^2 \quad (4.41)$$

$$\sigma_h(\theta) \approx \frac{4b^2}{\pi} \left| \left[\cos(2ka \sin(\phi)) + j \frac{\sin(2ka \sin(\phi))}{\sin(\phi)} \right] - \left(\frac{4e^{j(2ka + \frac{\pi}{4})}}{\sqrt{2\pi}(2ka)^{\frac{1}{2}}} \right) \left[\frac{1}{\cos(\phi)} - \frac{e^{j(2ka + \frac{\pi}{4})}}{2\sqrt{2\pi}(2ka)^{\frac{1}{2}}} \left(\frac{e^{-j2ka \sin(\theta)}}{1 - \sin(\phi)} + \frac{e^{j2ka \sin(\theta)}}{1 + \sin(\phi)} \right) \right] \right|^{-1} \left(1 - \frac{e^{j(4ka + \frac{\pi}{2})}}{2\pi(2ka)} \right)^{-1} \right|^2 \quad (4.42)$$

Note that the field contributions by the incident and reflected diffracted fields are small in comparison to the incident and reflected fields.

A finite rectangular plate having a well defined backscattered echo width is used to illustrate the Stochastic random mutation process with the goal of obtaining a minimized function while operating under a set of parameter constraints. A

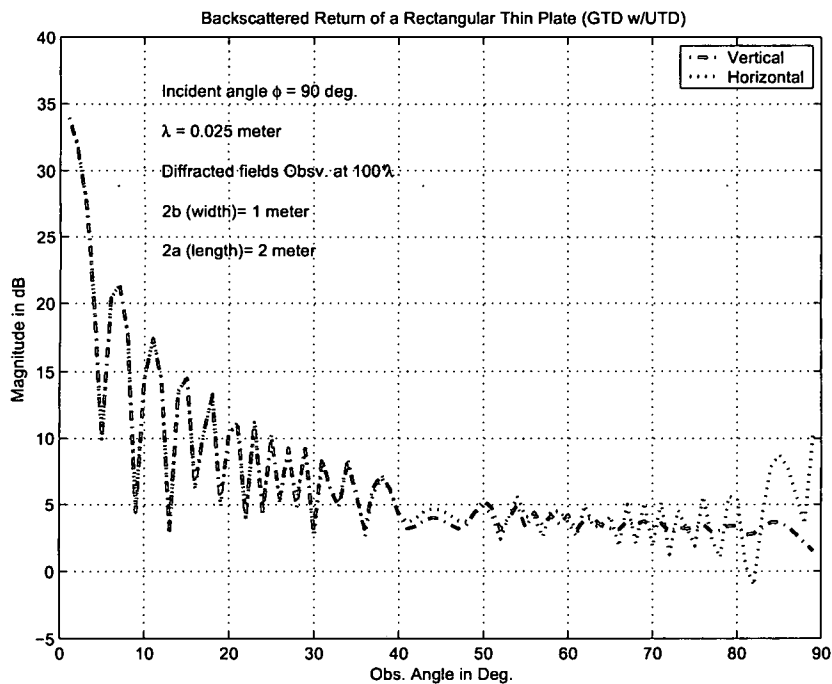


Figure 4.11: Backscattered field of a rectangular plate

rectangular plate having dimension of $2a$ by $2b$ as shown in Figure 4.10 with its backscattered field return is shown in Figure 4.11. An investigation of the scattering from a square plate [1] has been carried out to determine the analytical formulation for predicting the backscattered echo width. Figure 4.13 is the monostatic measurement (vertical and horizontal polarization) of the cross section of a square flat plate vs. the azimuth ration angle ϕ in degree. The plot also contains the backscattered echo width based on physical optics theory [55] and geometrical diffraction theory [64] where the magnitude peaks at the specular ($\phi = 0^\circ$) are independent of polarization and increases with the plate size. The vertical and horizontal polarization backscattered echo width computed based on uniform diffraction theory are shown in Figure 4.14 and Figure 4.15 respectively. Figure 4.12

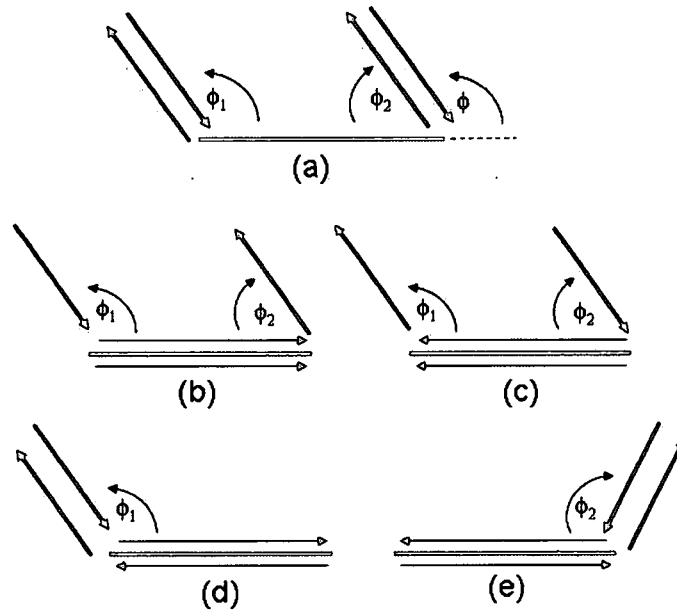


Figure 4.12: Diffraction field of a flat plate (a) Single Order; (b)&(c): 1st order multiple; (d)&(e): 2nd order multiple

depicts the multiple order diffractive terms of the backscattered return (using UTD method). In the horizontal case, the total fields are the sum of multiple order diffractive fields, whereas, for the vertical case, only a single order is needed. The objective is to minimize its backscattered width within the given constraints while retaining the optimal functions in a multi-disciplinary design optimization process. In the general case, the width and height of a given rectangular plate can be altered to produce a lower backscattered field return while maintaining its total surface area dictated by the Aero constraints.

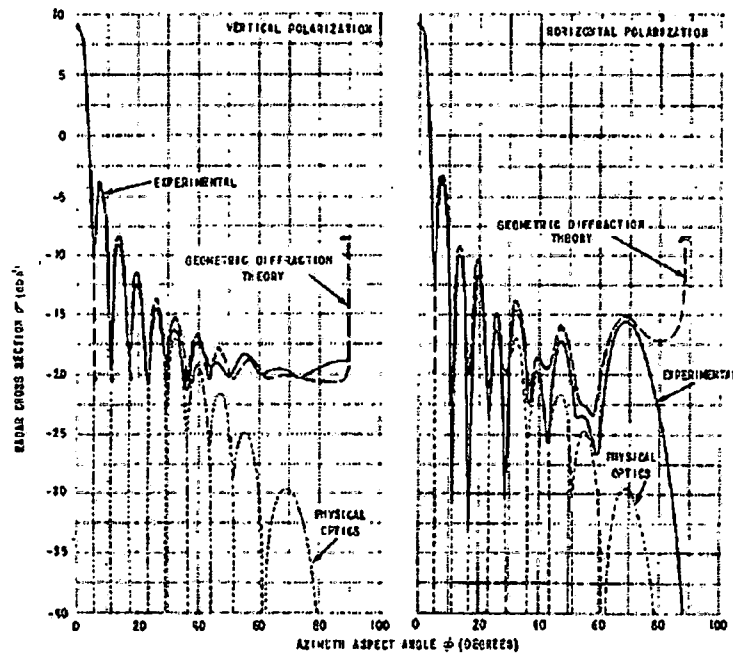


Figure 4.13: Backscattered return of a 6.5 x 6.5 inch flat plate [1]

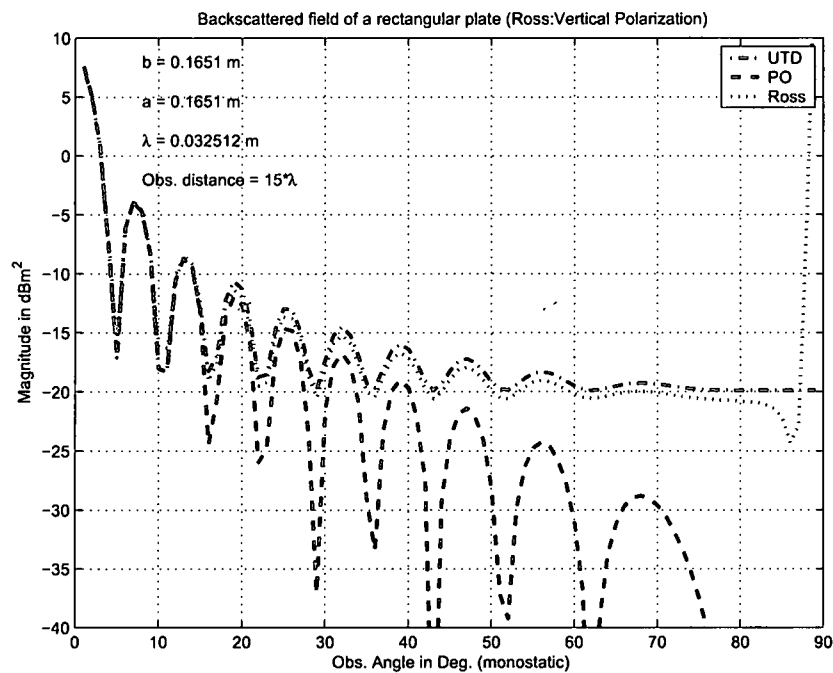


Figure 4.14: Backscattered return of a 6.5 x 6.5 inch flat plate (Vertical Pol.)

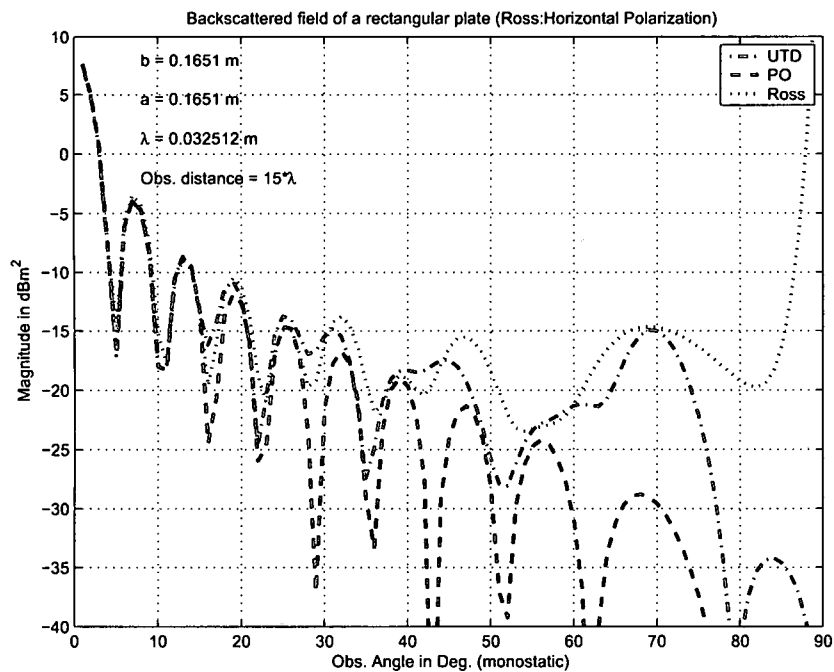


Figure 4.15: Backscattered width of a 6.5 x 6.5 inch flat plate (Horizontal Pol.)

CHAPTER 5

WING OF FINITE PLANFORM

The performance of spacecraft continues to reach new heights with advanced computer aided design tools, simulation, and test facilities. Flight Optimization System, an aircraft configuration program for conceptual design and assessment [65], illustrates the detailed optimization modules of the overall aircraft performance including weight, aerodynamics, and propulsion data. Many innovative design approaches and quantitative functional simulations play an important role in the development of high performance military spacecraft. An optimal set of geometric parameters was investigated by [66] showing the impact of the fuselage fineness ratio, the nose to body length ratio, the nose to camber value, the wing planform area scale factor and the wing location. The objective of this paper is to introduce the concept of coupling the EM discipline into the design process, where the return of the electromagnetic backscattered field would be an additional design variable. Much of the numerical data of aircraft wing shapes are readily available and it is outside the scope of this paper to describe the analytical or experimental data of the aerodynamic performance of various planform wing shapes as shown in Fig 5.1. The aerodynamic characteristics of a given geometrical wing shape are determined by the airfoil section distribution, the aspect ratio, the taper ratio, the twist, and the sweep back of the planform. The primary purpose of this research is

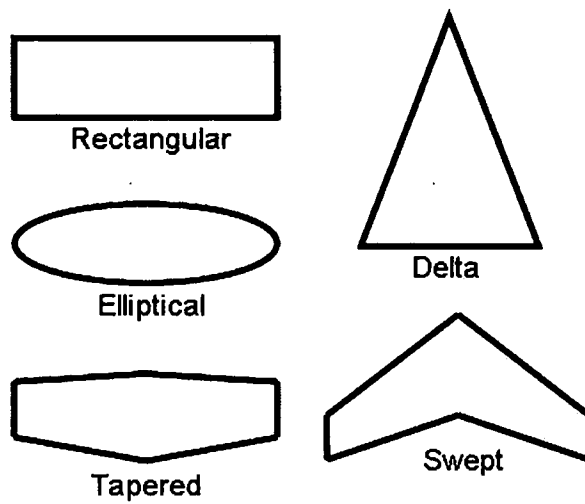


Figure 5.1: Various geometric wing planforms

to illustrate the potential utility of the Stochastic Mutation Algorithm in the design optimization among two distinctive disciplines, namely Aero and EM disciplines, and its coupling effort aimed at improving the method in multidisciplinary design and optimization. It is intended to improve efficiency in the design process. Equations were cited to establish their relevance in the context of MDO and were given without derivation or proof.

The basic characteristics of a finite rectangular wing platform shown in Figure 5.2 are used to illustrate the effect of optimizing the electromagnetic backscattered field for the given physical shape. Some of the fundamental aerodynamic principles and equations will be cited without giving in-depth derivation. The geometry of the rectangular wing shown in Figure 5.2 is used to illustrate the design constraint parameters in the optimization computational process.

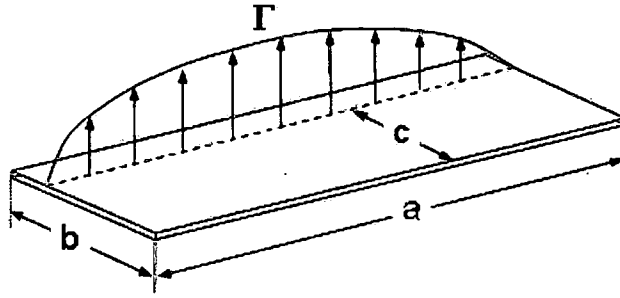


Figure 5.2: Rectangular wing spanwise distribution

5.1 LIFT COEFFICIENT

The free stream dynamic pressure of a fluid with air density ρ_∞ and airspeed V_∞ is defined [67] as

$$q_\infty = \frac{1}{2} \rho_\infty V_\infty^2 \quad (5.1)$$

where the dynamic pressure q_∞ is a function of flight conditions and is a function of control environment in terms of true airspeed within a given geometric altitude.

Consider the lifting of a thin, finite wing shown in Figure 5.3 that is moving at a constant airspeed and at a given altitude. The lift of spanwise circulation distribution for $0 \leq \theta \leq \pi$ can be evaluated since the spanwise location is proportional to the local lift along the lifting line. It can be expressed in terms of the Fourier Sine series and is given by [68] and [69] as

$$\Gamma(\theta) = 2aV_\infty \sum_{n=1}^N A_n \sin(n\theta) \quad (5.2)$$

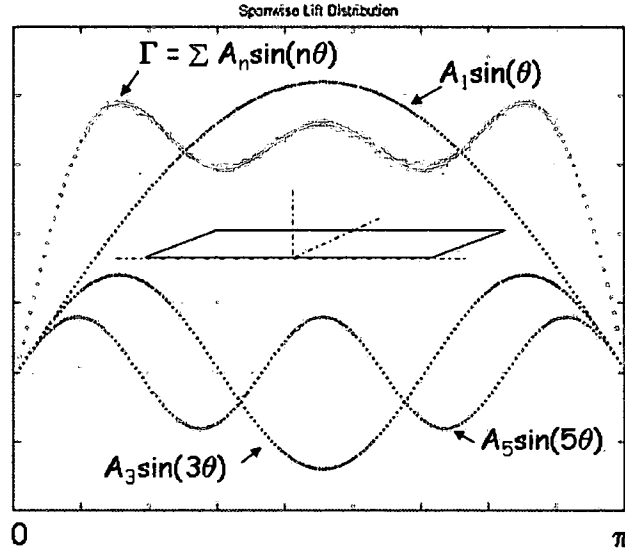


Figure 5.3: Symmetric spanwise lift distribution presented by a Fourier Sine series [2]

and the lift coefficient defined by [70]

$$C_\ell = \frac{a}{V_\infty S} \int_0^\pi \Gamma(\theta) \sin(\theta) d\theta \quad (5.3)$$

where S is the wing surface area and V_∞ is the airspeed. Substitute Equation (5.2) into (5.3)

$$C_\ell = \frac{2a^2}{S} \sum_1^N A_n \int_0^\pi \sin(n\theta) \sin(\theta) d\theta \quad (5.4)$$

where the integral term of $\int_0^\pi \sin(n\theta) \sin(\theta) d\theta$ equals to $\frac{\pi}{2}$ for $n = 1$, and 0 for $n \neq 1$. Hence Equation (5.4) can be written as

$$C_\ell = \frac{A_1 a^2 \pi}{S} \quad (5.5)$$

and the lift coefficient is mainly dependent on the leading coefficient of Fourier sine series expansion. In the case of an airfoil in a steady flow, the lift per unit span is

directly related to the circulation around the shape, known as the Kutta-Joukowski lift theorem. Thus the total lift is defined by integrating over the entire span of the wing, and the determination of the number of terms in coefficient A_n is based on the accuracy requirement. Since the spanwise direction is given by θ and the lift distribution is represented by Fourier sine series. Let N be the different spanwise stations and then obtain independent algebraic terms from A_1, A_2, \dots, A_n unknowns. Then the lift coefficient in Equation (5.4) can be expressed in terms of the numerical value satisfying the fundamental equation of Prandtl's lifting-line theory of a finite wing [68].

5.2 DRAG COEFFICIENT

Aerodynamic drag falls into three primary categories: wing profile drag, parasite drag, and induced drag. Wing profile drag varies with the airfoil section which is associated with maximum cruising range and high-performance spacecraft. Parasite drag, known as catch-all drag [71], includes skin friction drag, pressure field drag, separation drag, and interference drag, all of which have little to do with lift. However, induced drag is of particular interest because it is composed of two physical elements, wing surface area and aspect ratio. It is a major contributing source of aerodynamic drag of the finite wing.

The effective angle of attack α_e seen in Figure 5.4 is the angle between the chord line and the relative velocity V_r . The local lift force F acts normal to the relative flow direction, and the induced drag is created as the result of the presence of the downwash D_w due to the induced angle of attack α_i . Since the finite wing operates

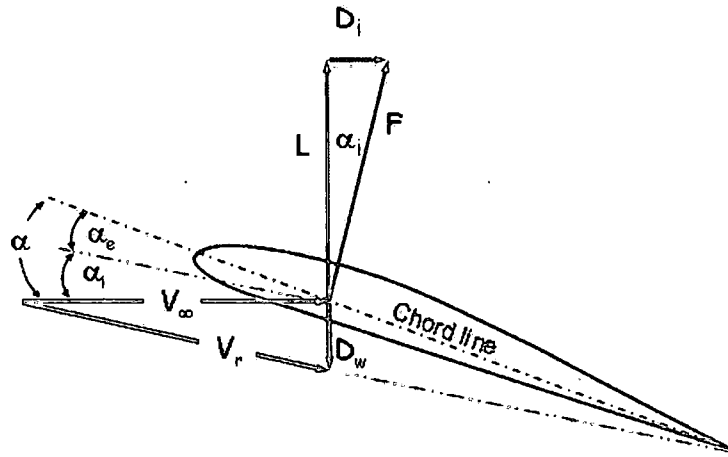


Figure 5.4: Induced flow on a finite wing

at a lower angle of attack than the infinite wing due to the depressed relative wind flow at the airfoil center, the angle of attack for a finite wing must be increased by α_i to produce the same lift coefficient as the infinite wing. The vector acting perpendicular to the flight path is the lift, and the vector acting backward along the flight path is drag force. The induced drag coefficient can be obtained similarly from Equation (5.4) and is given by [68]

$$C_d = \frac{2a^2}{S} \sum_1^N A_n \int_0^\pi \sin(n\theta) \sin(\theta) \alpha_i(\theta) d\theta \quad (5.6)$$

where $\alpha_i(\theta)$ is the induced angle of attack in term of circulation distribution along the wing and it is defined by [72] as

$$\alpha_i(\theta) = \sum_1^N k A_k \frac{\sin(k\theta)}{\sin(\theta)} \quad (5.7)$$

hence, Equation (5.6) can be re-written as

$$C_d = \frac{2a^2}{S} \int_0^\pi \left(\sum_1^N A_n \sin(n\theta) \right) \left(\sum_1^N k A_k \sin(k\theta) \right) d\theta \quad (5.8)$$

and the integral product term $\int_0^\pi \sin(n\theta) \sin(k\theta) d\theta$ equals to $\frac{\pi}{2}$ for $n = k$, and 0 for $n \neq k$. The coefficients of Fourier sine series product terms are zero except the leading term. Thus Equation (5.8) becomes

$$C_d = \frac{a^2 \pi}{S} \left(\sum_1^N n A_n^2 \right)$$

$$C_d = \frac{a^2 \pi}{S} A_1^2 \left[1 + \sum_2^N n \left(\frac{A_n}{A_1} \right)^2 \right] \quad (5.9)$$

Substituting Equation (5.5) into (5.9) to obtain

$$C_d = \frac{C_\ell^2 S}{a^2 \pi} (1 + \sigma) \quad (5.10)$$

where the induced drag factor is defined as

$$\sigma = \sum_2^N n \left(\frac{A_n}{A_1} \right)^2 \geq 0 \quad (5.11)$$

Equation (5.10) is the general drag coefficient of a finite wing, where lift distribution yields minimum induced drag at $\sigma = 0$. For a symmetrical loading distribution, only the odd terms of the Fourier Series need be considered [69]. Since not all wings have the same shape or efficiency, span or Oswald efficiency factor accounts for the design variance among wing planform, and is defined as

$$e = \frac{1}{1 + \sigma} \quad (5.12)$$

the theoretical maximum span efficiency e is 1 when $\sigma = 0$.

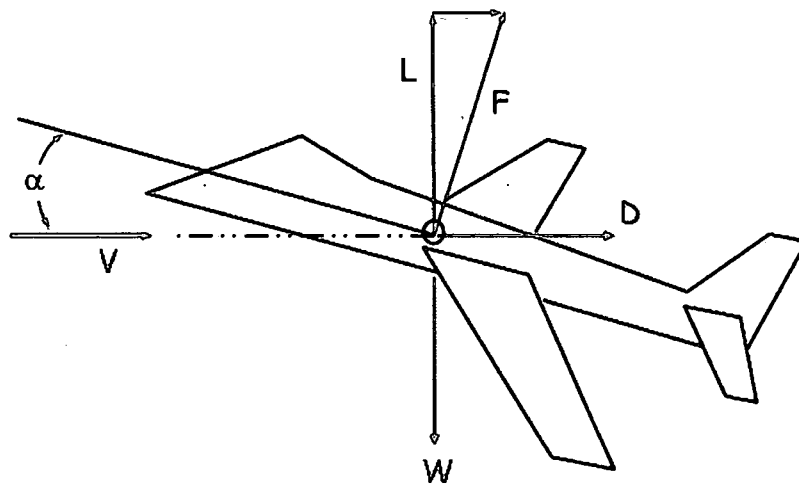


Figure 5.5: Simple geometry Illustrating Lift Force of an aeroplane

5.3 LIFT DISTRIBUTION OF A FINITE WING PLANFORM

The computation of the lift coefficient could be very complex due to many factors that affect the turning of the flow, which generates lift. Factors such as wing geometry (shape, size, mass), aerodynamic force (velocity, inclination, viscosity, compressibility), and the properties of air are also considered. Figure 5.5 depicts the general concept of an aeroplane lift force. With the reference of center of pressure at which the resultant aerodynamic force F acts, the lift component, L , is perpendicular to the velocity vector, V , whereas the drag component, D , is parallel.

The main factor affecting lift is the geometric shape of an object. For a conventional sub-sonic aeroplane with a reasonable high aspect ratio wing, it was noted that the wing and fuselage behave aerodynamically like a wing alone [73] with a very satisfactory lift approximation. The aerodynamic force due to angle of attack

is at the quarter chord point of the wing and varies directly with the angle of attack at angles below the stall. However, the lift created by the wing shape must be greater than the weight, W , for a given air velocity at a given altitude. It is noted that at high speed, α is generally small since a large contribution to the aerodynamic force is due to the camber dependent component where center of pressure is near the mid point of the chord. Refer to Figure 5.2 where the spanwise lift distribution is symmetrical, hence, the lift on the wing is defined by [2]

$$L = \frac{a}{2} \rho_{\infty} V_{\infty} \int_0^{\pi} \Gamma(\theta) \sin(\theta) d\theta \quad (5.13)$$

Consider a symmetrical loading distribution represented by the sine series, and using the Fourier Sine series for Equation (5.2), Equation (5.13) can be written as

$$L = a^2 \rho_{\infty} V_{\infty}^2 \int_0^{\pi} \left(\sum_1^N A_n \sin(n\theta) \right) \sin(\theta) d\theta \quad (5.14)$$

taking the integral of Equation (5.14),

$$L = a^2 \rho_{\infty} V_{\infty}^2 \left\{ A_1 \left[\frac{\theta}{2} + \frac{\sin(2\theta)}{4} \right] \Big|_0^{\pi} + \sum_3^N \frac{1}{2} A_n \left[\frac{\sin(n-1)\theta}{n-1} - \frac{\sin(n+1)\theta}{n+1} \right] \Big|_0^{\pi} \right\}$$

$$L = a^2 A_1 \pi \left(\frac{1}{2} \rho_{\infty} V_{\infty}^2 \right) \quad (5.15)$$

and note that the summation represented by the second term on the right-hand side is zero for $n \neq 1$. Hence, Equation (5.15) primarily depends on the leading coefficient of the Fourier sine series regardless of all other terms present in the series describing the distribution. Substitute Equations (5.1) and (5.5) in Equation (5.15)

$$L = C_l S q_{\infty} \quad (5.16)$$

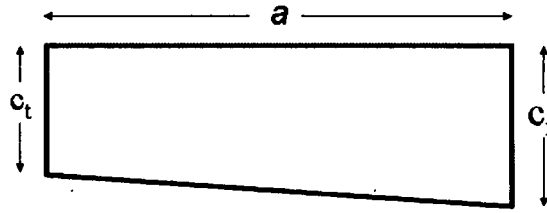


Figure 5.6: Linearly Tapered Wing

Equation (5.16) is a function of lift coefficient, dynamic pressure, and wing surface area. The induced drag, which is produced by integrating the spanwise of the lift component in the streamwise direction is defined as

$$D = C_d S q_\infty \quad (5.17)$$

For a linearly tapered wing shown in Figure 5.6, the taper ratio is defined as the ratio of tip chord to root chord

$$TR = \frac{c_t}{c_r} \quad (5.18)$$

and the wing surface area of the spanwise tapered wing is

$$S = \begin{cases} 0.5c_r(1 + TR)a & \text{for taper wing} \\ ba & \text{for rectangular wing} \end{cases} \quad (5.19)$$

and the aspect ratio where the chord varies along the spanwise of a finite wing [4] is defined as

$$AR = \begin{cases} \frac{2a}{(c_r + c_t)} & \text{for taper wing} \\ \frac{a^2}{S} & \text{for rectangular wing} \end{cases} \quad (5.20)$$

hence Equation (5.5) can be written as

$$C_\ell = A_1\pi(AR) \quad (5.21)$$

and the induced drag coefficient in Equation (5.10) is re-written as

$$C_d = \frac{C_\ell^2}{\pi(AR)}(1 + \sigma) \quad (5.22)$$

thus both lift and induced drag coefficients are functions of the wing aspect ratio, wing shape, and the first coefficient of the Fourier Sine series. The induced drag factor of Equation (5.11) is a function of taper ratio of a finite wing for a given aspect ratio. A high aspect ratio (long slender) wing has a lower induced drag than low aspect ratio wings. In lifting line theory [67] and [74], the minimum induced drag occurs at $AR = 0.35$.

5.4 LIFT AND DRAG ANALYSIS

In practice the need for airframe performance verification continues. One program, FoilSim II shown in Figure 5.7, was developed by the NASA Glenn Research Center. FoilSim II is an interactive simulation program that examines the airflow around various shapes of airfoils, including flat plate. The program will calculate lift based on the parameters such as airspeed, altitude, angle of attack, airfoil shape, wing surface area, and wing aspect ratio.

Table 5.1 and 5.2 compared the computed lift coefficient of a finite, thin rectangular wing with those data generated by FoilSim II simulation program shown in Figure 5.7. The variance among both sets of lift coefficients was less than 1 %. The agreement among the data sets validated the developed MatLab M-codes

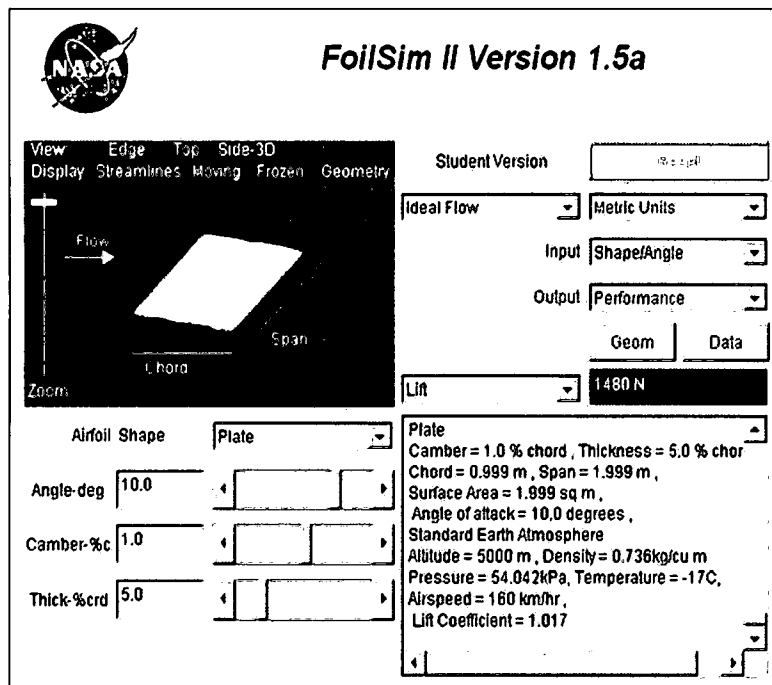


Figure 5.7: NASA FoilSim II Simulator Data Display

(shown in Appendix A) and established the fundamental understanding on the basic physical parameters that affect the lift force. The computed data presented in this section will be used to compare various experimental and measured data. To demonstrate the coupling effect among the Aero and EM disciplines, input parameters that have the most relevant impact on both aerodynamics performance and EM discipline will be considered.

As discussed in previous sections, the lift and induced drag coefficient due to the angle of attack α is shown in Table 5.1, and the effect due to wing aspect ratio AR shown in Table 5.2 are two physical Aero design variables. The wing shape and wing surface area are used to compute the theoretical lift coefficient as a function of angle of attack of an unswept wing of NACA 65-210 [2] is shown in Figure 5.8, and

Table 5.1: C_ℓ as Function of α for $AR = 2$ and $\alpha_{lo} = -1.2^\circ$

α	C_ℓ^{Fsim} (FoilSim II)	C_ℓ^{Comp} (Computed)	Variance%
0	0.123	0.123	0.000
1	0.226	0.226	0.000
2	0.326	0.327	0.307
3	0.423	0.424	0.236
4	0.517	0.517	0.000
5	0.607	0.608	0.165
6	0.695	0.696	0.144
7	0.779	0.782	0.385
8	0.861	0.865	0.465
9	0.941	0.945	0.425
10	1.017	1.023	0.590
11	1.092	1.099	0.641
12	1.164	1.172	0.687
13	1.234	1.244	0.810
14	1.301	1.313	0.922

the lift as a function of induced drag coefficient is shown in Figure 5.9. Note that in Figure 5.8 the zero lift angle of attack is approximately -1.2° across the wingspan as given in [75]. Since the wing is untwisted, the geometric angle of attack is the same at all spanwise positions and the lift distribution can be represented by the Fourier Sine Series as shown in Figure 5.3.

The computed or estimated lift coefficient as a function of angle of attack and induced drag coefficient are shown in Figures 5.12 and 5.13, respectively. The computed data yielded similar values to those data shown in Figures 5.8 and 5.9. Furthermore, the estimated lift coefficient was also in close agreement with the data shown in Figures 5.10 and 5.11 obtained by the www.3DFoil.com software

Table 5.2: C_ℓ as Function of AR for $\alpha = 5^\circ$ and $\alpha_{lo} = -1.2^\circ$

AR	C_ℓ^{Fsim} (FoilSim II)	C_ℓ^{Comp} (Computed)	Variance %
2.000	0.607	0.608	0.214
2.170	0.611	0.613	0.327
2.363	0.615	0.618	0.407
2.583	0.621	0.622	0.145
2.835	0.625	0.626	0.192
3.125	0.629	0.630	0.207
3.463	0.633	0.634	0.190
3.858	0.637	0.638	0.173
4.325	0.641	0.642	0.109
4.883	0.644	0.645	0.186
5.556	0.647	0.649	0.232
6.378	0.650	0.652	0.246
7.396	0.653	0.655	0.230
8.681	0.656	0.657	0.198
10.331	0.659	0.660	0.121
12.500	0.661	0.662	0.182
15.432	0.663	0.664	0.196
19.531	0.665	0.666	0.180
25.510	0.667	0.668	0.135

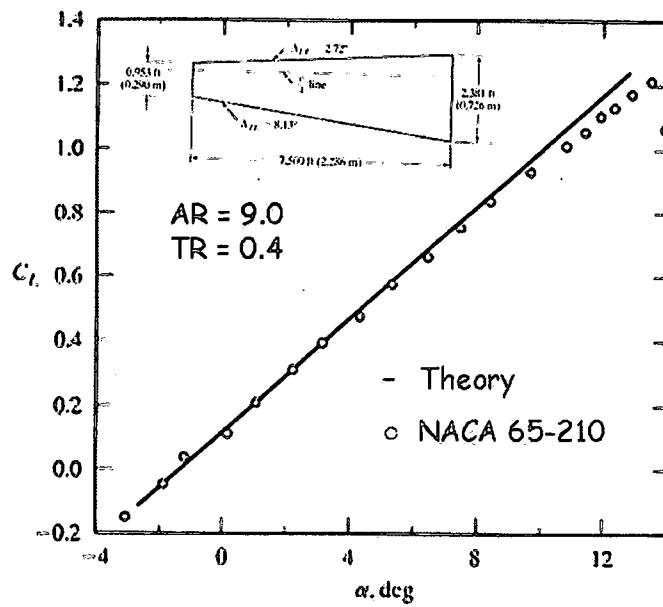


Figure 5.8: Theoretical and experimental C_l as function of α of unswept tapered wing [2]

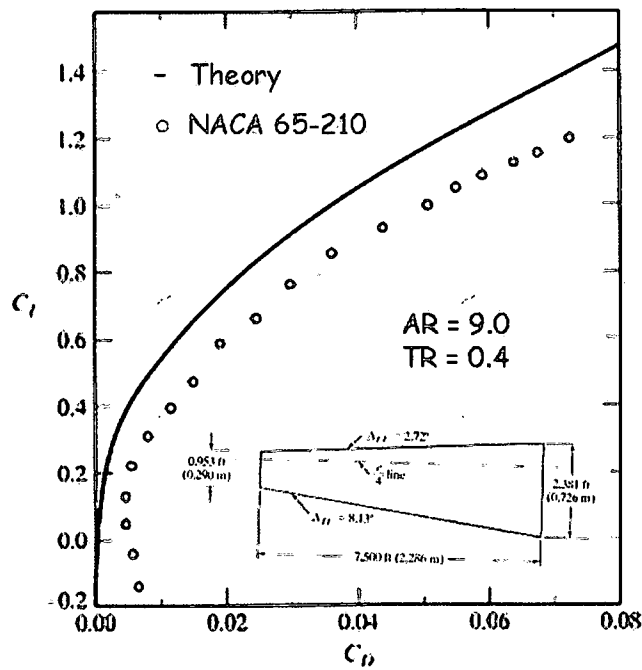


Figure 5.9: Theoretical and measured C_l as function of C_d of unswept tapered wing [2]

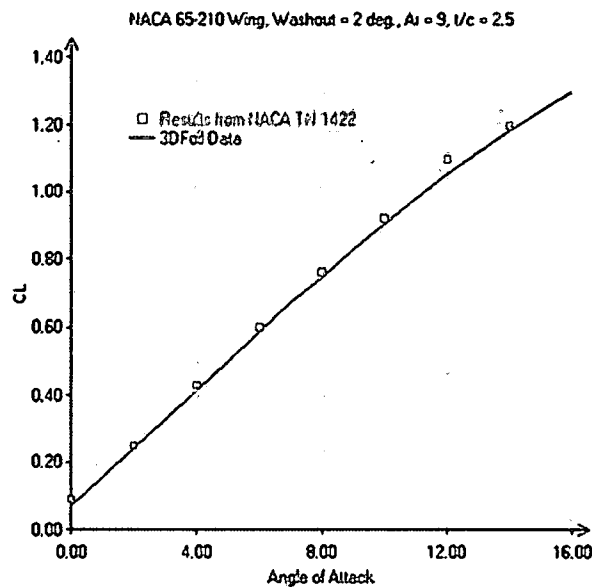


Figure 5.10: Calculated C_l as function of α of unswept tapered wing [3]

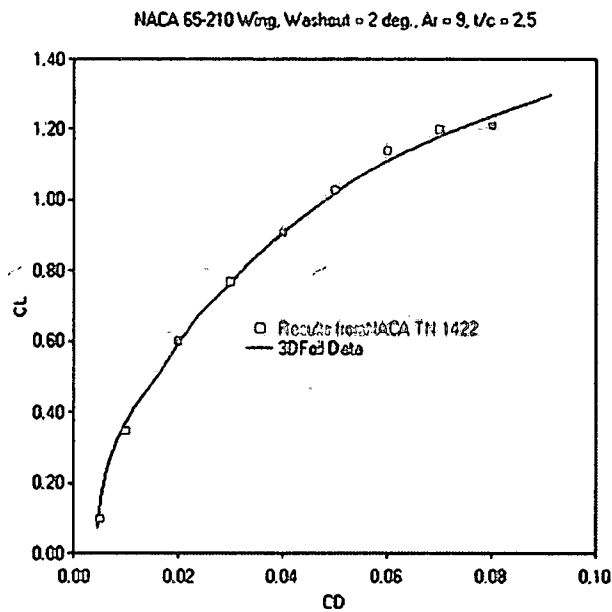


Figure 5.11: Calculated C_l as function of C_d of unswept tapered wing [3]

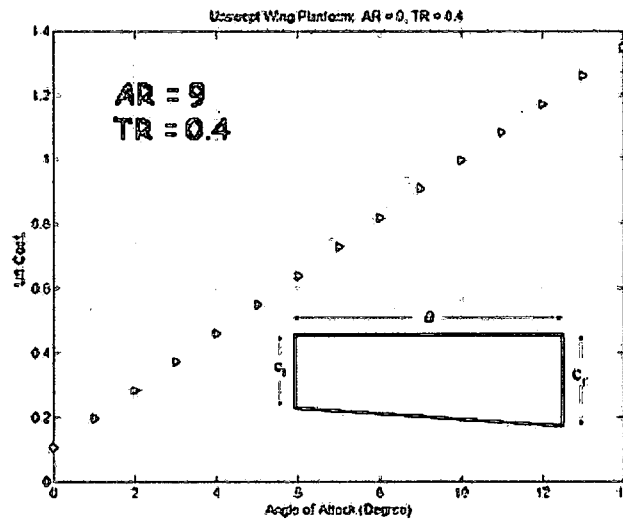


Figure 5.12: Computed lift coefficients of unswept tapered wing

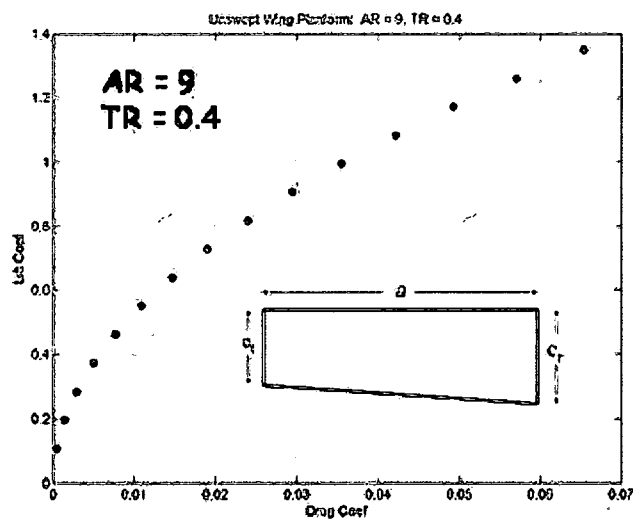


Figure 5.13: Computed induced drag coefficients of unswept tapered wing

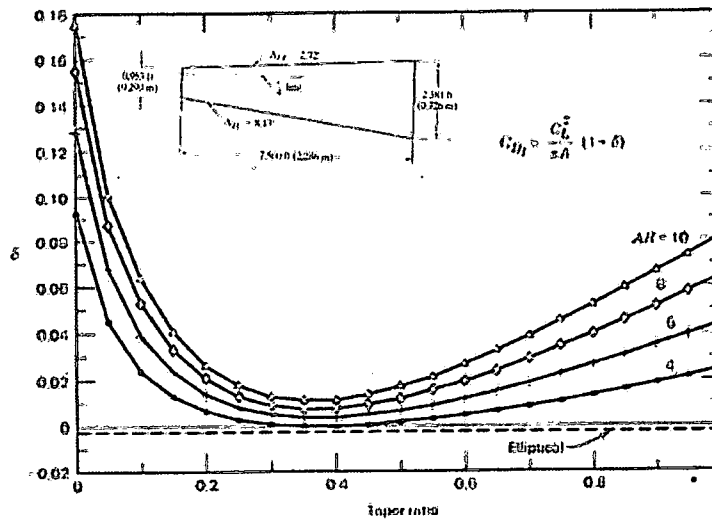


Figure 5.14: Numerical induced drag factor for a linearly tapered wing [4]

program [3], a twisted wing tip with 2° washout angle. All data were very well matched with those experimental values reported in [76].

For a given wing aspect ratio and lift coefficient as shown in Equation (5.21), which is for an arbitrary wing shape where the induced drag factor σ is normally small, the numerical calculation of induced drag factor as a function of wing taper ratio TR is shown in Figure 5.14. The calculations were first published by Hermann Glauert in 1926 by [77] and the numerical computation by [4]. Note that the rectangular wing is represented by $TR = 1$.

The computed induced drag factor (by MatLab M-code in Appendix A) is shown in Figure 5.15 with zero lift angle of attack $\alpha_{lo} = -1.2^\circ$. Since the wing is untwisted, the geometric angle of attack α is the same at all spanwise positions.

Both Figures 5.14 and 5.15 have the minimum induced drag factor at approximately $TR = 0.35$, which is close to the elliptical wing distribution shown

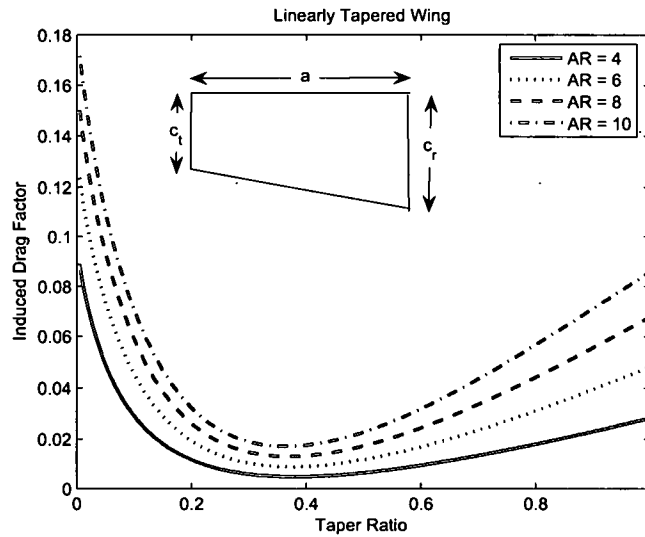


Figure 5.15: Computed induced drag factor of a tapered wing

in [78] where induced drag factor in Equation (5.11) was used to compute the induced drag as function of lift is shown in Figure 5.17.

$$C_d = \frac{C_l^2}{\pi(AR)} \quad (5.23)$$

Equation 5.23 represents the minimum induced drag for a wing where the elliptic lift distribution is optimum from the viewpoint of induced drag. Drag due to lift, as the term indicates, is associated with the generation of lift and it is predominantly induced by many variants [79] such as the lifting line, the pressure difference between lower and upper sides of a lifting wind, downwash angle where the optimum lift distribution over the span of a wing providing maximum lift on a given angle of attack, and wing shape, where a reduced drag can be obtained by increasing the wing span (higher aspect ratio). For a thin rectangular wing, the

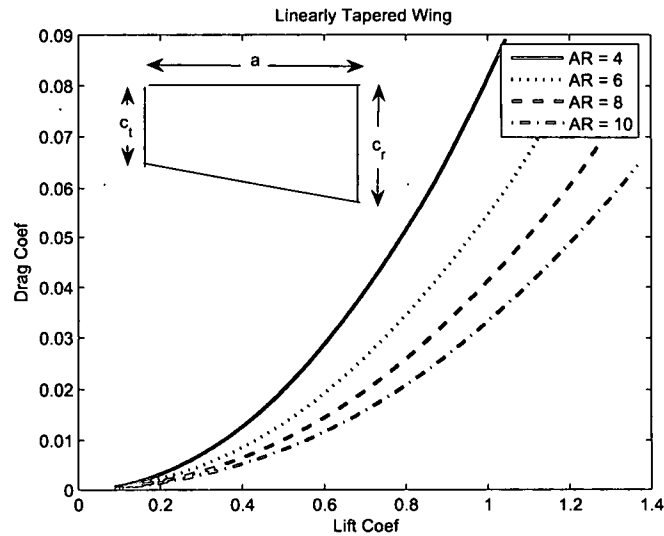


Figure 5.16: Computed induced drag C_d as function of lift C_l and aspect ratio of tapered wing

pressure force is normal to the wing plate surface and the induced drag due to lift is the component of the normal force as shown in Figure 5.5.

Given a constant weight and powerplant, the most efficient and optimal approach to attain increasing climb (large lift) is through drag reduction. At -1.2° induced angle of attack at zero lift, the computed (Aero code) induced drag as a function of lift variation is shown in Fig 5.16, which has similar characteristics as the theoretical drag value shown in Figure 5.17.

Referring to Figure 5.2 and the NASA FoilSim II simulator shown in Figure 5.7, the computed lift coefficients for various wing aspect ratio, angle of attack, and wing surface area were validated to ensure accuracy against the developed MatLab codes. The lift and drag force generated by the wing planform is dependent on angle of attack, the wing shape, air density, airspeed, and wing planform surface area.

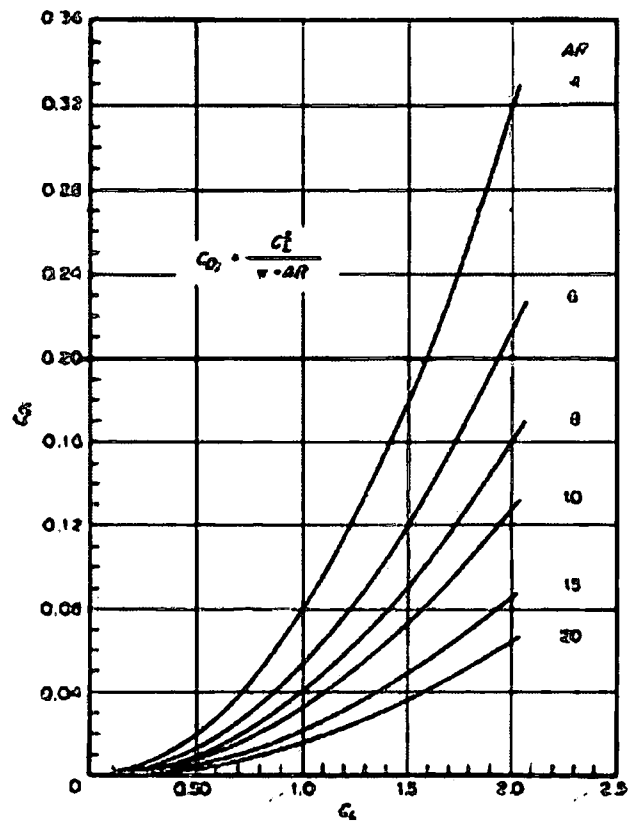


Figure 5.17: Theoretical induced drag C_d variation with lift C_l and wing aspect ratio

CHAPTER 6

DESIGN OPTIMIZATION IN COUPLING AERO AND ELECTROMAGNETIC DISCIPLINES

Multidisciplinary Design Optimization (MDO) has emerged as a numerical analysis tool in aircraft design to meet the demands in aerodynamic performance and cost. The development in design and optimization focuses on decomposing a large complex system into several smaller sub-systems through the coupling effects among the disciplines within. Optimization in aircraft design among aerodynamics, structure, control, and propulsion remains a great challenge to numerical optimization. The computation power required to accurately model each discipline and predict aircraft performance is intensive and cost prohibitive. The development of multidisciplinary design optimization (MDO) using Genetic Algorithms or Evolutionary Algorithms has many applications in aircraft design. The aircraft wing planform based on Evolutionary Algorithms optimizing multiple variables including aerodynamics, structure, control, and propulsion have shown promise in predicting aircraft performance with great accuracy [80] with intensive computation. It has been shown that the aero function is very sensitive to wing geometry and requires simultaneous optimization of multiple components. MDO has been applied in aerodynamic performance optimization and in aircraft design, where it has been used to facilitate system performance and life cycle cost [81]. It has also been used in a workflow based process [82] of a complex engineering system. The MDO utilizing

Stochastic Mutation Algorithm (SMA) provides a method to link the disciplinary analysis and optimal system design with a distinct optimization framework.

In general, MDO comprises of three primary elements: 1) data model & management; 2) conceptual design & analysis, and 3) design approximation & optimization. In practice, the problem of minimizing one function while maximizing the other concurrently is challenging, especially in applications with a large number of variables. The investigation of partitioned quasi-Newton method for large scale unconstrained optimization by J. Necedal and the Stochastic Global (SG) optimization utilizing parallel computation by S.L. Smith, E. Eskow, and R.B. Schnabel [83] showed promise in designing fast and robust algorithms for large unconstrained optimization problems and execution time reduction in solving global optimization problems. In this paper, the objective of the optimization statement is to couple the Aero and EM performance function in a multidisciplinary problem bounded by its design variables and constraints where the performance function is defined by

$$F(X) = F(x_1, x_2, \dots, x_n) \quad (6.1)$$

subject to the constraint

$$G(X) = g_j(x_1, x_2, \dots, x_n) \leq c_j \quad (6.2)$$

for $j = 1, 2, \dots, m$ where $F(X)$ is the performance function, $G(X)$ is the constraint imposed by aerodynamic and structural performance, and x is the design variable.

The state flow diagram of the Stochastic Mutation Algorithm (SMA) shown in Figure 6.1 depicts the cross-discipline between the Aero and EM discipline where \bar{X}^o is the input design variable vector, \bar{v} is the weighting factor associated with the

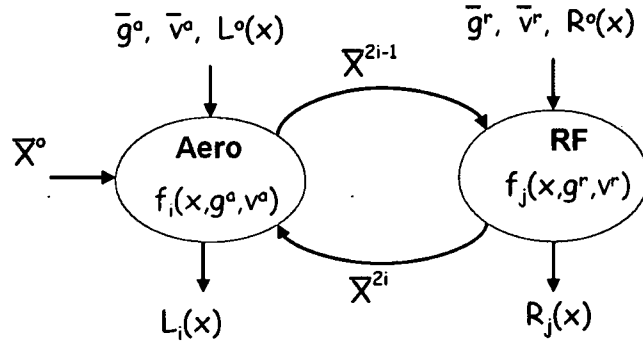


Figure 6.1: Stochastic Mutation Algorithm Optimization state flow

design vector and \bar{g} is the design variable constraint. The initial design goal for the Aero discipline is represented by $L^o(\bar{X})$. The objective is to render an optimal Aero solution where $L_i(\bar{X}) > L^o(\bar{X})$ is the desired design goal derived by the Stochastic algorithm. The mutation method will seek and retain the optimal value through the trial process.

The interaction design variable vector, $\bar{X}^{(2i-1)}$, applies to both Aero and EM disciplinary design optimization. The design variable vector iterates and its value is retained whenever a desirable Aero solution is detected. The current state of $\bar{X}^{(2i-1)}$ is then passed on to the EM discipline to compute the RCS value in the EM discipline section. The variable \bar{v}^r is the weighting factor applied to $\bar{X}^{(2i-1)}$ and \bar{g}^r is the constraint associated with the EM function in meeting $R^o(\bar{X})$, the initial minimum RCS value. Once $R_j(\bar{X}) < R^o(\bar{X})$ is obtained, then $\bar{X}^{(2i)}$ is passed back to Aero section to re-evaluate $L_i(\bar{X})$.

The SMA process flow is shown in Figure 6.2. The process re-iterates until a set of optimum design variables \bar{X} is obtained where both functions $L_i(\bar{X})$ with respect to the Aero discipline and $R_j(\bar{X})$ with respect to the EM discipline meet the design

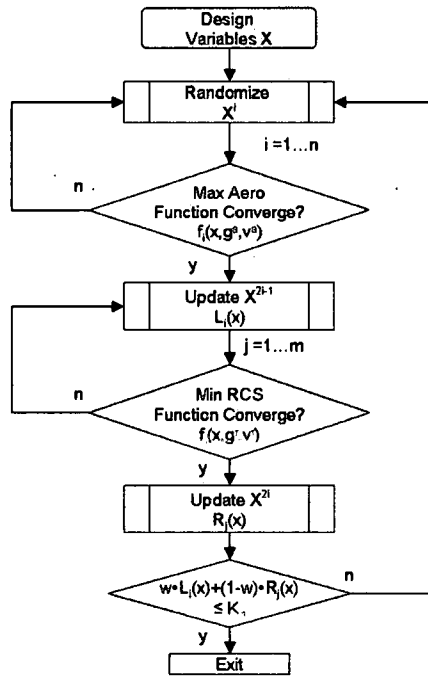


Figure 6.2: Stochastic Mutation Algorithm Optimization decision tree flow

criteria. The cross-disciplinary weighting factor w was included to provide additional robustness in the design decision process, and K_d is the design threshold (score) which gauges the overall design objective.

If the subcomponent constraint defined by a step function is

$$g(x, x_l, x_h) = \begin{cases} 1 & \text{for } x_l \leq x \leq x_h \\ 0 & \text{otherwise} \end{cases} \quad (6.3)$$

then the constraint for the Aero discipline associated with each design variable is defined as

$$G^a(\bar{X}) = \prod_{i=1}^n g_i^a(x^{2i-1}, x_l, x_h) \cdot v_i^a \quad (6.4)$$

where v^a is the design variable weighting factor associated with each Aero subcomponent performance function and is defined as

$$\sum_{i=1}^n v_i^a = 1 \quad (6.5)$$

The maximum lift defined by the Aero function is written as

$$L(\bar{X}) = F^a(\bar{X}) \cdot G^a(\bar{X}) > L^o(\bar{X}) \quad (6.6)$$

where $F^a(\bar{X})$ is the Aero performance function.

Similarly, the EM discipline is derived in the same manner as the design variables that were determined from the Aero discipline perspective. The constraint associated with the EM discipline is defined as

$$G^r(\bar{X}) = \prod_{j=1}^m g_j^r(x^{2i}, x_l, x_h) \cdot v_j^r \quad (6.7)$$

and the EM constraint weighting factor is

$$\sum_{j=1}^m v_j^r = 1 \quad (6.8)$$

and the minimum function of the EM solution bounded by the Aero constraint is defined as

$$R(\bar{X}) = F^r(\bar{X}) \cdot \left\{ \frac{1}{G^r(\bar{X})} \right\} < R^o(\bar{X}) \quad (6.9)$$

where $F^r(\bar{X})$ is the EM performance function, and $R^o(\bar{X})$ is the initial arbitrary EM solution. The optimum performance function of the cross-discipline between the Aero and EM disciplines is defined by

$$O(\bar{X}) = w \cdot L(\bar{X}) + (1 - w) \cdot R(\bar{X}) \quad (6.10)$$

where w is the weighting factor associated with each discipline. The primary purpose of w is to emphasize the design objective. The weighting factor can also be used as a scaling factor.

The inter-disciplinary algorithm has shown promising results in achieving a robust design to provide flexibility in resolving the conflicts in game theory [84] among protocols on the design parameters that involve the coupled information between players. The MDO of this paper evolves two distinct disciplines that will derive an optimal solution in concurrent sequence. The concurrent subspace optimization approach [85] which is based on the concept of multilevel structural optimization and Multi-Level Optimization approaches in [86] seeks to minimize the discrepancy in the coupling equations while satisfying the design constraints.

6.1 MODELS CRITERIA IN AERODYNAMIC AND ELECTROMAGNETIC DISCIPLINES

The wing planform has to be determined at the design conceptual stage since the geometric shape is considered one of the key constraint parameters and is closely related to the EM discipline function. Conducting trade-off analyses between the return of backscattered field and the aerodynamic requirements will be most prudent in high-performance future air vehicle design. Recent study stated that an optimum wing planform would be a highly swept, and highly tapered arrowhead [87] where the sweep angle is dictated by cruising speed and airfoil technology. The geometric shape for a low-drag wing planform is a complex problem confronted by a range of factors, such as sweep angle, aspect ratio, control surface, flight envelope limits, etc.

Genetic Algorithms (GA) in MDO are commonly used for airfoil design and wing shape planform optimization. Examples include Multiobjective Genetic Algorithm

(MOGA) [88] in the design of a cascade airfoil, High-Fidelity MDO of aerostructural wing shape [89], MDO on aircraft wing planform based on Evolutionary Algorithm [80], Design Optimization of supersonic wings using Evolutionary Algorithm [90], Optimization of supersonic wings [91] using Evolutionary Algorithm, Subsonic wing planform design [92] using multidisciplinary optimization, and many others. Whereas in this paper MDO is used for design optimization of two distinctive (Aero & EM) disciplines. The inclusion of the EM discipline, or the computation of backscattered field return for high frequency applications, induces additional complexity in the context of MDO. The integration of inter-disciplinary controlled parameters, computation power, and convergence are issues of particular interest to MDO.

Data integration among disciplines in MDO is a difficult design process. An attempt to incorporate a narrow wing shape failed [25] due to design integration difficulties on aeroelastic problems and high structural weight. Another study of an automated MDO used to optimize aerodynamics and structural dynamics [93] described the necessity of modeling the inter-discipline effects to achieve realistic optimized wing planforms.

It is essential to develop a fundamental model as the basis for optimization in the context of MDO treating two distinctive disciplines concurrently. Introducing, yet another aspect of MDO approach through SMA illustrates the coupling effects among the Aero and EM disciplines. The primary objective of SMA is to attain an optimum performance function for maximum lift with minimal induced drag force due to lift, and minimum backscattered field return under the constraints of geometrical wing shape and structural weight. Computation or prediction of

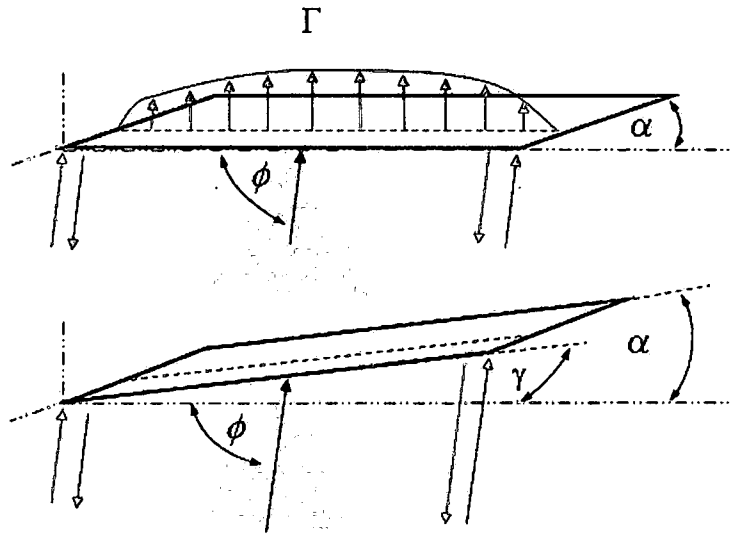


Figure 6.3: Modal of a zeroth (0^{th}) order mode wing planform

backscattered field return for X-band (8-12 GHz) is a laborious task due to the electrically large wing shape in term of wavelength, and is impractical under extreme circumstances. Therefore, a simplistic Aero & EM geometric shape modal, referred as Zeroth (0^{th}) Order mode shown in Figure 6.3 is used to demonstrate the SMA concept.

Computed data of the 0^{th} order modal mode of a thin rectangular and linearly tapered wing planform will be presented in the following section. The 0^{th} order modal mode is used to

- a) Prove the SMA concept by comparing the computed data with experimental values
- b) Define the desirable parameters/variables for an optimal solution among the multi-objective functions

- c) Augment MDO process with adaptability and "design-in " early in the conceptual stage
- d) Analyze the design variables randomness dynamic and improve computational convergency
- e) Demonstrate an empirical method for obtaining "best-case" scenario condition
- f) Investigate the potential application as a "Quick Look" tool for numerically complex problems deal with MDO

The next step would be to substitute the 0th order mode with an actual airfoil shape to "test" the validity of the "optimum" values in the context of MDO. The ability to understand the trade-offs and attain the ambitious objectives on the coupling effects among the Aero and EM disciplines will not only enhance the design objectives of future high-performance air vehicles, but also improve the implementation process results in a tightly integrated MDO.

6.2 COMPUTATIONAL DATA OF A RECTANGULAR WING PLANFORM

Aerodynamic performance is sensitive to wing planform geometry and must account for the structural strength constraints and environmentally controlled parameters, such as airspeed, altitude, and weight, among others. In this section, the effectiveness of the Stochastic Mutation Algorithm (SMA) deals with the Aero and EM disciplines concurrently within the same set of design variables and constraints will be assessed. The need to derive an optimal solution for each discipline concurrently will be of interest in the context of MDO. A rectangular wing shape shown in Figure 6.4 and Figure 6.5 is used to illustrate the objective in

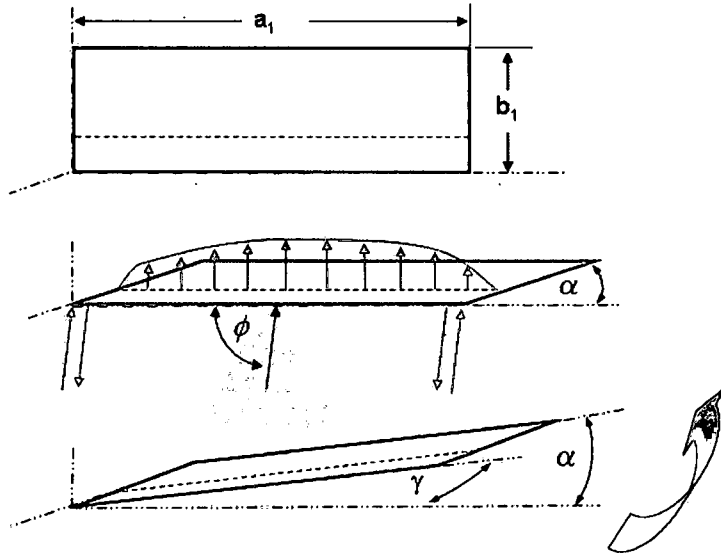


Figure 6.4: Low aspect ratio of a finite thin rectangular wing

deriving a maximum lift while obtaining a minimum backscattered field of the same wing planform where the physical wing mass and wing surface area (constraints) remain the constant. As in this case, the lift increases as the rectangular wing shape varies as shown in Figure 6.4 to the shape shown in Figure 6.5 by altering the wing aspect ratio as shown in Equation (5.18) while the wing surface area and weight are constant.

Angle γ is the the orientation angle with respect to the wing in the azimuth plane. The wingspan a_{rf} in reference to the observation angle ϕ in EM perspective is defined as

$$a_{rf} = a_1 \cos(\gamma) \quad (6.11)$$

and the chord b_{rf} is

$$b_{rf} = b_1 \cos(\alpha) \quad (6.12)$$

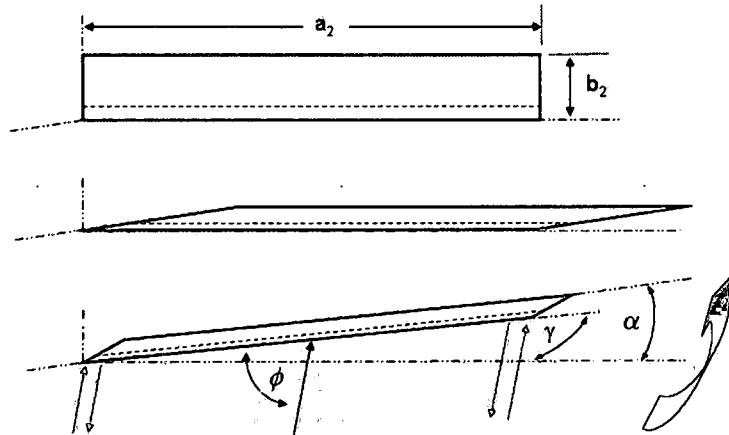


Figure 6.5: High aspect ratio of a finite thin rectangular wing

while the wing aspect ratio of Figure 6.4 and 6.5 are different, the wing surface of the two wingspans are the same

$$a_1 b_1 = a_2 b_2 \quad (6.13)$$

Other factors affecting lift force are shown in Table 6.1. A subset of environmentally controlled variables are used to demonstrate the SMA concept in the MDO scheme. Only physical factors such as airspeed, dynamic pressure, and weight are considered since the EM discipline is directly related to the wing shape, surface area, and aspect view angle. The lift slope curve for a finite, 3-D wing is derived from the airfoil having an infinite section of wingspan as shown in Figure 6.6. The 3-D finite wing lift slope is considerably less than the 2-D infinite wingspan [94]. Since the infinite wingspan does not include the effect of wing aspect ratio, thus a lift slope curve containing the wing aspect ratio is defined [2] as

$$C_{\ell}^{AR} = \frac{C_{\ell}}{1 + \frac{C_{\ell}}{\pi(AR)}} \quad (6.14)$$

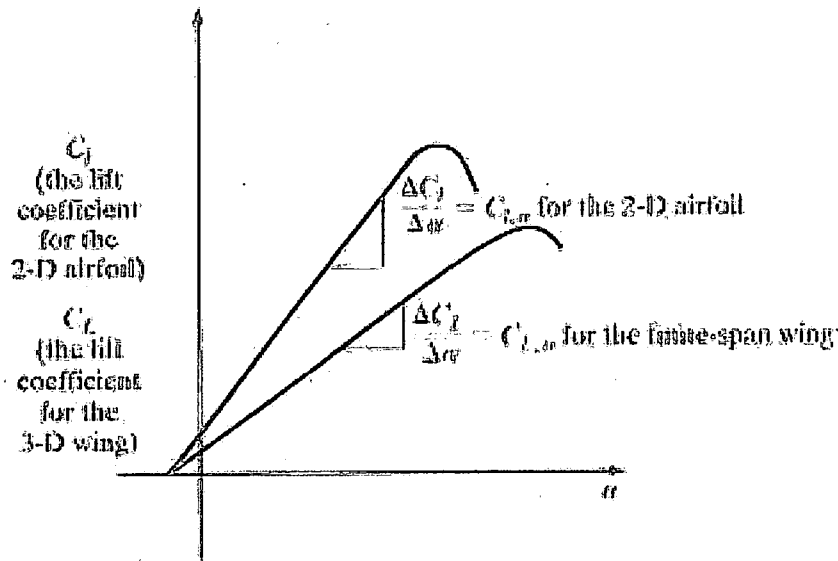


Figure 6.6: $C_l - \alpha$ curve of infinite and finite wing planform [2]

Hence, the lower the aspect ratio, the more induced drag a wing will produce and the lower the lift curve slope becomes. Refer to Figure 6.6 where the straight line of $C_l - \alpha$ can be represented by

$$C_l = C_l^\alpha \alpha + C_l^0 \quad (6.15)$$

where C_l^α is the slope of the curve and C_l^0 is the y-axis intercept point. According to the infinite wing span (ideal aerodynamics) of the Thin Airfoil Theory [95], the y-intercept C_l^0 is 0 and the slope of the lift curve C_l^α is equal to 2π .

As indicated in Equation (6.14), the physical shape of the wing planform contributes directly to the return of electromagnetic backscattered field. Table 6.1 shows the control design parameters of a rectangular wing shape bounded by the environment constraints, such as size, surface area, physical weight, wing loading weight, wing planform, wing aspect ratio, and angle of attack. The airspeed and

altitude are factors that can be referred to as application specific for spacecraft design. Since the primary purpose of this research focuses on the coupling effect among the Aero and EM disciplines, this paper examines the impact in the context of multi-disciplinary analysis. Therefore, super-sonic and hyper-sonic discussion is beyond the scope of this research. The normalized weight vector of wing loading due to angle of attack α is defined as

$$W_{Norm} = \frac{W_{wing}}{\cos(\alpha)} \quad (6.16)$$

Note that the amount of lift force generated by the rectangular wing is directly related to the angle of attack, a larger value of α produces a higher lift force and larger induced drag force as it increases the frontal area. However, excessively large angles of attack will cause the aircraft to stall due to the disruption of airflow, which causes loss of lift. The amount of lift or drag (conversely) are influenced by the airfoil wing profile [96], viscosity of air [97], and compressibility effects [98]. The stall speed is affected by many factors, such as weight, wing loading, angle of attack, and altitude, and is given as

$$V_s = \sqrt{\frac{2L_{wing}}{C_l S \rho_\infty}} \quad (6.17)$$

where L_{wing} is the lift force or the normalized weight vector of the wing loading and C_l is the lift coefficient defined by the stall angle of attack. Hence, the stall speed is a function of the physical size of the airfoil wing profile and the viscosity of the air. For constant airspeed (unaccelerated) flight, stall condition is related to airspeed below which the aircraft will not continue to fly, a design criterion relevant to aerodynamic performance but which has no bearing on the EM discipline since EM backscattered field is not a function of velocity, or viscosity of air, but is a function

of physical size in term of electrical wavelength and perspective observation angle in the azimuth plane. The SMA process will mutate both distinctive disciplines concurrently to attain a best outcome for any given arbitrary state.

Since the primary purpose of SMA is to illustrate the concept of coupling two distinctive Aero and electromagnetic (EM) disciplines, the number of design variables for a rectangular wing planform is limited to those controlled parameters relevant to both Aero and EM functions and as shown in Table 6.1. The SMA optimization process will first obtain an initial optimal lift force greater than the wing loading weight plus the lift force margin (150N to 400N) and a drag force less than 300N while attaining an optimum EM solution during the iteration cycle. The lift force is first computed with respect to the Aero discipline and evaluated with the condition $L_i(\bar{X}) \geq W_{norm} + L_{mgn}$ and $D_i(\bar{X}) \leq 300N$. Once a lift force meets the Aero criteria, this lift force data is captured as the current optimum. SMA then minimizes EM function for the wing geometry with respect to the Aero discipline while the physical wing is being oriented in the azimuth plane to attain a minimum backscattered field return $R_i(\bar{X}) \leq R_{min}(\bar{X})$. The Aero discipline cycle completes if the current iteration yields a maximum $L_i(\bar{X})$ and a minimum $R_i(\bar{X})$. Then SMA optimization with respect to EM discipline will first compute a minimum $R_i(\bar{X}) \leq R_{min}(\bar{X})$, and then seek to attain a maximum $L_i(\bar{X})$ until an optimum solution converges, and the design variable vector, (\bar{X}) is now known as the current optimal solution to both disciplines.

The lift force L_i computed by each trial of a finite, thin rectangular wing shown in Figure 6.4 is shown in Figure 6.7. Each trial takes two cycles to process; the first cycle computes a maximum lift force L_i (Aero discipline), and the second cycle

Table 6.1: Control Parameters of a Rectangular Wing Optimization: RectProbSet1

Variable	Value	Description
a_{ar}	2	Wing span (m)
b_{ar}	1	Chord (m)
AR_i	2 to 20	Wing Aspect Ratio
S_{wing}	2	Wing Surface Area (m^2)
α_i	0 to 15	Angle of Attack (Deg.)
θ	0 to 180	Spanwise Distribution Angle (Deg.)
Γ	$0 < \Gamma(\theta) < 1$	Spanwise Distribution Fourier Sine Series
C_ℓ^o	0.1252	Intercept lift coefficient @ $\alpha = 0^\circ$
C_ℓ^α	2π	Thin Foil Lift Slope Curve Coefficient
V_∞	160	Airspeed (km/h)
Alt	5000	Altitude (m)
q_∞	0.736	Air Density (kg/cu m)
P_∞	54.042	Air Pressure (kpa)
T_∞	-17	Air Temperature (Deg. C)
W_{wing}	1600	Physical Weight (N)
W_{norm}	$\frac{W_{wing}}{\cos(\alpha)}$	Normalized Weight (N)
L_{mgn}	150 to 400	Design Lift Margin (N)
L_i^{opt}	$> (W_{norm} + L_{mgn})$	Desired Lift Force (N)
D_i	< 300	Maximum Drag Force (N)
γ_i	0 to 30	Aspect View Angle WRT EM discipline (Deg.)
a_{rf}	$a_{ar}\cos(\gamma)$	Wing span WRT EM discipline (m)
b_{rf}	$b_{ar}\cos(\alpha)$	Chord WRT EM discipline (m)
E^{inc}	1	Incident E-field ($\frac{v}{m}$)
ϕ'	90	Incident E-field Angle (Deg.)
ϕ	0 to 90	Observation Angle Monostatic (Deg.)
f_o	9.0	Operating Frequency (GHz)
r_o	500	Observation Distance in RF wavelength (λ)
R_i^{opt}	< 0.4	Desired Backscattered Return Scalar

computes a minimum backscattered field return R_i of the wing planform (EM discipline). Classical aerodynamic shape optimization [99] and the adjoint method for optimal shape design of an airfoil [100] accelerates the numerical solution in analysis of multidisciplinary design where each solution converges simultaneously. The current maximum lift force and its corresponding normalized wing loading weight where the Aero solution converges is shown in Figure 6.8. The SMA processor mutates until it obtains a lift force L_i greater than the previous one, then randomizes and the mutate processor repeats. In order for those control parameters shown in Table 6.1 to be random in nature, the random seed was generated using the computer clock since the analysis of computer experiments typically lack random error but are statistically suitable for deterministic problems through the use of interpolation method or kriging [101].

The corresponding induced drag force D_i of Figure 6.8 is shown in Figure 6.9. The induced drag force is the result of the downwash effect as shown in Figure 5.4, and is a function of C_ℓ .

The lift force vector, F , shown in Figure 5.4 will vary with respect to the wing aspect ratio AR , and angle of attack α for a given constant airspeed V_∞ and altitude. Figure 6.10 is the EM backscattered field return and Figure 6.11 is the same backscattered field using a 10° median filter to smooth out the notches. It represents the minimum return of backscattered field that corresponded to each maximum L_i at the i^{th} trial. Hence, it is referred to as an optimal solution with respect to the Aero discipline in which a minimum EM solution is also obtained after a maximum Aero lift force has been first attained. Refer to Figure 6.8. Each marker indicates an optimal lift force has been attained and its backscattered field

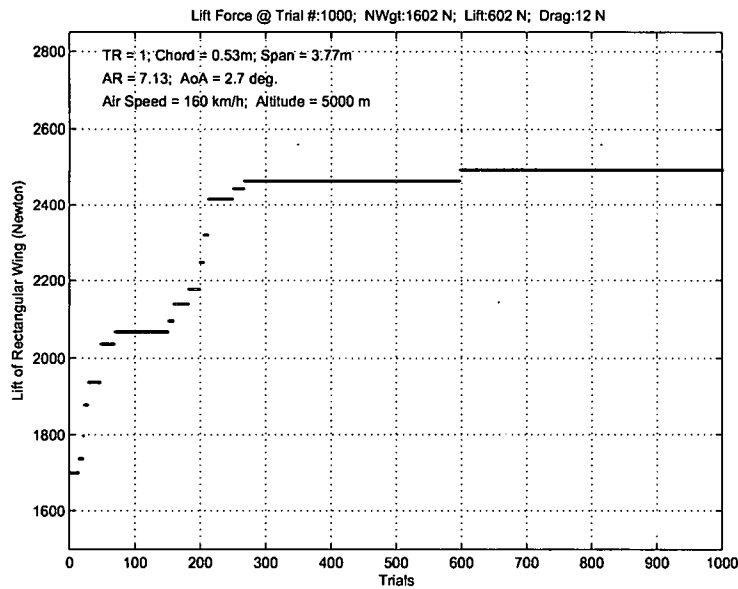


Figure 6.7: Lift force (L_i) of a rectangular wing; RectProbSet1

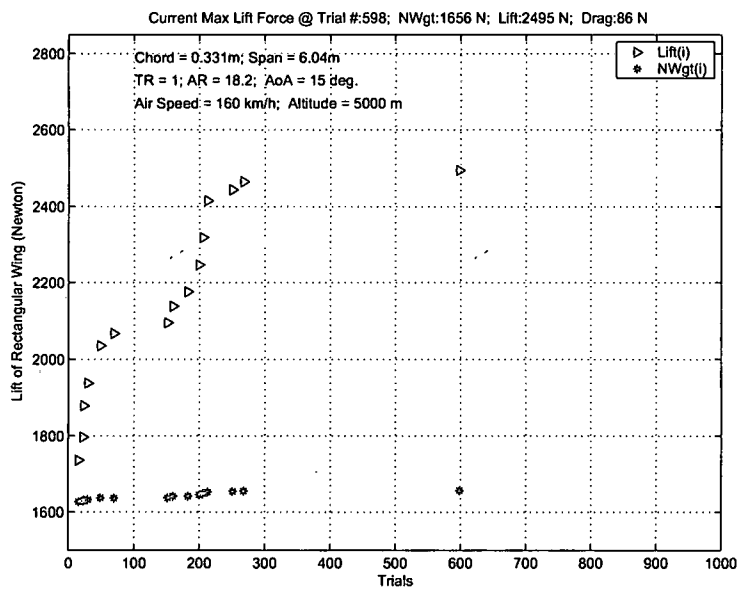


Figure 6.8: Current Max L_i and W_{Norm} of a rectangular wing; RectProbSet1

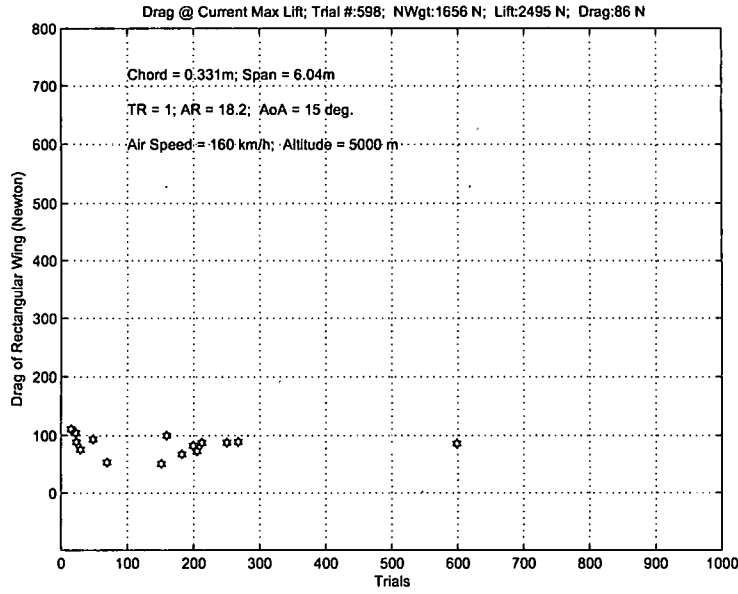


Figure 6.9: Current Drag force D_i of a rectangular wing; RectProbSet1

return is shown in Figure 6.12. Hence multiple optimal lift force L_i had been attained but only a few will meet the EM discipline criteria and produce a minimum EM backscattered field simultaneously. Note that the sum of coefficient factor in Figure 6.12 of the current $R_{i+1} = 1.165$ is greater than the previous $R_i = 0.734$. This is the condition where a minimal EM solution is not achievable during the current Trial No. 598 and fails with respect to the Aero discipline. Figure 6.11 represents the fall-back optimization solution at Trial No. 22 with respect to the Aero discipline where both conditions $L_{i+1} > L_i$ and $R_{i+1} < R_i$ are met.

The magnitude of the EM backscattered field is influenced by the physical shape, size, aspect view angle in azimuth plane, and the orientation angle with respect to the observation point. However, the actual physical size of the wing planform and its surface area remained the same in an Aero discipline perspective. Figure 6.13

depicts the relative backscattered field return shown associated with the orientation angle γ in the azimuth plane. The backscattered field shown in Trial No. 598 should be less than the value previously obtained ($R_{i+1} < R_i$) with respect to the EM discipline by alternating the aspect angle in the azimuth plane. Figure 6.14 takes on the value of Figure 6.13 as its current minimum EM solution in Trial No. 598.

Figure 6.15 is the same waveform with a 10° median filter. This captured waveform occurs if and only if a minimal EM solution was also attained while a maximal lift force had been obtained at the current Trial i . Hence Figure 6.15 is the optimized solution with respect to the EM discipline in which both the EM and the Aero disciplines had reached the design threshold respectively, that is, a minimal EM backscattered field return and a maximal Aero lift force.

Despite the fact that both the Aero and the EM are two distinctive disciplines, they are coupled to attain optimization for a given arbitrary state. The optimization process may take thousands of random trials, and sometime may not produce an optimization as desired. Thus, trade off between computing power, cost, and design requirements can be a challenging issue to address, possibly with another optimization method.

Each design variable is independent of the others and random by nature, where multiple sets of optimal solutions are possible without deterministic conclusion [102]. Refer to data on the lift force L_i and EM backscattered field R_i in Figures 6.11 (WRT Aero discipline) and Figure 6.15 (WRT EM discipline). This is a typical case where a trade off between Aero vs. EM discipline takes place. The quick assessment provides valuable insight for application during the preliminary

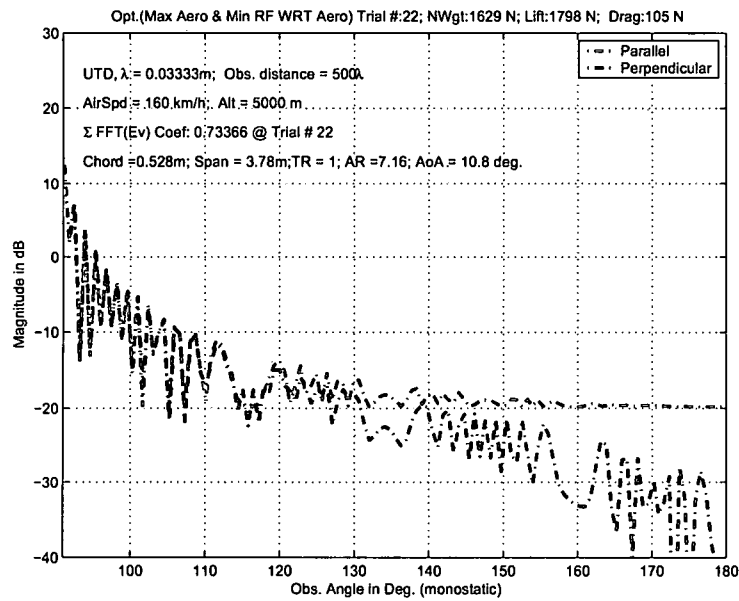


Figure 6.10: Optimal: $\text{Max}(L_i)$ & $\text{Min}(R_i)$ WRT Aero Discipline of a rectangular wing; RectProbSet1

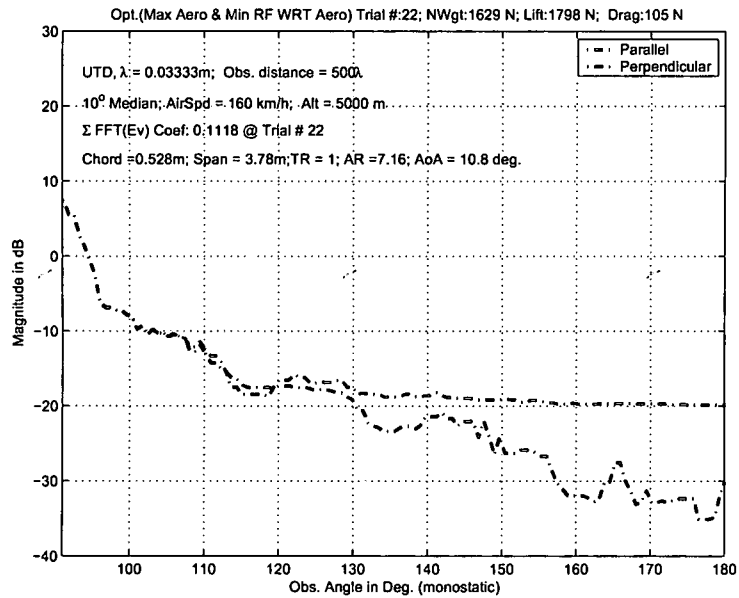


Figure 6.11: Optimal: $\text{Max}(L_i)$ & $\text{Min}(R_i)$ w/10° median WRT Aero Discipline of a rectangular wing; RectProbSet1

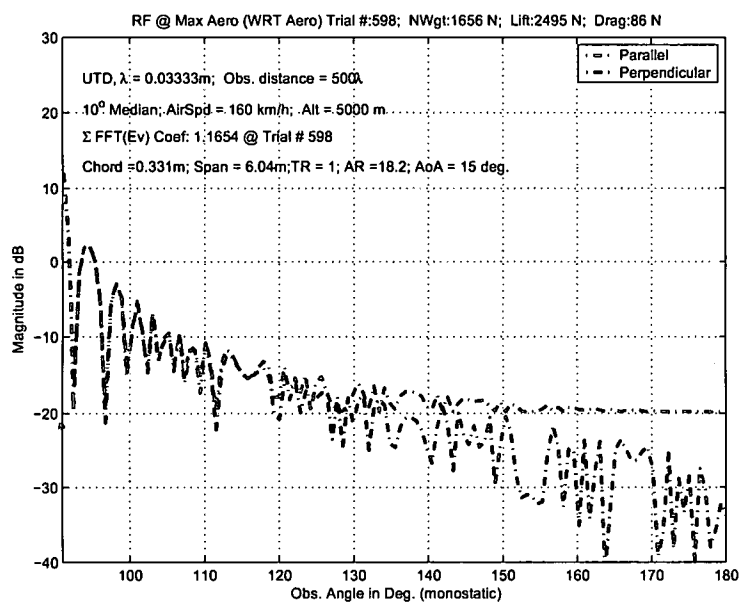


Figure 6.12: Current R_i @ $\text{Max}(L_i)$ WRT Aero Discipline of a rectangular wing; RectProbSet1

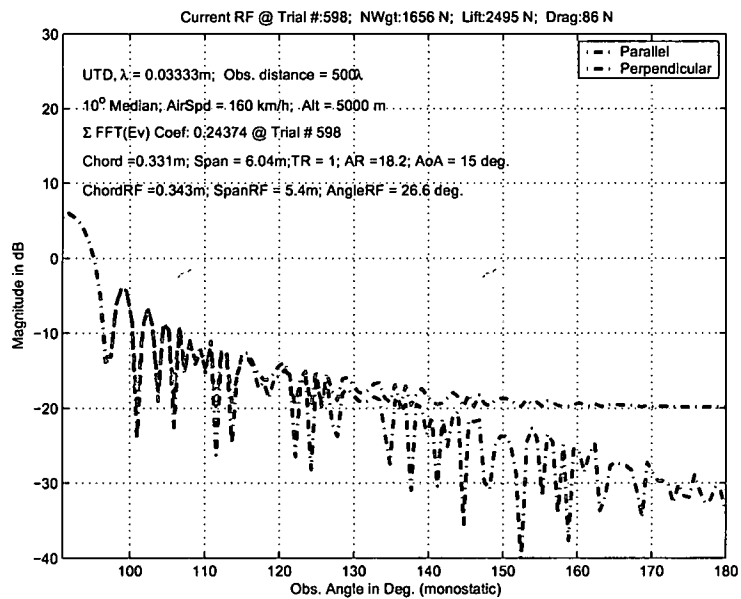


Figure 6.13: Current $\text{Min}(R_i)$ @ $\text{Max}(L_i)$ WRT EM Discipline of a rectangular wing; RectProbSet1

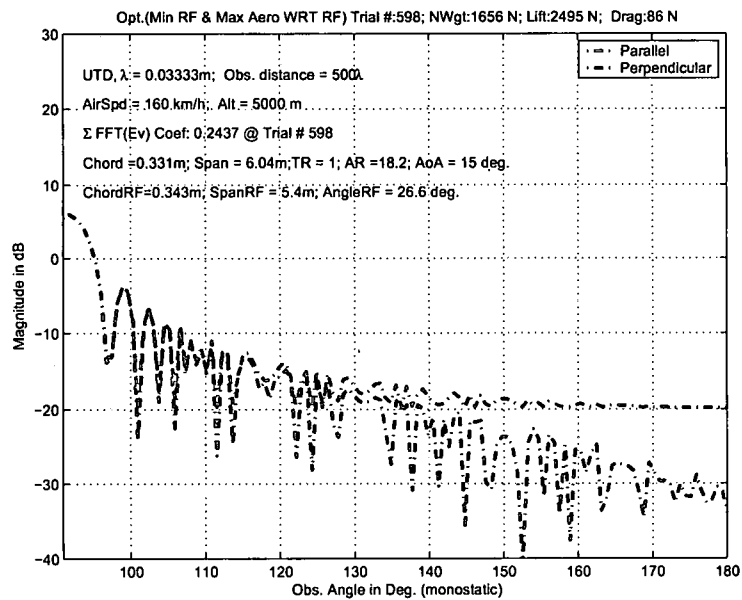


Figure 6.14: Optimal: $\text{Min}(R_i)$ & $\text{Max}(L_i)$ WRT EM Discipline of a rectangular wing; PProbSet1

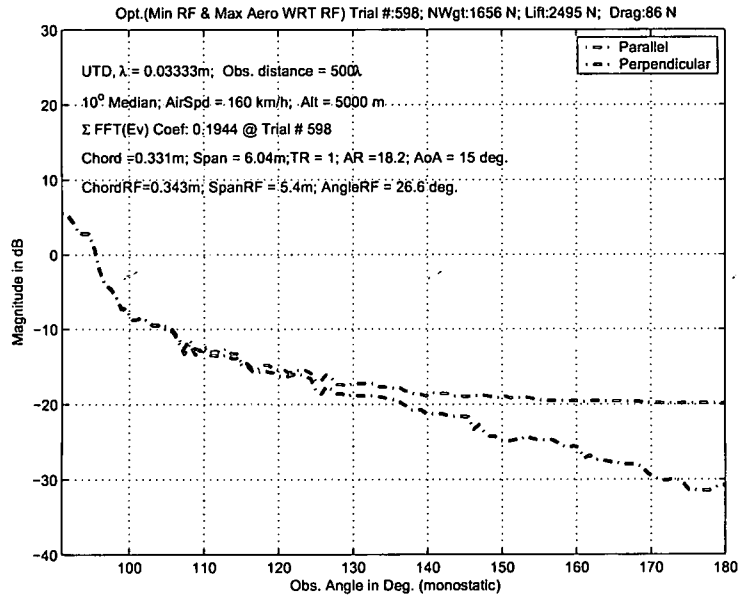


Figure 6.15: Optimal: $\text{Min}(R_i)$ w/ 10° median & $\text{Max}(L_i)$ WRT EM Discipline of a rectangular wing; RectProbSet1

design stage where MDO provides critical data for quick assessment. Data obtained from various runs of RectProbSet1 were tabulated and shown in Table 6.2.

It should be noted that every "optimal" lift force L_i shown in Figure 6.8 does not necessarily yield an optimal solution to satisfy both disciplines. However, each trial will converge to its last optimum lift force with respect to the Aero discipline or minimal backscattered field return with respect to the EM discipline. Even though each trial converges, it converges to the last best value and does not necessarily reach an optimization in the coupling context.

Simulated data shown in Table 6.2 indicates that a greater wing aspect ratio and larger angle of attack produces greater lift force. In particular, high wing aspect ratio generates lower induced drag force. The tabulated output data provides a quick assessment on optimization requirements. Any changes made in the control environment will greatly affect the Aero discipline, such as airspeed and altitude. Refer to Run #1, Trial No. 49 vs. 194, even though the wing aspect ratio (3.45 vs. 11.0), is 3.18:1, the backscattered field returns are fairly close (0.247 vs. 0.255) but the lift forces difference was 499N (1941N vs. 2440N). In Run #6, Trial No. 46 and 301, since the drag force of both disciplines meet the criteria, a trade-off between the lift force (1891N vs 2454N) and the backscattered field return (0.117 vs. 0.262) transpired. The disparity in benefit trade-off is approximately 4 to 1; 124% increases in backscattered field return for 30% gain in lift force (L_i). Another unique situation is in Run #10, a gain of 741N in lift force while the backscattered field return remains the same, a unique design trade-off scenario.

Greater lift force can be attained by increasing the airspeed, decreasing the altitude, or enlarging the wing surface area. Since the wing surface shown in

Table 6.2: Computed MDO Data of Table 6.1 Controlled Parameters

RectProbSet1	Trial i^{th}	AR	α°	L_i (N)	D_i (N)	γ°	R_i
Run #1	49	3.45	12.7	1941	245	0	0.247 [‡]
Run #1	194	11.0	14.9	2440	130	27.1	0.255 [†]
Run #2	617	14.5	14.9	2460	103	0	0.230 [‡]
Run #2	617	14.5	14.9	2460	103	4.06	0.242 [†]
Run #3	12	21.3	9.99	1742	37	0	0.114 [‡]
Run #3	105	10.1	14.8	2415	138	20.9	0.283 [†]
Run #4	14	8.64	10.3	1749	83	0	0.225 [‡]
Run #4	664	18.6	14.9	2488	84	25.8	0.145 [†]
Run #5	60	21.1	10.5	1814	40	0	0.169 [‡]
Run #5	179	17.5	14.8	2471	87	25.2	0.239 [†]
Run #6	46	21.4	11.0	1891	43	0	0.117 [‡]
Run #6	301	11.9	15.0	2454	122	29.0	0.262 [†]
Run #7	21	6.68	10.4	1733	104	0	0.084 [‡]
Run #7	321	15.9	14.7	2446	93	9.65	0.291 [†]
Run #8	31	21.9	9.69	1698	34	0	0.213 [‡]
Run #8	70	9.48	11.7	1953	95	14.7	0.303 [†]
Run #9	22	21.9	9.42	1656	32	0	0.221 [‡]
Run #9	120	4.02	14.9	2243	282	19.6	0.204 [†]
Run #10	19	14.2	9.66	1708	50	0	0.270 [‡]
Run #10	156	14.7	14.8	2449	100	9.56	0.270 [†]

‡ Max L_i & Min R_i with respect to Aero discipline

† Min R_i & Max L_i with respect to EM discipline

Equation (6.13) remains constant for this analysis, the airspeed in Table 6.3 has increased to 200 km/h. The lift force with this increase airspeed is shown in Figure 6.16 ($L_i \propto V_\infty^2$). The optimal lift force and its corresponding normalized wing loading weight is shown in Figure 6.17. The induced drag force vector due to lift is shown in 6.18. No significant increase in drag force is noticed.

The minimum EM backscattered field return with respect to the Aero discipline is shown in Figure 6.19 with $R_{335} = 1.294$ which was greater than the $R_{196} = 0.613$. Hence, Figure 6.20 is the minimum EM solution with respect to the Aero discipline. Figure 6.21 shows the backscattered field using a 10° median filter. Since Trial No. 196 derived a minimum R_{196} and maximum L_{196} , it is referred to as an optimal solution and represents the optimization solution with respect to the Aero discipline.

The current minimum R_i corresponds to every optimal L_i and are shown in Figures 6.22 and 6.17, respectively. Since $R_{843} > R_{335}$, the optimum solution with respect to the EM discipline is achieved at Trial No. 335 and its backscattered field is shown in Figure 6.23 and the 10° median waveform is shown in Figure 6.24.

Table 6.4 contains simulated data for $V_\infty = 200$ km/h, with the remaining environmental control variables unchanged. As airspeed increased from 160 km/h to 200 km/h, it produces a lift force over 3700 N as shown Figure 6.17. Most of the data shown in Table 6.4 exceeds the requirement shown in Table 6.3 for the same wing surface area, weight, and altitude. However, the lift force shown on Run #8 is much lower than the rest at Trial #29. In other words, not all trials will exceed every single time, but the SMA process mutates randomly to attain an optimal value in reference to its current state, in relative term. It is interesting to note that higher lift force and lower backscattered field were recorded with respect to the EM

Table 6.3: Control Parameters of a Rectangular Wing Optimization: RectProbSet2

Variable	Value	Description
a_{ar}	2	Wing span (m)
b_{ar}	1	Chord (m)
AR_i	2 to 20	Wing Aspect Ratio
S_{wing}	2	Wing Surface Area (m^2)
α_i	0 to 15	Angle of Attack (Deg.)
θ	0 to 180	Spanwise Distribution Angle (Deg.)
Γ	$0 < \Gamma(\theta) < 1$	Spanwise Distribution Fourier Sine Series
C_ℓ^o	0.1252	Intercept lift coefficient @ $\alpha = 0^\circ$
C_ℓ^α	2π	Thin Foil Lift Slope Curve Coefficient
V_∞	200	Airspeed (km/h)
Alt	5000	Altitude (m)
q_∞	0.736	Air Density (kg/cu m)
P_∞	54.042	Air Pressure (kpa)
T_∞	-17	Air Temperature (Deg. C)
W_{wing}	1600	Physical Weight (N)
W_{norm}	$\frac{W_{wing}}{\cos(\alpha)}$	Normalized Weight (N)
L_{mgn}	150 to 400	Design Lift Margin (N)
L_i^{opt}	$> (W_{norm} + L_{mgn})$	Desired Lift Force (N)
D_i	< 300	Maximum Drag Force (N)
γ_i	0 to 30	Aspect View Angle WRT EM discipline (Deg.)
a_{rf}	$a_{ar}\cos(\gamma)$	Wing span WRT EM discipline (m)
b_{rf}	$b_{ar}\cos(\alpha)$	Chord WRT EM discipline (m)
E^{inc}	1	Incident E-field ($\frac{v}{m}$)
ϕ'	90	Incident E-field Angle (Deg.)
ϕ	0 to 90	Observation Angle Monostatic (Deg.)
f_o	9.0	Operating Frequency (GHz)
r_o	500	Observation Distance in RF wavelength (λ)
R_i^{opt}	< 0.4	Desired Backscattered Return Scalar

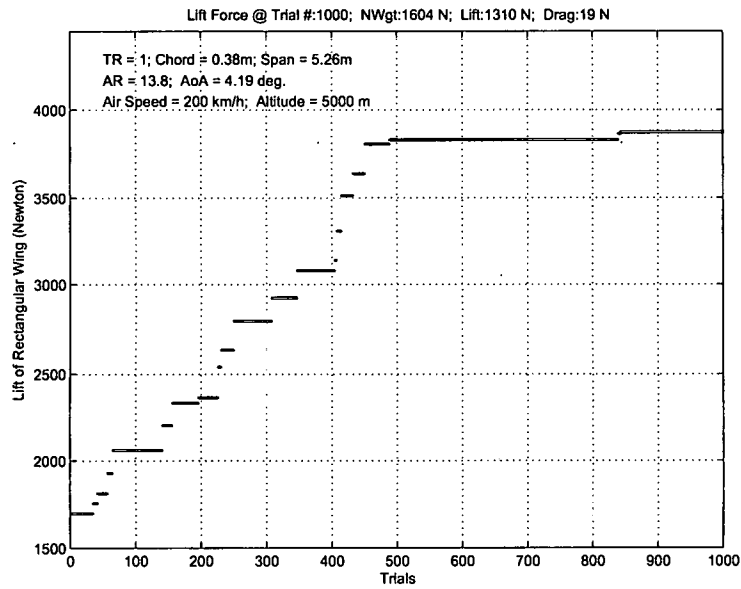


Figure 6.16: Lift force (L_i) of a rectangular wing; RectProbSet2

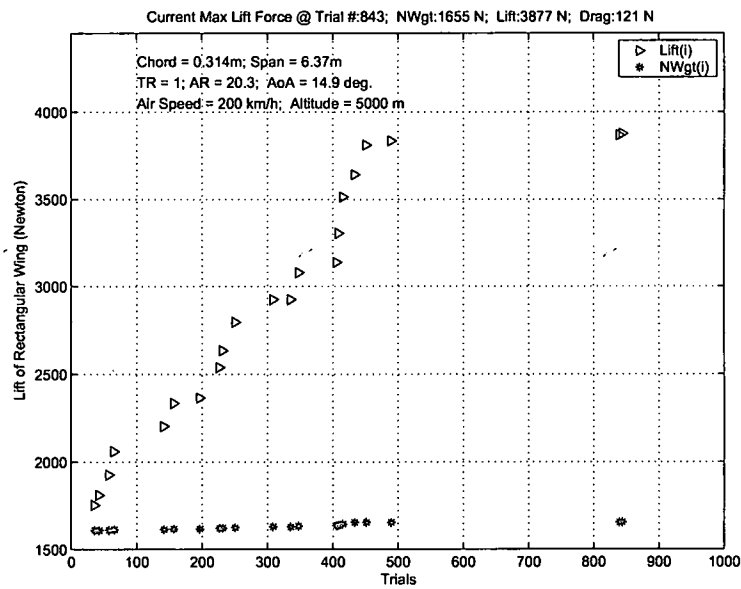


Figure 6.17: Current Max L_i and W_{Norm} of a rectangular wing; RectProbSet2

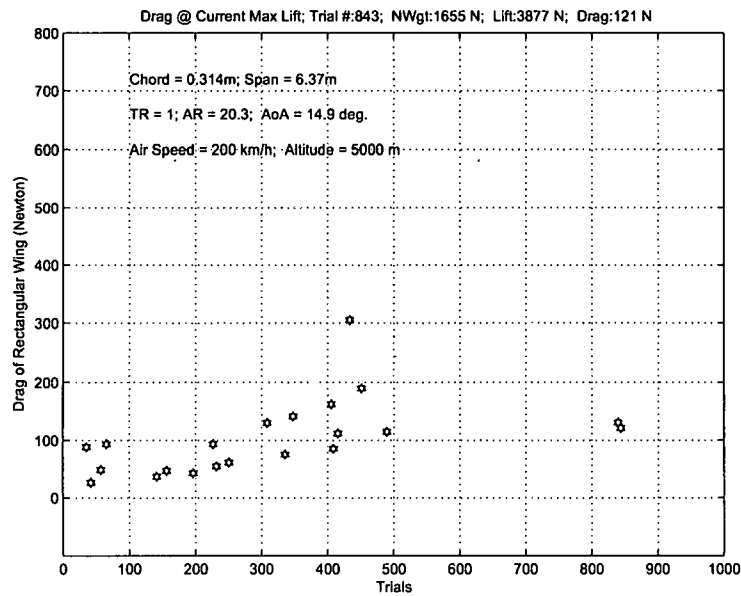


Figure 6.18: Current Drag force D_i of a rectangular wing; RectProbSet2

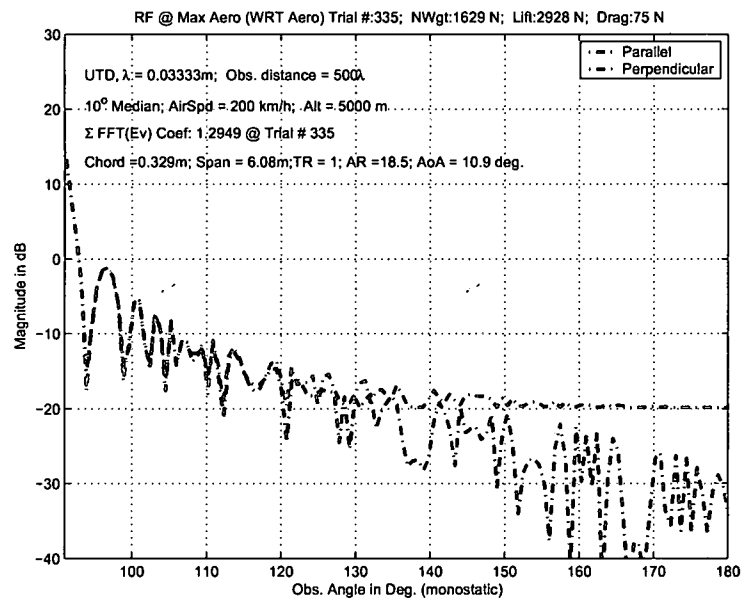


Figure 6.19: Current R_i @ $\text{Max}(L_i)$ WRT Aero Discipline of a rectangular wing; RectProbSet2

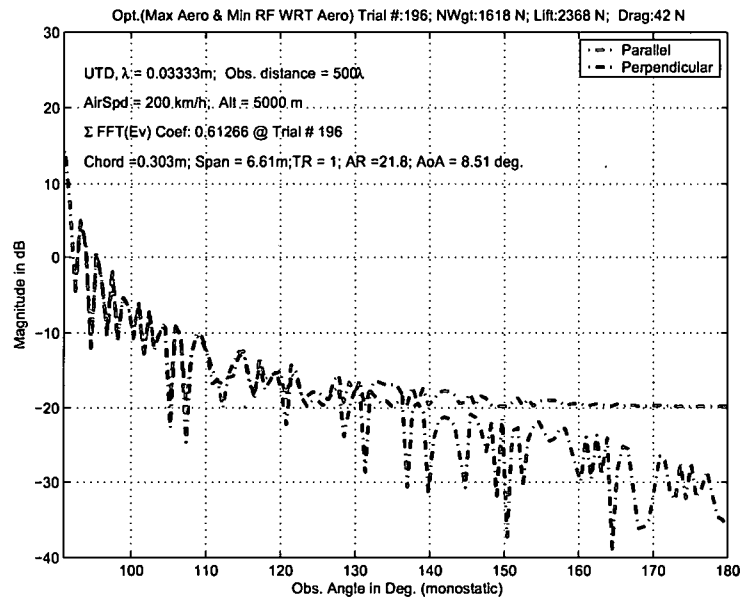


Figure 6.20: Optimal: $\text{Max}(L_i)$ & $\text{Min}(R_i)$ WRT Aero Discipline of a rectangular wing; RectProbSet2

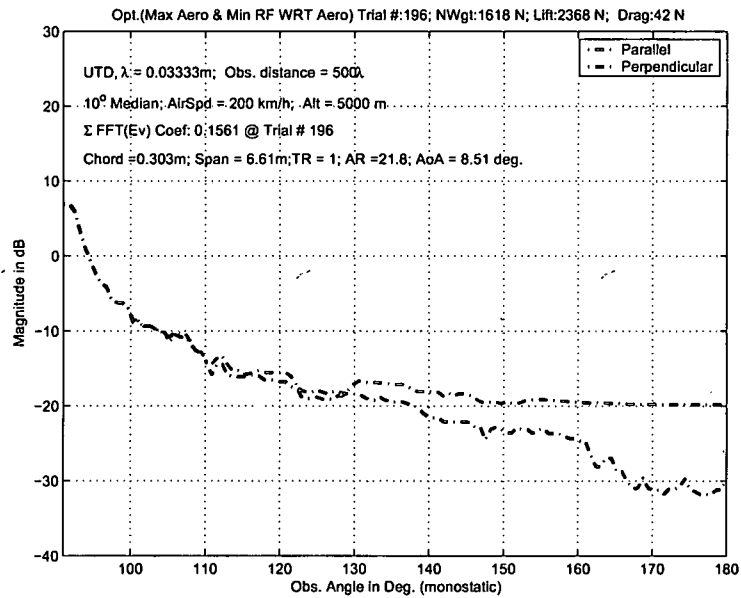


Figure 6.21: Optimal: $\text{Max}(L_i)$ & $\text{Min}(R_i)$ w/10° median WRT Aero Discipline of a rectangular wing; RectProbSet2

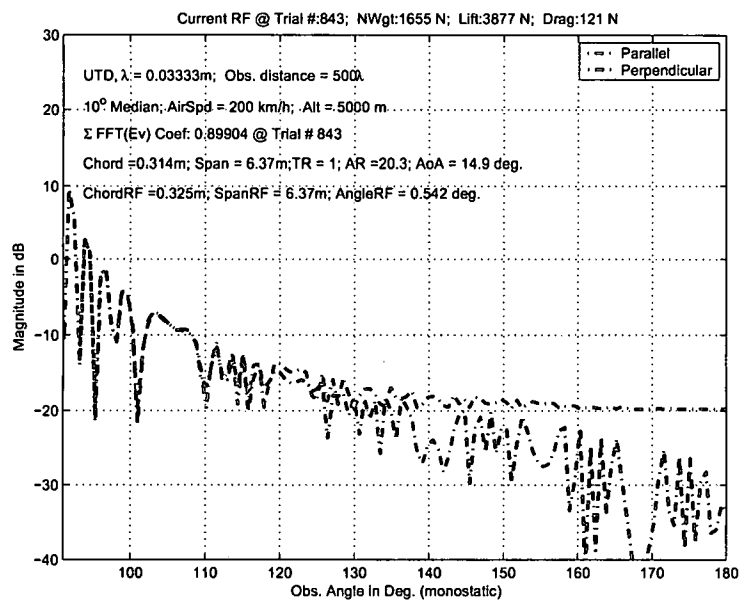


Figure 6.22: Current $\text{Min}(R_i) @ \text{Max}(L_i)$ WRT EM Discipline of a rectangular wing; RectProbSet2

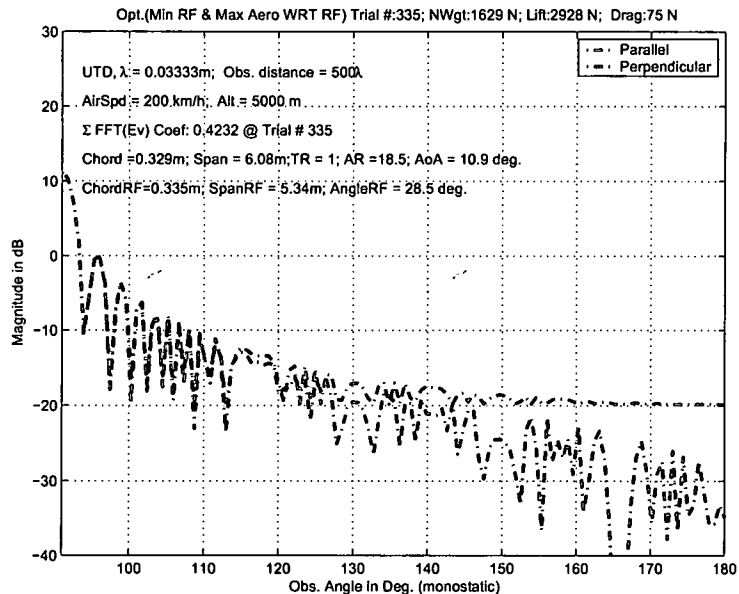


Figure 6.23: Optimal: $\text{Min}(R_i) \& \text{Max}(L_i)$ WRT EM Discipline of a rectangular wing; PProbSet2

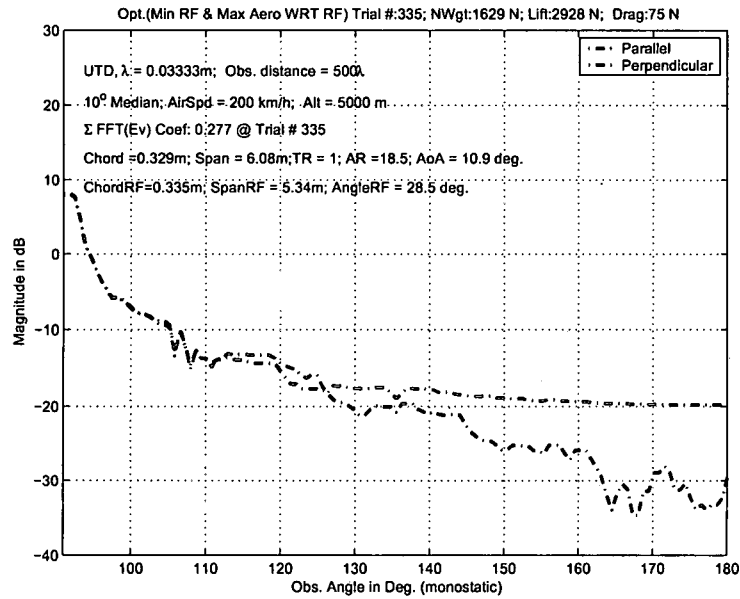


Figure 6.24: Optimal: $\text{Min}(R_i)$ w/ 10° median & $\text{Max}(L_i)$ WRT EM Discipline of a rectangular wing; RectProbSet2

discipline with the wing being oriented by γ in the azimuth plane. Optimization with respect to the EM discipline does not yield the desired solution for low wing aspect ratio $AR = 4.02$ shown in Run #2, since a low aspect ratio wing resembles a rectangular shape instead of a narrow strip. Note that in Run #3 both disciplines have similar wing aspect ratio (8.85 vs. 8.23) and angle of attack (12.8° vs. 14.7°) but the lift force obtained from the EM discipline is increased by more than 12% (3701 N vs. 3290 N) and the EM backscattered field is 19% (0.242 vs. 0.288) lower than the values attained by the Aero discipline. The trade off for gaining the higher lift force and lower backscattered field return is the increase of induced drag force by approximately 35% (249 N vs. 184 N).

Table 6.4: Computed MDO Data of Table 6.3 Controlled Parameters

RectProbSet2	Trial i^{th}	AR	α°	L_i (N)	D_i (N)	γ°	R_i
Run #1	77	15.6	6.30	1822	34	0	0.326 [†]
Run #1	311	14.9	10.7	2876	88	6.40	0.154 [‡]
Run #2	95	4.02	10.1	2558	234	0	0.272 [†]
Run #2	95	4.02	10.1	2558	234	23.6	0.310 [†]
Run #3	131	8.85	12.8	3290	184	0	0.288 [‡]
Run #3	229	8.23	14.7	3701	249	9.37	0.242 [†]
Run #4	196	21.8	8.51	2368	42	0	0.156 [‡]
Run #4	335	18.5	10.9	2928	75	28.5	0.277 [†]
Run #5	78	14.2	6.83	1948	42	0	0.287 [‡]
Run #5	142	4.24	9.53	2443	203	24.9	0.236 [†]
Run #6	26	16.1	6.48	1869	34	0	0.394 [‡]
Run #6	158	8.32	11.6	2399	104	11.8	0.236 [†]
Run #7	128	7.98	6.77	1906	68	0	0.259 [‡]
Run #7	250	8.64	10.3	2733	130	6.50	0.173 [†]
Run #8	29	3.06	6.13	1674	131	0	0.142 [‡]
Run #8	155	16.6	10.5	2830	77	16.5	0.237 [†]
Run #9	136	7.19	6.65	1871	72	0	0.116 [‡]
Run #9	483	18.8	14.5	3790	123	28.5	0.206 [†]
Run #10	128	7.98	6.77	1906	68	0	0.259 [‡]
Run #10	250	8.64	10.3	2733	130	6.5	0.173 [†]

‡ Max L_i & Min R_i with respect to Aero discipline

† Min R_i & Max L_i with respect to EM discipline

The environmental control variables play an important role in Aerodynamics performance, leading to lower dynamic pressure at high altitude, which results in a decrease in lift force. To maintain the same lift force at high altitude, an increase in airspeed is necessary to produce the required lift. An environment parameters RectProbSet3 is shown in Table 6.5 and the simulated data illustrate the compensation effect between high altitude and airspeed.

The range of lift force L_i and the normalized wing loading weight W_{Norm} shown in Figure 6.25 is similar to those data of Table 6.2 since the increase in airspeed is compensated by the atmospheric effect of higher altitude. Hence, providing a complementary effect resulted in a net lift margin similar to the value prescribed by Table 6.2 control parameters. Figure 6.26 depicts a moderate induced drag force except one close to 300N. This value is about three times the average value and is due to the low wing aspect ratio. Figure 6.27 is the snap shot of the lift coefficient C_ℓ vs. the induced drag coefficient C_d . The high drag coefficient shown corresponds to $C_\ell = 1.5$ and it is interesting to note that the same lift coefficient can also produce a much smaller induced drag coefficient (0.04 vs. 2.3), an improvement factor of 57. Clearly, the ability to explore the effects due to the composite control parameters provides a benefit to traditional aircraft design. The converged lift force, L_i , for each trial is shown in Figure 6.28. It reached its optimal peak very quickly, by Trial No. 278 which would be in most cases for small-scale control parameters. Figure 6.29 indicated that a minimum EM backscattered field was obtained with each optimal L_{276} and Figure 6.30 is minimum EM solution at L_{188} with respect to the Aero discipline, and the 10° median filter waveform is shown in Figure 6.31. On the EM discipline side, Figure 6.32 depicts a different backscattered field return

Table 6.5: Control Parameters of a Rectangular Wing Optimization: RectProbSet3

Variable	Value	Description
a_{ar}	2	Wing span (m)
b_{ar}	1	Chord (m)
AR_i	2 to 20	Wing Aspect Ratio
S_{wing}	2	Wing Surface Area (m^2)
α_i	0 to 15	Angle of Attack (Deg.)
θ	0 to 180	Spanwise Distribution Angle (Deg.)
Γ	$0 < \Gamma(\theta) < 1$	Spanwise Distribution Fourier Sine Series
C_ℓ^0	0.1252	Intercept lift coefficient @ $\alpha = 0^\circ$
C_ℓ^α	2π	Thin Foil Lift Slope Curve Coefficient
V_∞	200	Airspeed (km/h)
Alt	10000	Altitude (m)
q_∞	0.413	Air Density (kg/cu m)
P_∞	26.483	Air Pressure (kpa)
T_∞	-49	Air Temperature (Deg. C)
W_{wing}	1600	Physical Weight (N)
W_{norm}	$\frac{W_{wing}}{\cos(\alpha)}$	Normalized Weight (N)
L_{mgn}	150 to 400	Design Lift Margin (N)
L_i^{opt}	$> (W_{norm} + L_{mgn})$	Desired Lift Force (N)
D_i	< 300	Maximum Drag Force (N)
γ_i	0 to 30	Aspect View Angle WRT EM discipline (Deg.)
a_{rf}	$a_{ar}\cos(\gamma)$	Wing span WRT EM discipline (m)
b_{rf}	$b_{ar}\cos(\alpha)$	Chord WRT EM discipline (m)
E^{inc}	1	Incident E-field ($\frac{v}{m}$)
ϕ'	90	Incident E-field Angle (Deg.)
ϕ	0 to 90	Observation Angle Monostatic (Deg.)
f_o	9.0	Operating Frequency (GHz)
r_o	500	Observation Distance in RF wavelength (λ)
R_i^{opt}	< 0.4	Desired Backscattered Return Scalar

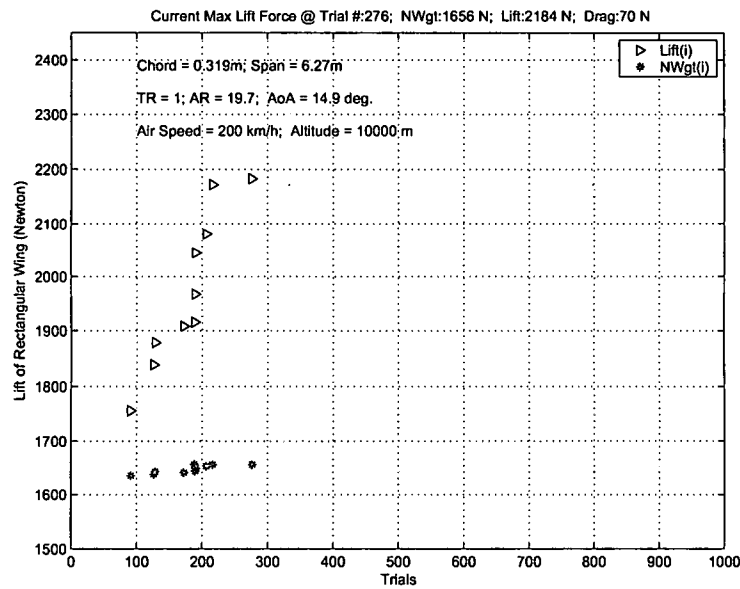


Figure 6.25: Current Max L_i and W_{Norm} of a rectangular wing; RectProbSet3

than Figure 6.29 with the same wing aspect ratio and angle of attack, but produces a much lower return of the electromagnetic backscatter and at the same time attains a higher lift value. Figure 6.33 is the optimum solution where the EM discipline has reached a greater lift force and a minimum backscattered field return. The 10° median filter waveform of Figure 6.33 is shown in Figure 6.34. A composite of simulated data of additional runs per Table 6.5 was tabulated and shown in Table 6.6.

Data shown in Table 6.6, Run #1, #2, #8, and #9 provide trade-offs between the Aero and EM disciplines. A decision would be made to have lower lift with lower backscattered field return, or higher lift with higher backscattered field return based on the environmental control parameters. However, the backscattered field returns on Run #6 are fairly close with the addition of 193N of lift force with

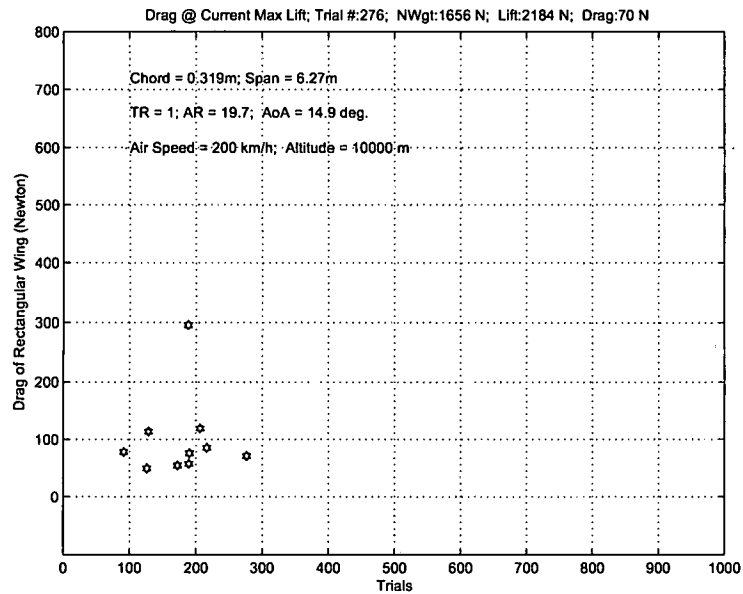


Figure 6.26: Current Drag force D_i of a rectangular wing; RectProbSet3

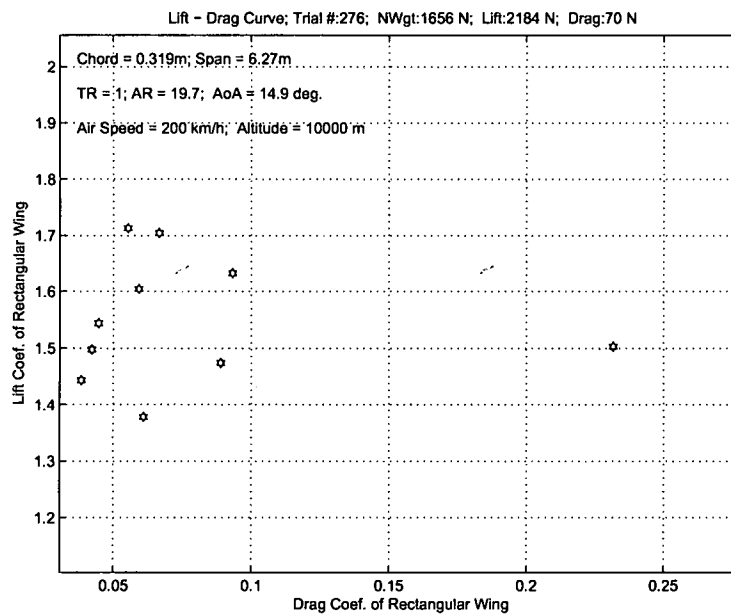


Figure 6.27: Lift Coeff. C_l vs. Drag Coeff. C_d of a rectangular wing; RectProbSet3

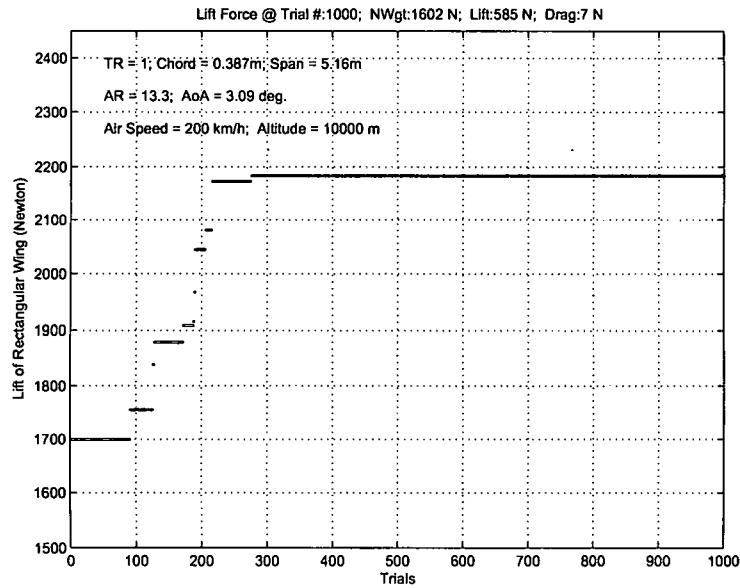


Figure 6.28: Lift force (L_i) of a rectangular wing; RectProbSet3

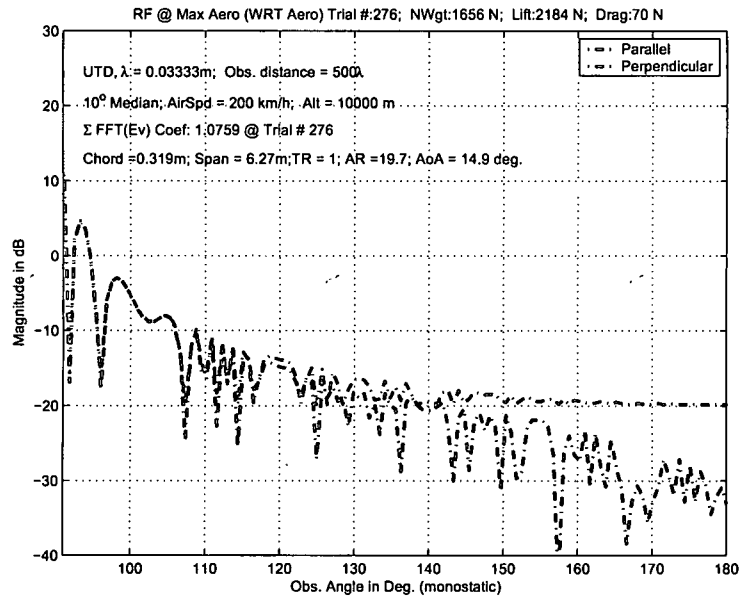


Figure 6.29: Current R_i @ $\text{Max}(L_i)$ WRT Aero Discipline of a rectangular wing; RectProbSet3

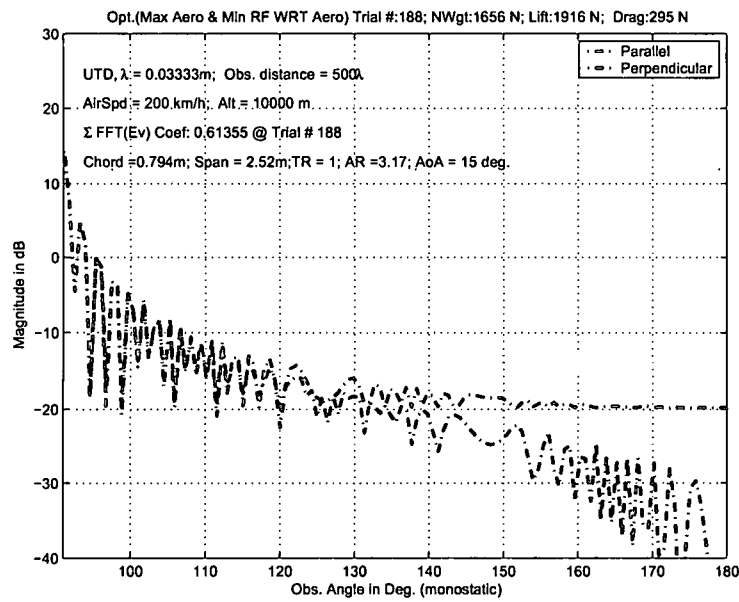


Figure 6.30: Optimal: $\text{Max}(L_i)$ & $\text{Min}(R_i)$ WRT Aero Discipline of a rectangular wing; RectProbSet3

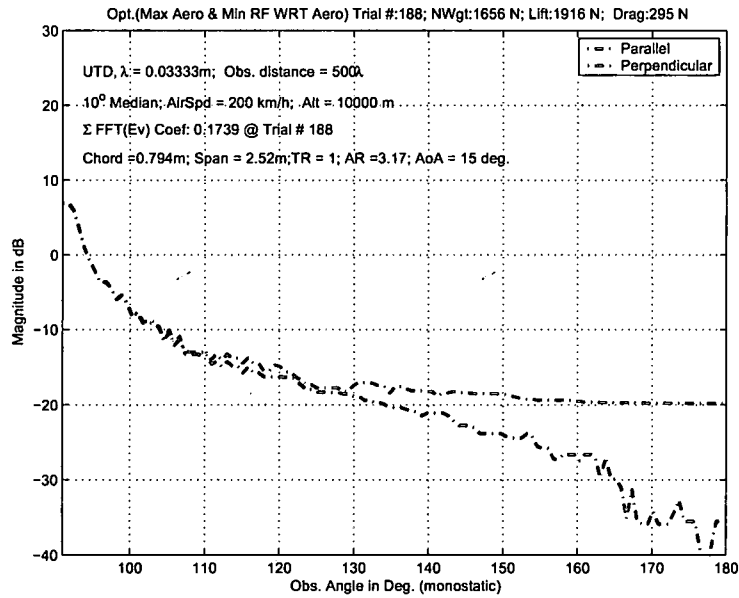


Figure 6.31: Optimal: $\text{Max}(L_i)$ & $\text{Min}(R_i)$ w/ 10° median WRT Aero Discipline of a rectangular wing; RectProbSet3

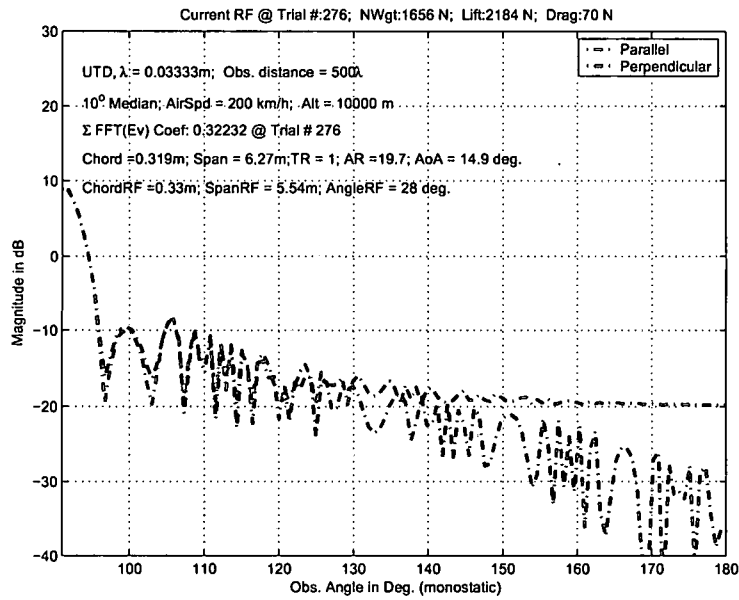


Figure 6.32: Current $\text{Min}(R_i) @ \text{Max}(L_i)$ WRT EM Discipline of a rectangular wing; RectProbSet3

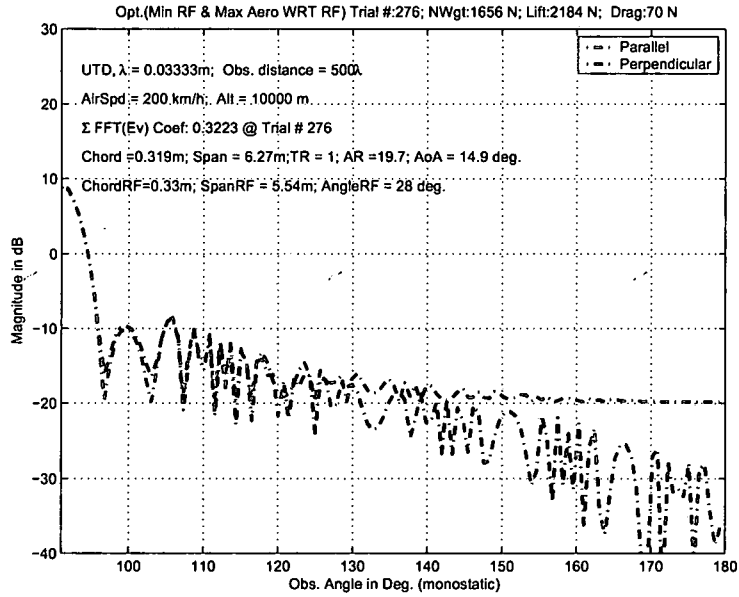


Figure 6.33: Optimal: $\text{Min}(R_i) \& \text{Max}(L_i)$ WRT EM Discipline of a rectangular wing; PProbSet3

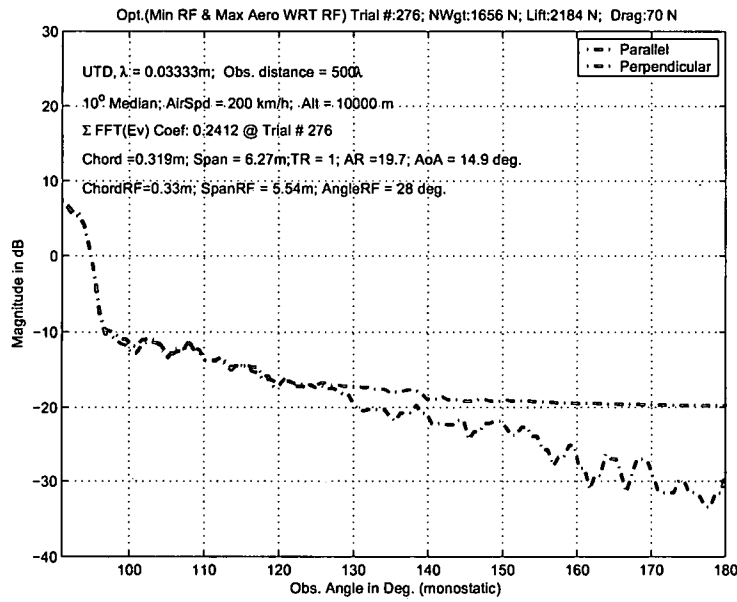


Figure 6.34: Optimal: $\text{Min}(R_i)$ w/10° median & $\text{Max}(L_i)$ WRT EM Discipline of a rectangular wing; RectProbSet3

respect to the EM discipline. According to the simulated data shown in Table 6.6, the EM discipline has a slight advantage over the Aero discipline in attaining more optimal solutions in the context of design optimization among two distinctive disciplines. The rectangular wing planform shape with large wing aspect ratio results in having a lower induced drag.

Unlike Modified Concurrent Subspace Optimization Method (MDCSSO) [103] where a constrained minimum point is needed to prevent premature convergence, SMA deploys the mutation method where both minimum and maximum function will always converge at any arbitrarily constrained point. Each set of optimization solutions (Aero or EM discipline) is derived without compromising one another since the mutation process will retain the last best optimum data set. The

simulated data shown in Table 6.2, 6.4, and 6.6 have similar randomness characteristics. The ability to capture all those optimal data points allows a trade-off study and the analysis of "best" case scenario which would be invaluable in a complex system since each discipline function improves (maximize or minimize) simultaneously without degrading other functions through out the mutating process.

6.3 COMPUTATIONAL DATA OF A TAPERED WING PLANFORM

For a given wingspan and speed, induced drag due to lift is minimized with an elliptical distribution of wing spanwise loading according to the lifting line theory. Analysis of induced drag of a highly swept and tapered wing [104] indicated a tapered wing would provide lower induced drag. Further more, wings with various planform shapes and tip geometries cited in [105] might also improve the fundamental drag reduction. And the approximations involved in lifting line theory [106] highlighted that overestimate tip loading leads to larger estimated induced drag force for a rectangular wing planform than are predicted by more refined potential methods. A finite wing with linearly tapered planform shown in Figure 6.35 will be used to illustrate the effect on lift force due to the tapered ratio, along with the respective wing aspect ratio bounded by the constraint of same wing surface area is shown in Figure 6.36. Table 6.7 is the environmentally controlled parameters used to analyze the tapered wing performance and compare it to those rectangular wing data.

The converged lift force and the optimum lift with its wing loading weight are shown in Figures 6.37 and 6.38, respectively. The induced drag force data due to

Table 6.6: Computed MDO Data of Table 6.5 Controlled Parameters

RectProbSet3	Trial i^{th}	AR	α°	L_i (N)	D_i (N)	γ°	R_i
Run #1	23	20.6	11.6	1740	43	0	0.160 [‡]
Run #1	111	18.3	14.8	2165	74	15.7	0.285 [†]
Run #2	15	12.3	12.4	1829	75	0	0.167 [‡]
Run #2	196	19.8	14.4	2120	66	26.5	0.279 [†]
Run #3	59	9.03	13.7	1967	115	0	0.359 [‡]
Run #3	59	9.03	13.7	1967	115	24.1	0.154 [†]
Run #4	12	15.7	11.1	1666	50	0	0.353 [‡]
Run #4	33	16.4	12.2	1812	57	20.1	0.228 [†]
Run #5	17	8.62	11.8	1725	93	0	0.224 [‡]
Run #5	419	20.0	14.7	2154	67	29.5	0.189 [†]
Run #6	35	4.02	14.9	1967	247	0	0.265 [‡]
Run #6	462	16.4	14.8	2160	81	21.0	0.264 [†]
Run #7	144	14.5	13.3	1947	73	0	0.205 [‡]
Run #7	196	15.0	14.3	2083	82	8.80	0.180 [†]
Run #8	16	21.1	11.6	1743	42	0	0.156 [‡]
Run #8	279	8.30	14.2	2016	131	10.9	0.255 [†]
Run #9	188	3.17	15.0	1916	295	0	0.174 [‡]
Run #9	276	19.7	14.9	2184	70	28.0	0.241 [†]
Run #10	122	7.88	13.0	1855	116	0	0.275 [‡]
Run #10	129	17.0	12.7	1855	60	22.7	0.225 [†]

‡ Max L_i & Min R_i with respect to Aero discipline

† Min R_i & Max L_i with respect to EM discipline

every optimum lift shown in Figure 6.39 remains fairly close throughout the trials even with a large increase in lift force from Trial #70 to #200. The lift force reaches its diminished return beyond Trial #200. Unlike Multi-Objective Pareto concurrent subspace optimization [103], SMA does not have to deal with the cumulative constraint violations due to the fact that all the design variables and constraints are randomized at each trial and the mutation processor will always obtain an optimum set of solutions that couple between the Aero and EM disciplines. However, ranking of design variables and their corresponding constraints may be conducted according to priority. Refer to Figure 6.38. The computational time to seek additional lift beyond Trial #300 seemed inefficient but it may be necessary since no one critical constraint dominates the SMA optimization process.

Figure 6.40 revealed the current backscattered scalar sum $R_{334} = 0.804$ which is less than the previous $R_{41} = 0.935$ shown in Figure 6.41 with respect to the Aero discipline, but it is greater than $R_{334} = 0.218$ with respect to the EM discipline shown in Figure 6.42. Hence, the most recent maximum lift force $L_{802} = 2494$ shown in Figure 6.43 failed to meet the EM discipline criteria $R_{802} \leq R_{334}$ and the SMA mutation processor continues. The maximum lift with minimum backscattered field and its corresponding induced drag force of 111N with respect to the Aero discipline is shown in Figure 6.44, and the minimum backscattered return with maximum lift and a drag force of 84N with respect to the EM discipline is shown in Figure 6.45. Clearly, the solution derived with respect to the EM discipline is far better than the one obtained from the Aero discipline bounded by the same wing surface area and mass. The factors affecting the outcome are the wing tip tapered ratio, wing aspect ratio, angle of attack, and aspect view angle in the azimuth plane.

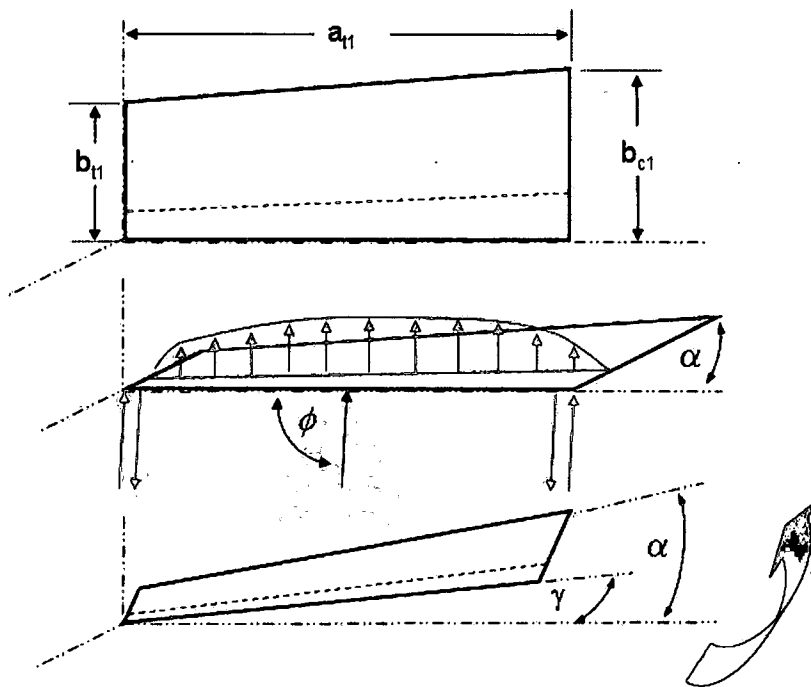


Figure 6.35: Low aspect ratio of a finite thin tapered wing

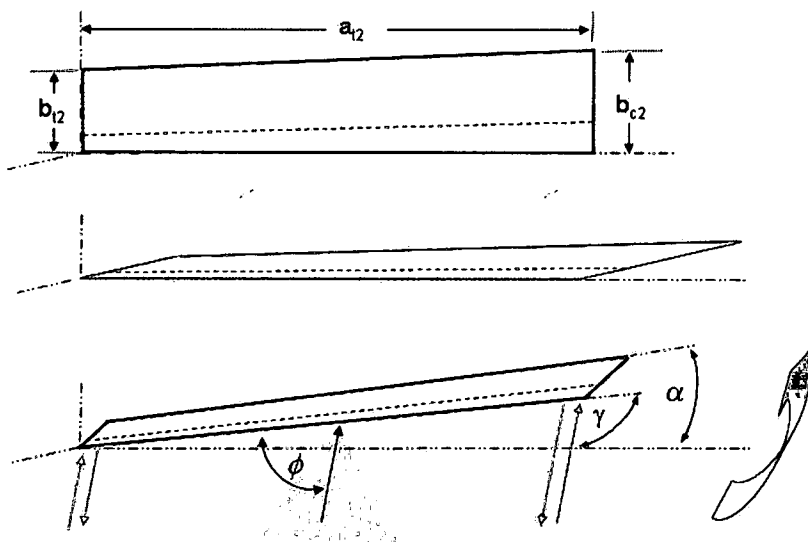


Figure 6.36: High aspect ratio of a finite thin tapered wing

Table 6.7: Control Parameters of a Tapered Wing Optimization: TapProbSet1

Variable	Value	Description
a_{ar}	2	Wing span (m)
TR_i	10 to 100	Tapered Wing Ratio (%)
AR_i	2 to 20	Wing Aspect Ratio
S_{wing}	2	Wing Surface Area (m^2)
α_i	0 to 15	Angle of Attack (Deg.)
θ	0 to 180	Spanwise Distribution Angle (Deg.)
Γ	$0 < \Gamma(\theta) < 1$	Spanwise Distribution Fourier Sine Series
C_ℓ^0	0.1252	Intercept lift coefficient @ $\alpha = 0^\circ$
C_ℓ^α	2π	Thin Foil Lift Slope Curve Coefficient
V_∞	160	Airspeed (km/h)
Alt	5000	Altitude (meter)
q_∞	0.736	Air Density (kg/cu m)
P_∞	54.042	Air Pressure (kpa)
T_∞	-17	Air Temperature (Deg. C)
W_{wing}	1600	Physical Weight (N)
W_{norm}	$\frac{W_{wing}}{\cos(\alpha)}$	Normalized Weight (N)
L_{mgn}	150 to 400	Design Lift Margin (N)
L_i^{opt}	$> (W_{norm} + L_{mgn})$	Desired Lift Force (N)
D_i	< 300	Maximum Drag Force (N)
γ_i	0 to 30	Aspect View Angle WRT EM discipline (Deg.)
a_{rf}	$a_{ar}\cos(\gamma)$	Wing span WRT EM discipline (m)
b_{rf}	$b_{ar}\cos(\alpha)$	Chord WRT EM discipline (m)
E^{inc}	1	Incident E-field ($\frac{V}{m}$)
ϕ'	90	Incident E-field Angle (Deg.)
ϕ	0 to 90	Observation Angle Monostatic (Deg.)
f_o	9.0	Operating Frequency (GHz)
r_o	500	Observation Distance in RF wavelength (λ)
R_i^{opt}	< 0.4	Desired Backscattered Return Scalar

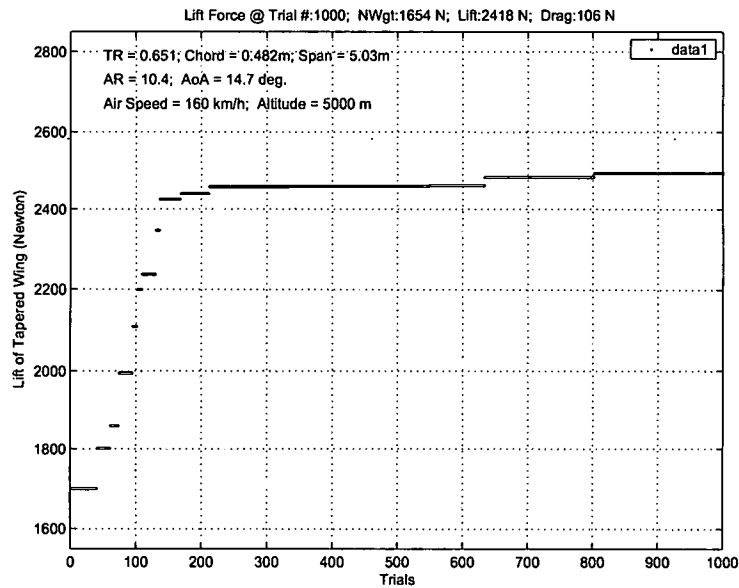


Figure 6.37: Lift force (L_i) of a tapered wing; TapProbSet1

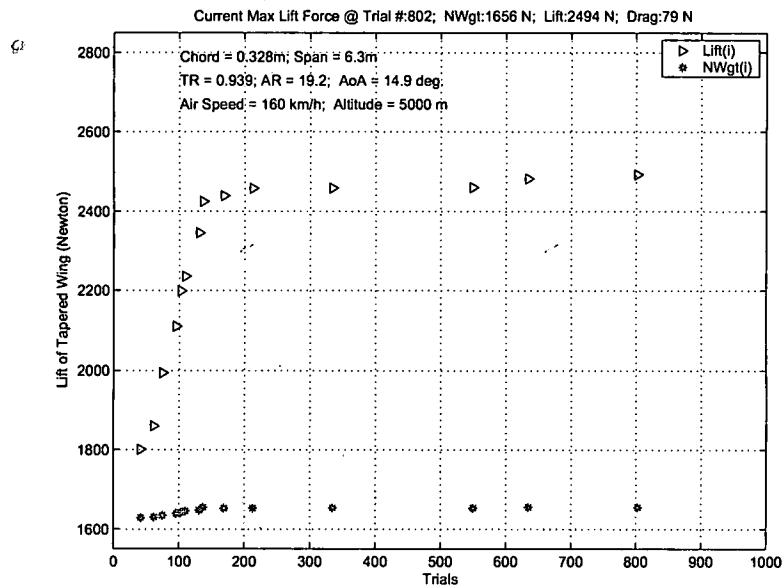


Figure 6.38: Current Max L_i and W_{Norm} of a tapered wing; TapProbSet1

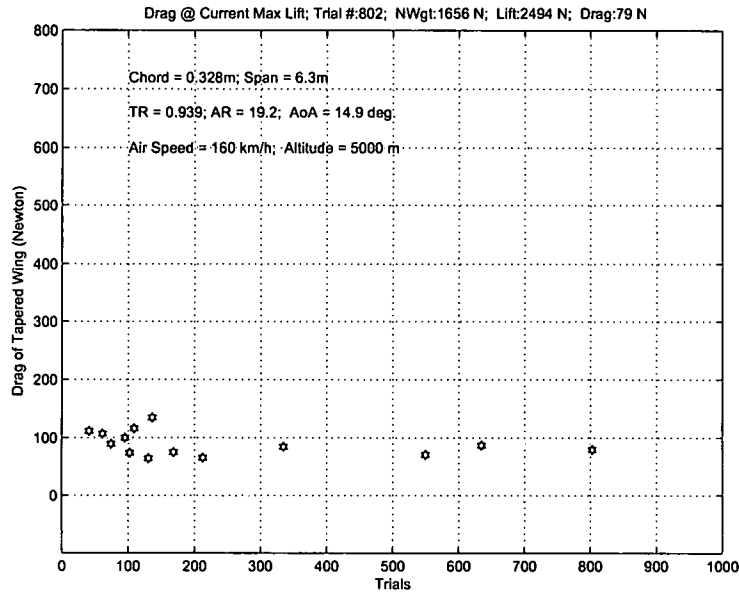


Figure 6.39: Current Drag force D_i of a tapered wing; TapProbSet1

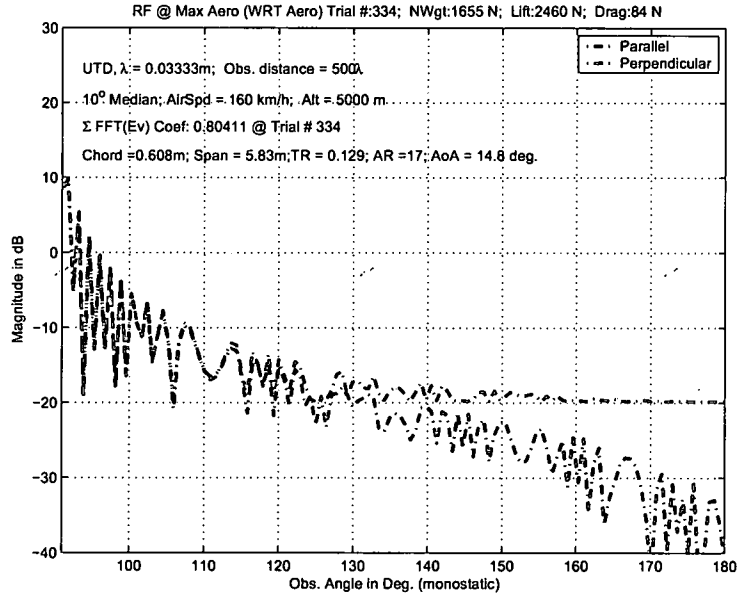


Figure 6.40: Current R_i @ $\text{Max}(L_i)$ WRT Aero Discipline of a tapered wing; TapProbSet1

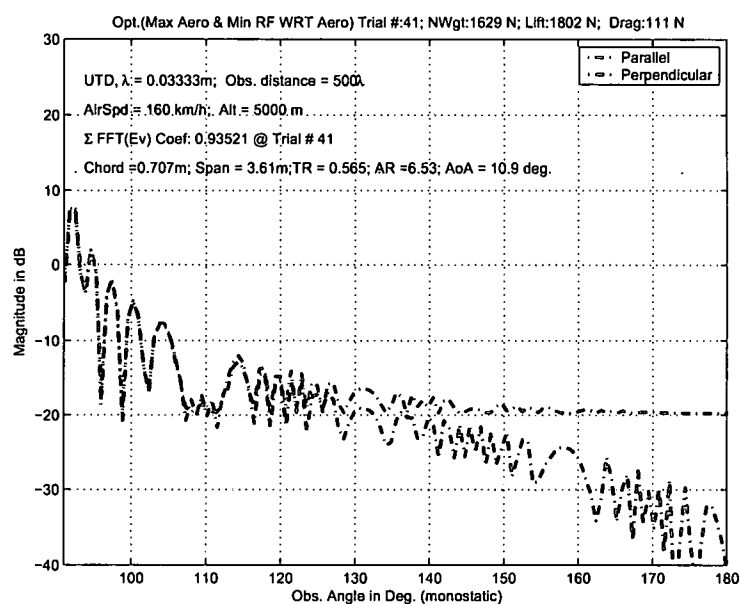


Figure 6.41: Optimal: $\text{Max}(L_i)$ & $\text{Min}(R_i)$ WRT Aero Discipline of a tapered wing; TapProbSet1

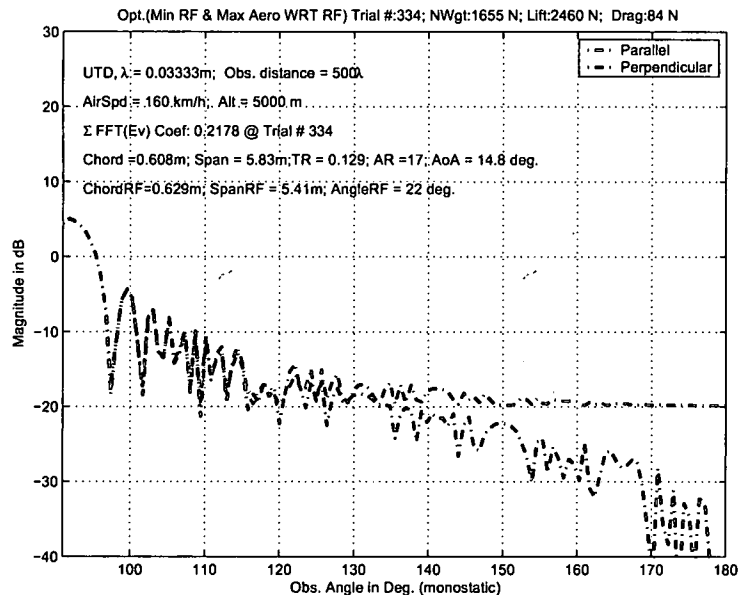


Figure 6.42: Optimal: $\text{Min}(R_i)$ & $\text{Max}(L_i)$ WRT EM Discipline of a tapered wing; TapPProbSet1

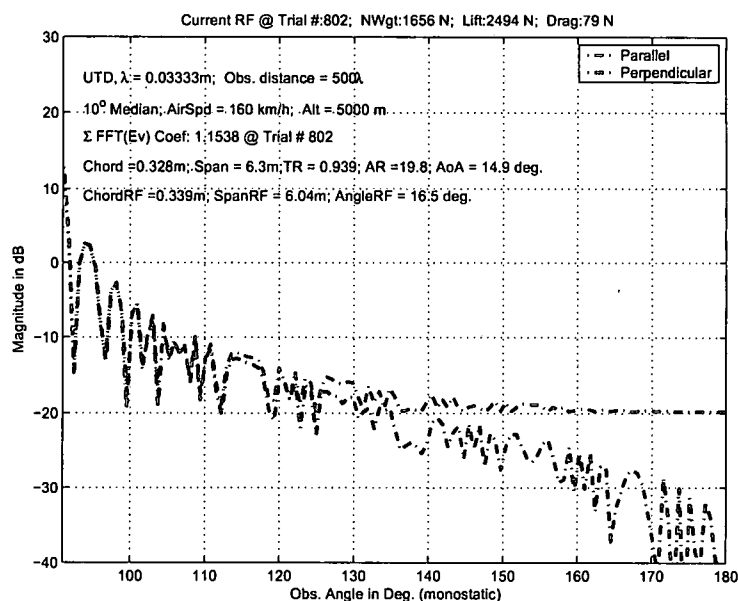


Figure 6.43: Current $\text{Min}(R_i)$ @ $\text{Max}(L_i)$ WRT EM Discipline of a tapered wing; TapProbSet1

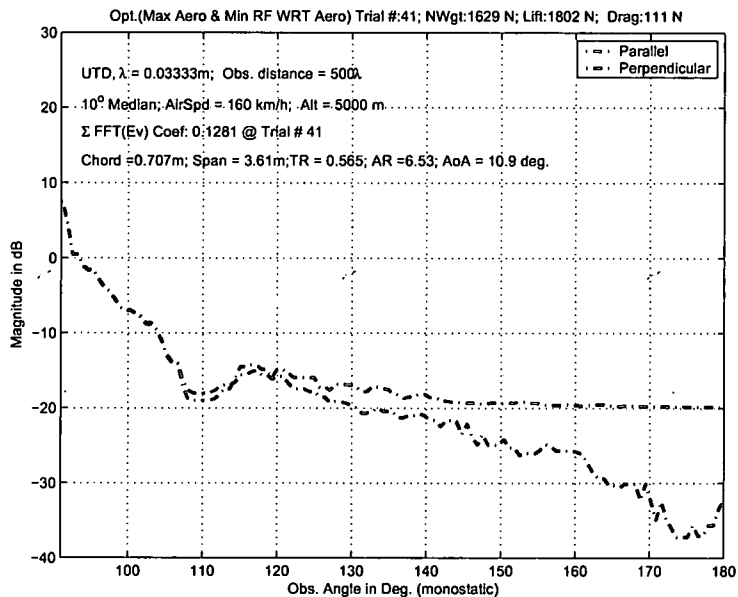


Figure 6.44: Optimal: $\text{Max}(L_i)$ & $\text{Min}(R_i)$ w/ 10° median WRT Aero Discipline of a tapered wing; TapProbSet1

Table 6.8: Simulated Tapered Wing Data of TapProbSet1 (Table 6.7)

TapProbSet1	Trial i^{th}	TR	AR	α^o	L_i (N)	D_i (N)	γ^o	R_i
Run #1	59	0.763	14.1	10.4	1783	53	0	0.351 [‡]
Run #1	59	0.763	14.1	10.4	1783	53	16.4	0.277 [†]
Run #2	58	0.331	13.6	11.0	1874	58	0	0.144 [‡]
Run #2	95	0.953	4.23	13.5	2088	232	23.0	0.268 [†]
Run #3	63	0.387	8.77	12.4	2050	108	0	0.280 [‡]
Run #3	108	0.972	8.71	14.5	2354	149	7.70	0.199 [†]
Run #4	985	0.893	21.9	14.9	2496	71	0	0.203 [‡]
Run #4	985	0.893	21.9	14.9	2496	71	5.13	0.049 [†]
Run #5	47	0.496	7.24	13.6	2189	147	0	0.117 [‡]
Run #5	79	0.740	14.6	14.7	2426	95	15.5	0.144 [†]
Run #6	99	0.295	22.0	12.0	2053	44	0	0.227 [‡]
Run #6	142	0.973	20.6	13.5	2280	64	26.0	0.171 [†]
Run #7	310	0.534	21.6	14.7	2464	65	0	0.130 [‡]
Run #7	310	0.534	21.6	14.7	2438	70	6.32	0.110 [†]
Run #8	135	0.588	7.08	11.9	1947	120	0	0.165 [‡]
Run #8	490	0.467	20.6	14.9	2492	69	28.2	0.191 [†]
Run #9	55	0.671	17.3	9.78	1704	39	0	0.038 [‡]
Run #9	129	0.618	9.74	12.6	2082	101	21.5	0.015 [†]
Run #10	18	0.988	5.14	11.2	1821	147	0	0.061 [‡]
Run #10	70	0.465	12.8	14.7	2154	103	25.9	0.056 [†]

‡ Max L_i & Min R_i with respect to Aero discipline

† Min R_i & Max L_i with respect to EM discipline

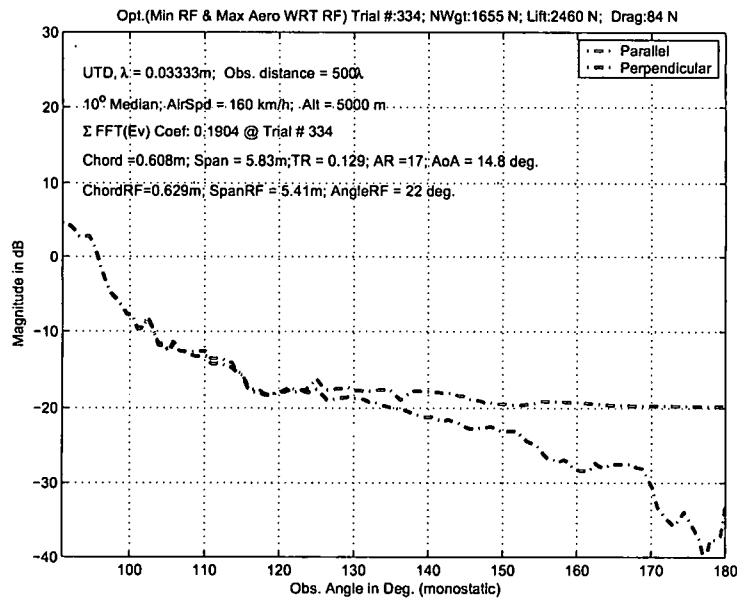


Figure 6.45: Optimal: $\text{Min}(R_i)$ w/ 10° median & $\text{Max}(L_i)$ WRT EM Discipline of a tapered wing; TapProbSet1

Table 6.8 listed 10 optimum data sets tabulated from over 50 trials to establish a normal random distribution where trade-off study or alternate analysis can be derived from these sample data. 7 sets of the tabulated data (Run # 1, 3, 4, 6, 7, 9, and 10) are the optimized solutions with respect to the EM discipline bounded by the wing planform shape indicated. SMA does not rank the constraints and the optimization processor converges to an optimum, single solution set or SMA optimal set with respect to either the Aero or EM disciplines. Whereas the Pareto genetic algorithm [107] for multi-objective optimization seeks to optimize a vector-valued objective with a family of points known as Pareto-optimal set. One of the benefits in SMA optimization is that no constraints deduction to a single criterion is needed

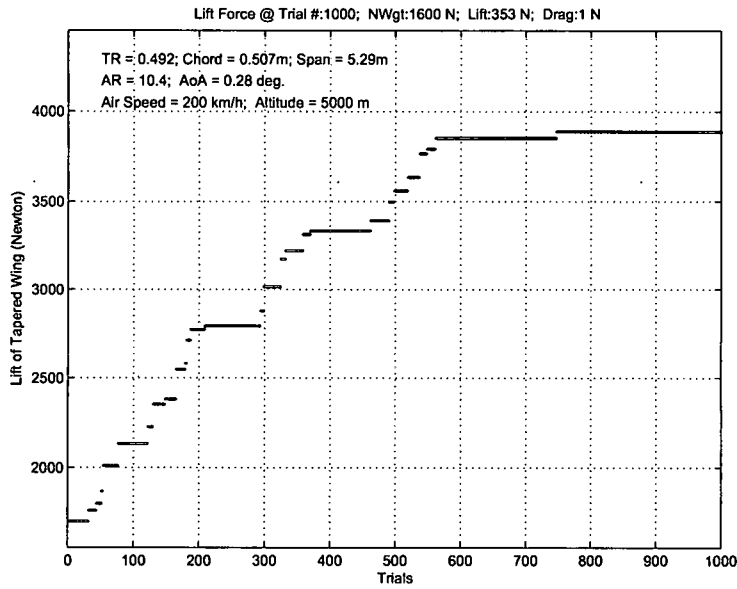


Figure 6.46: Lift force (L_i) of a tapered wing; TapProbSet2

to solve optimization problems concurrently and allow trade-off among two distinctive disciplines.

The second test case scenario, Table 6.9 shows the environmental parameters to the same tapered wing planform with a higher airspeed. The additional airspeed does not necessarily produce lift proportionally to Equation (5.16). The converged lift force shown in Figure 6.46 increases or improves gradually and each of the optimum lift forces L_i shown in Figure 6.47 is far greater than its corresponding normalized wing loading weight W_{Norm} . Figure 6.48 shows a moderately higher induced drag force, however, most of them are less than 300N, except one which exceeds 450N. Figure 6.49 depicts a snap shot of the lift coefficient C_l vs. the induced drag coefficient C_d . The high drag coefficient shown corresponds to $C_l = 1.4$ and links to a lift force $L_{320} = 3040N$ but is not the optimum solution.

Table 6.9: Control Parameters of a Tapered Wing Optimization: TapProbSet2

Variable	Value	Description
a_{ar}	2	Wing span (m)
TR_i	10 to 100	Tapered Wing Ratio (%)
AR_i	2 to 20	Wing Aspect Ratio
S_{wing}	2	Wing Surface Area (m^2)
α_i	0 to 15	Angle of Attack (Deg.)
θ	0 to 180	Spanwise Distribution Angle (Deg.)
Γ	$0 < \Gamma(\theta) < 1$	Spanwise Distribution Fourier Sine Series
C_ℓ^o	0.1252	Intercept lift coefficient @ $\alpha = 0^\circ$
C_ℓ^α	2π	Thin Foil Lift Slope Curve Coefficient
V_∞	200	Airspeed (km/h)
Alt	5000	Altitude (meter)
q_∞	0.736	Air Density (kg/cu m)
P_∞	54.042	Air Pressure (kpa)
T_∞	-17	Air Temperature (Deg. C)
W_{wing}	1600	Physical Weight (N)
W_{norm}	$\frac{W_{wing}}{\cos(\alpha)}$	Normalized Weight (N)
L_{mgn}	150 to 400	Design Lift Margin (N)
L_i^{opt}	$> (W_{norm} + L_{mgn})$	Desired Lift Force (N)
D_i	< 300	Maximum Drag Force (N)
γ_i	0 to 30	Aspect View Angle WRT EM discipline (Deg.)
a_{rf}	$a_{ar}\cos(\gamma)$	Wing span WRT EM discipline (m)
b_{rf}	$b_{ar}\cos(\alpha)$	Chord WRT EM discipline (m)
E^{inc}	1	Incident E-field ($\frac{v}{m}$)
ϕ'	90	Incident E-field Angle (Deg.)
ϕ	0 to 90	Observation Angle Monostatic (Deg.)
f_o	9.0	Operating Frequency (GHz)
r_o	500	Observation Distance in RF wavelength (λ)
R_i^{opt}	< 0.4	Desired Backscattered Return Scalar

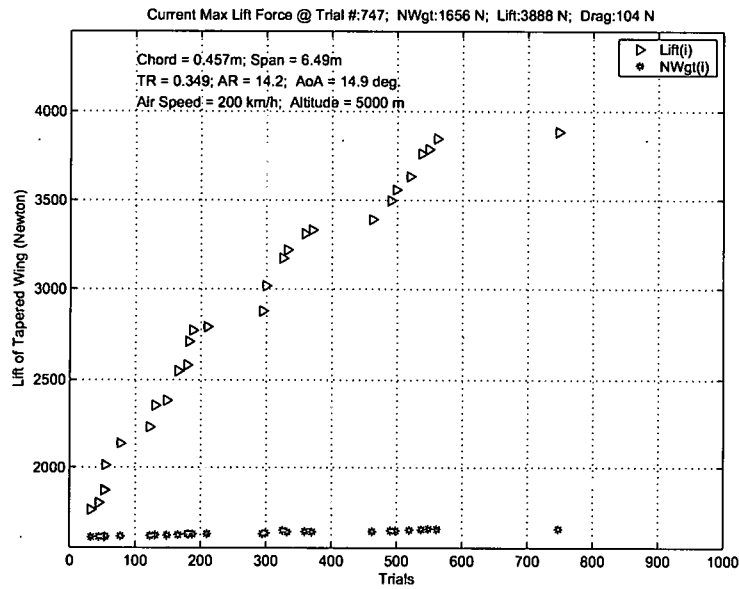


Figure 6.47: Current Max L_i and W_{Norm} of a tapered wing; TapProbSet2

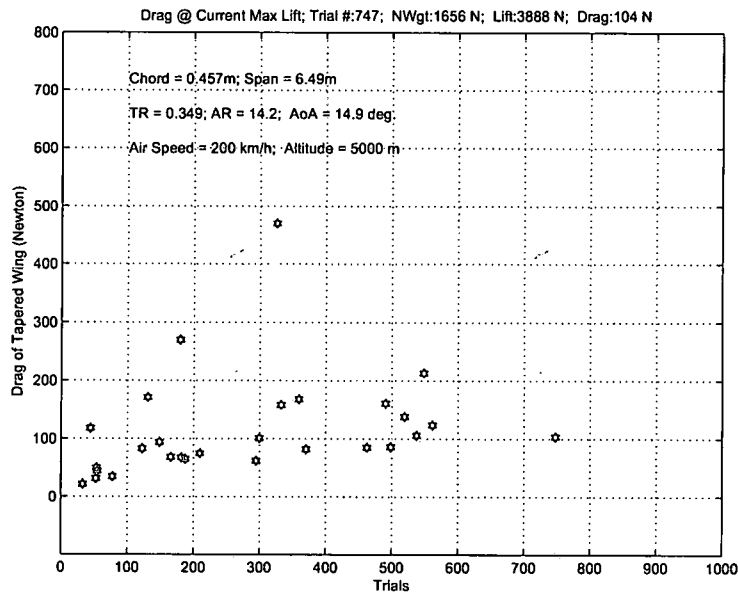


Figure 6.48: Current Drag force D_i of a tapered wing; TapProbSet2

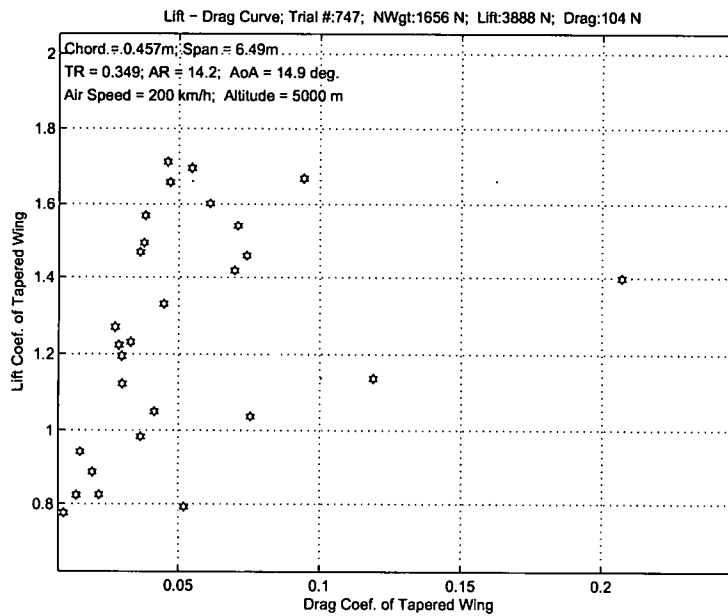


Figure 6.49: Lift Coeff. C_L vs. Drag Coeff. C_D of a tapered wing; TapProbSet2

Figure 6.50 indicates a minimum backscattered field return at $L_{498} = 3561N$ with respect to the Aero discipline and its 10° median filter waveform is shown in Figure 6.51. However, the minimum backscattered return was attained at Trial #561 with maximum $L_{561} = 3851N$ with respect to the EM discipline as shown in Figure 6.52. Figure 6.53 is its 10° median filter waveform. Both backscattered returns shown in Figures 6.51 and 6.53 have similar frequency spectrum except that the EM discipline has a relatively lower RF component scalar.

Data of various tapered wing planform are recorded in Table 6.10. 4 out of 10 data sets, Run #6, 7, 8, and 9 are the optimum solutions with respect to the EM discipline comparing 7 out of 10 data sets shown in Table 6.8. Compared to those data shown in Table 6.7, the additional increase in airspeed (40 km/h) produces a much higher lift force while the corresponding induced drag remain less than 200N.

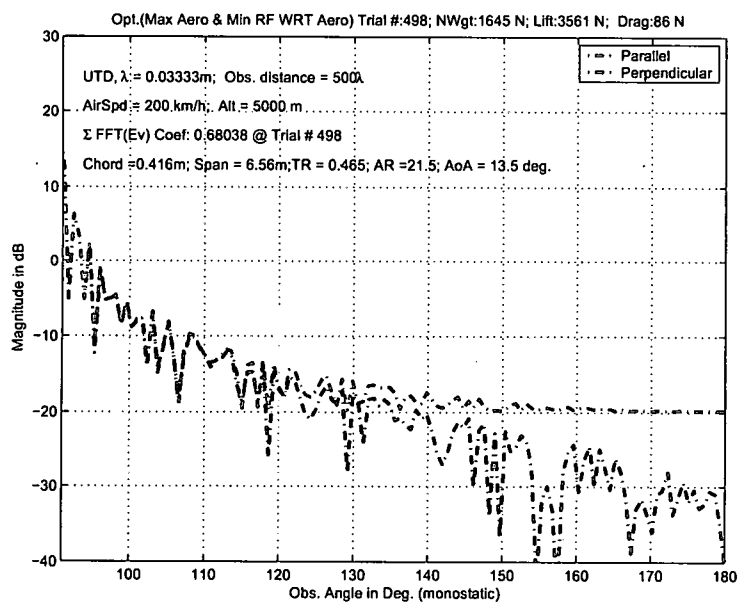


Figure 6.50: Optimal: $\text{Max}(L_i)$ & $\text{Min}(R_i)$ WRT Aero Discipline of a tapered wing; TapProbSet2

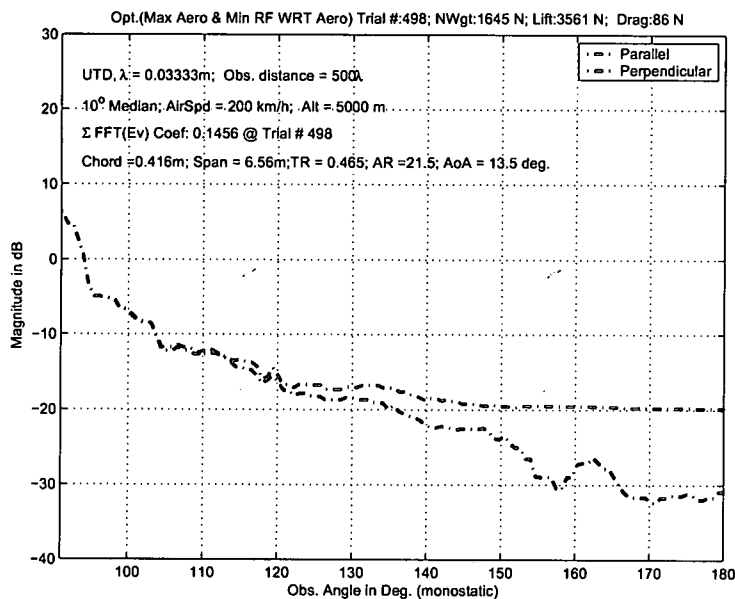


Figure 6.51: Optimal: $\text{Max}(L_i)$ & $\text{Min}(R_i)$ w/10° median WRT Aero Discipline of a tapered wing; TapProbSet2

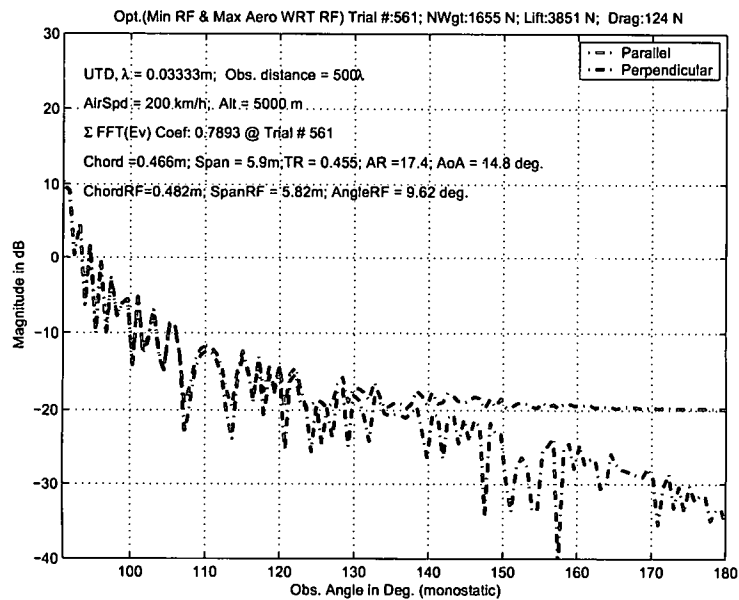


Figure 6.52: Optimal: $\text{Min}(R_i)$ & $\text{Max}(L_i)$ WRT EM Discipline of a tapered wing; TapPProbSet2

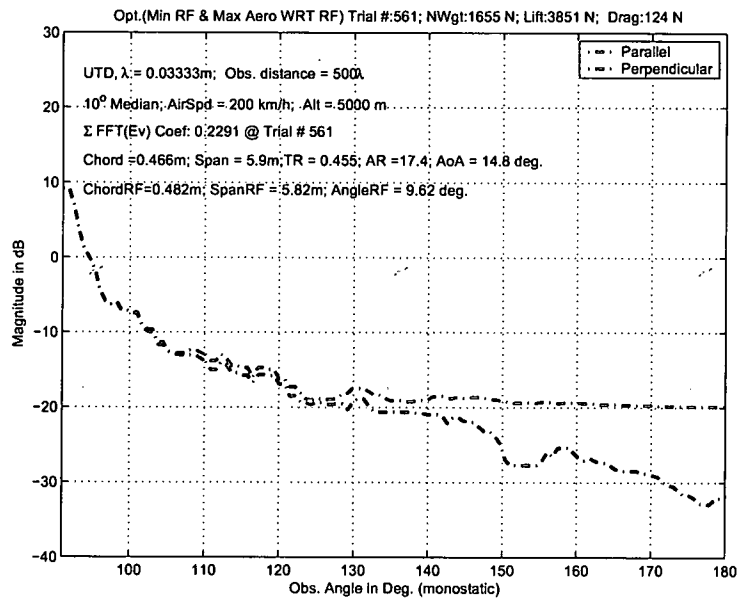


Figure 6.53: Optimal: $\text{Min}(R_i)$ w/ 10° median & $\text{Max}(L_i)$ WRT EM Discipline of a tapered wing; TapProbSet2

Most of the induced drag forces are relatively low correlated to a much higher lift force. One of which, $D_{12} = 23N$ corresponds to a high aspect ratio $AR = 20.5$ with a marginal lift force $L_{12} = 1734N$ and a fairly low backscattered return. Obviously, Run #3, 8, and 10 consist of the best case solution among the 10 data sets. All three have lift forces exceeding 3820N with induced drag forces less than 150N, and backscattered field return spectral density scalars lower than 0.165. Run #10 attained the optimum solution at Trial #975 on the limit of 1000. Hence, the higher number of trials would certainly improve the odds of obtaining the optimal solution.

The last test scenario is shown in Table 6.11. The altitude has changed from 5000 m to 10000 m. The atmospheric effect, thinner air density due to high altitude, is compensated by the 200 km/h airspeed. The complementary effect resulted by thinner air density and the converged lift force shown in Figure 6.54 reaches top lift force by trial #100. Figure 6.55 shows the optimum lift force attained beyond Trial # 840. Figure 6.56 depicts a moderate induced drag forces except one exceeds the norm, at $\sim 200N$. However, the lift coefficient C_ℓ vs. the induced drag coefficient C_d shown in Figure 6.57 reveals that one is anomalous.

The induced drag forces shown in Figure 6.39 (160 km/h at 5000m) and Figure 6.56 (200 km/h at 10000) vary slightly, and similar conclusion can be made for the lift forces as well. Figure 6.58 shows the current minimum backscattered field return optimal lift $L_{849} = 2194$ and Figure 6.30 is the optimum solution with respect to the Aero discipline $L_{611} = 2191$, and $R_{611} = 0.720$. The 10° median filter waveform is shown in Figure 6.60. With respect to the EM discipline side, Figure 6.61 depicts a lower backscattered field return than Figure 6.58 with the same wing tapered ratio, wing aspect ratio, wing surface area, and angle of attack, while Figure 6.61 has a

Table 6.10: Simulated Tapered Wing Data of TapProbSet2 (Table 6.9)

TapProbSet2	Trial i^{th}	TR	AR	α°	L_i (N)	D_i (N)	γ°	R_i
Run #1	475	0.114	13.8	13.9	3615	143	0	0.195 [‡]
Run #1	932	0.944	19.7	14.7	3840	120	22.2	0.219 [†]
Run #2	12	0.881	20.5	5.90	1734	23	0	0.112 [‡]
Run #2	238	0.209	5.56	9.47	2477	157	25.0	0.132 [†]
Run #3	470	0.449	21.5	13.4	3531	85	0	0.155 [‡]
Run #3	517	0.569	17.2	14.7	3829	126	28.8	0.163 [†]
Run #4	498	0.465	21.5	13.5	3561	86	0	0.146 [‡]
Run #4	561	0.455	17.4	14.8	3851	124	9.62	0.229 [†]
Run #5	317	0.295	13.0	10.4	2783	85	0	0.199 [‡]
Run #5	593	0.758	10.4	14.5	3701	195	12.0	0.232 [†]
Run #6	361	0.615	14.3	12.3	3240	108	0	0.271 [‡]
Run #6	486	0.323	16.9	14.5	3776	121	10.9	0.155 [†]
Run #7	403	0.163	21.9	12.4	3307	75	0	0.208 [‡]
Run #7	422	0.278	10.6	13.4	3460	161	18.7	0.100 [†]
Run #8	357	0.108	15.7	14.7	3822	141	0	0.358 [‡]
Run #8	357	0.108	15.7	14.7	3822	141	20.8	0.156 [†]
Run #9	584	0.811	15.9	13.9	3626	126	0	0.248 [‡]
Run #9	587	0.161	17.6	14.2	3705	116	16.3	0.155 [†]
Run #10	574	0.732	21.6	14.4	3780	102	0	0.140 [‡]
Run #10	975	0.590	16.3	14.9	3853	134	4.68	0.154 [†]

‡ Max L_i & Min R_i with respect to Aero discipline

† Min R_i & Max L_i with respect to EM discipline

Table 6.11: Control Parameters of a Tapered Wing Optimization: TapProbSet3.

Variable	Value	Description
a_{ar}	2	Wing span (m)
TR_i	10 to 100	Tapered Wing Ratio (%)
AR_i	2 to 20	Wing Aspect Ratio
S_{wing}	2	Wing Surface Area (m^2)
α_i	0 to 15	Angle of Attack (Deg.)
θ	0 to 180	Spanwise Distribution Angle (Deg.)
Γ	$0 < \Gamma(\theta) < 1$	Spanwise Distribution Fourier Sine Series
C_ℓ^0	0.1252	Intercept lift coefficient @ $\alpha = 0^\circ$
C_ℓ^α	2π	Thin Foil Lift Slope Curve Coefficient
V_∞	200	Airspeed (km/h)
Alt	10000	Altitude (meter)
q_∞	0.431	Air Density (kg/cu m)
P_∞	26.483	Air Pressure (kpa)
T_∞	-49	Air Temperature (Deg. C)
W_{wing}	1600	Physical Weight (N)
W_{norm}	$\frac{W_{wing}}{\cos(\alpha)}$	Normalized Weight (N)
L_{mgn}	150 to 400	Design Lift Margin (N)
L_i^{opt}	$> (W_{norm} + L_{mgn})$	Desired Lift Force (N)
D_i	< 300	Maximum Drag Force (N)
γ_i	0 to 30	Aspect View Angle WRT EM discipline (Deg.)
a_{rf}	$a_{ar}\cos(\gamma)$	Wing span WRT EM discipline (m)
b_{rf}	$b_{ar}\cos(\alpha)$	Chord WRT EM discipline (m)
E^{inc}	1	Incident E-field ($\frac{V}{m}$)
ϕ'	90	Incident E-field Angle (Deg.)

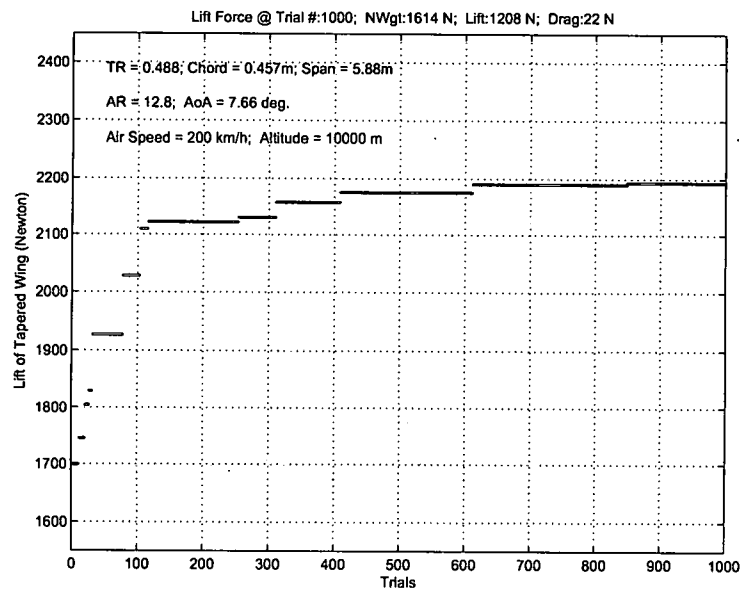


Figure 6.54: Lift force (L_i) of a tapered wing; TapProbSet3

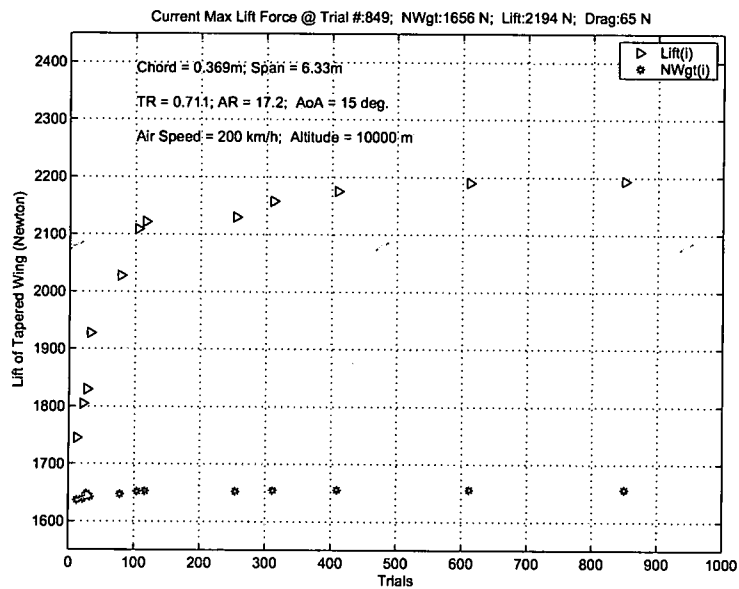


Figure 6.55: Current Max L_i and W_{Norm} of a tapered wing; TapProbSet3

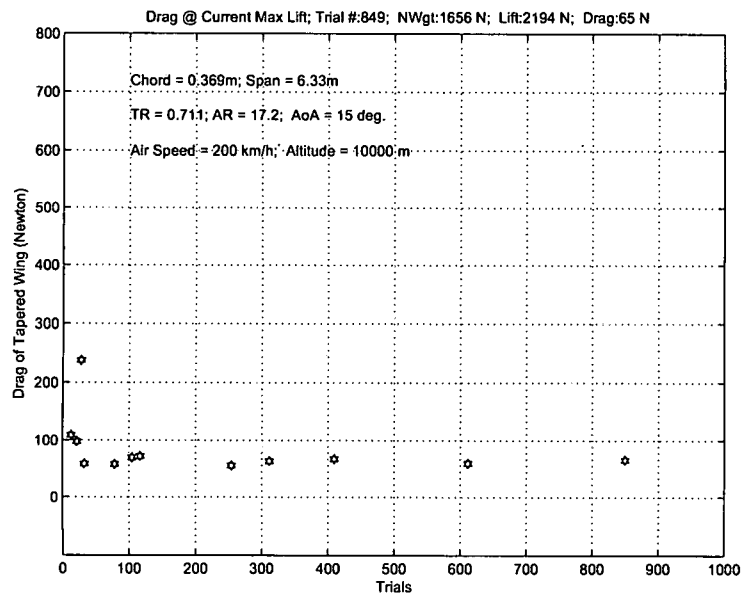
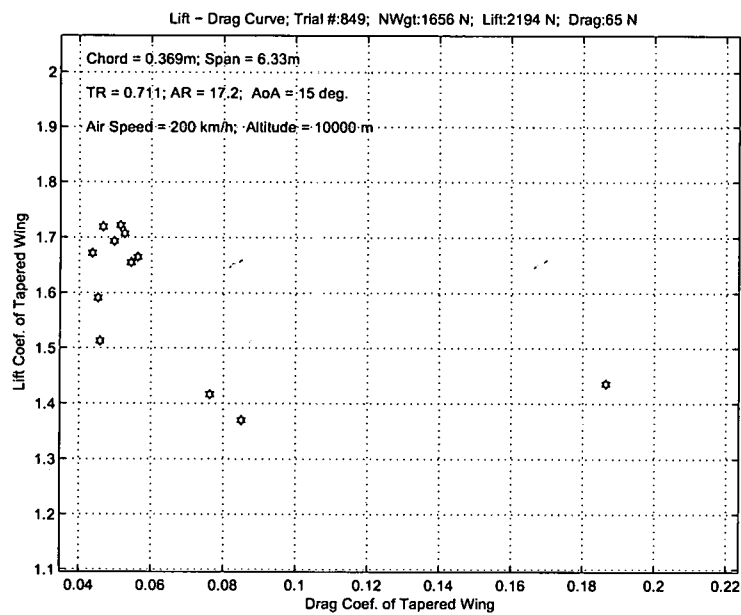


Figure 6.56: Current Drag force D_i of a tapered wing; TapProbSet3



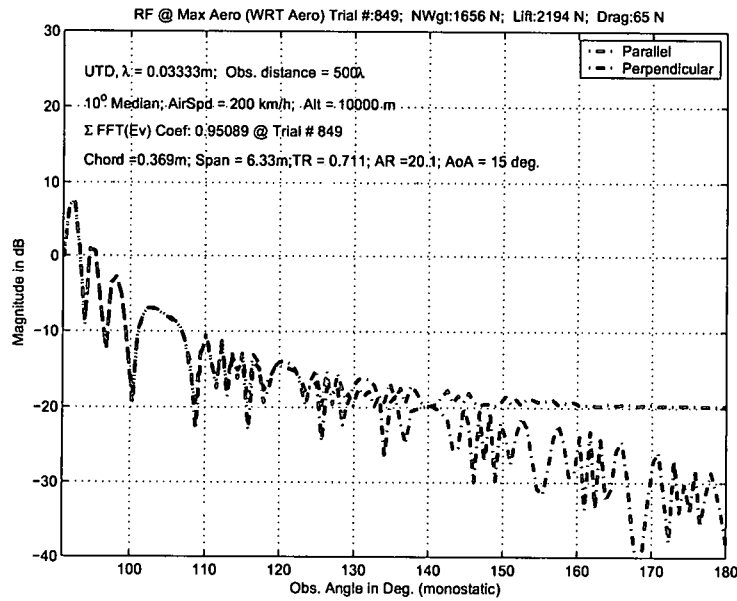


Figure 6.58: Current R_i @ $\text{Max}(L_i)$ WRT Aero Discipline of a tapered wing; Tap-ProbSet3

lower return of the electromagnetic backscatter. Figure 6.62 is the optimum solution for attaining a minimum backscattered field return and a maximum lift force.

Hence, EM discipline has reached a greater lift force and a lower backscattered field return. The 10° median filter waveform of Figure 6.62 is shown in Figure 6.63. A composite of simulated data runs per Table 6.11 was tabulated and is shown in Table 6.12.

Table 6.12 are simulated data of various tapered wing planform, 5 out of 10 data sets, Run #4, 6, 8, 9, and 10 are the optimum solutions with respect to the EM discipline, the additional increase in both airspeed (from 160km/h to 200km/h) and a higher altitude (from 5000 m to 10,000 m) produces similar lift force, induced drag force, and backscattered field returns. Even though SMA optimizes both

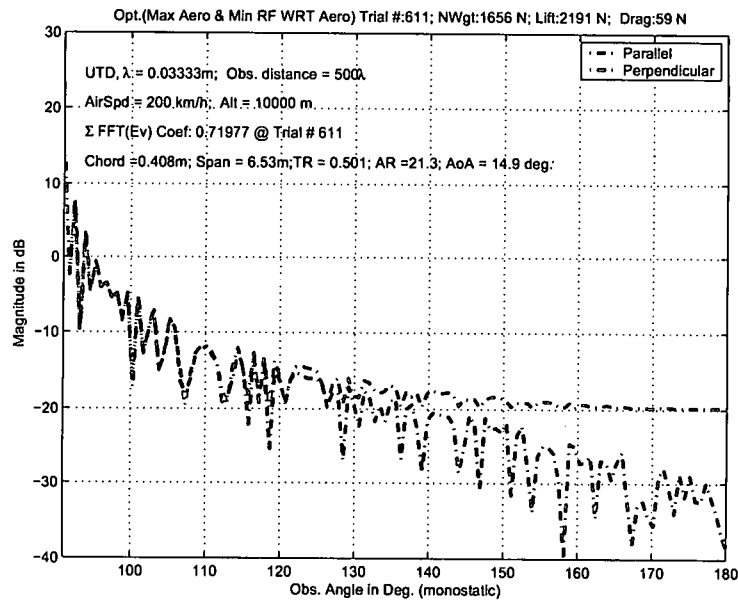


Figure 6.59: Optimal: $\text{Max}(L_i)$ & $\text{Min}(R_i)$ WRT Aero Discipline of a tapered wing; TapProbSet3

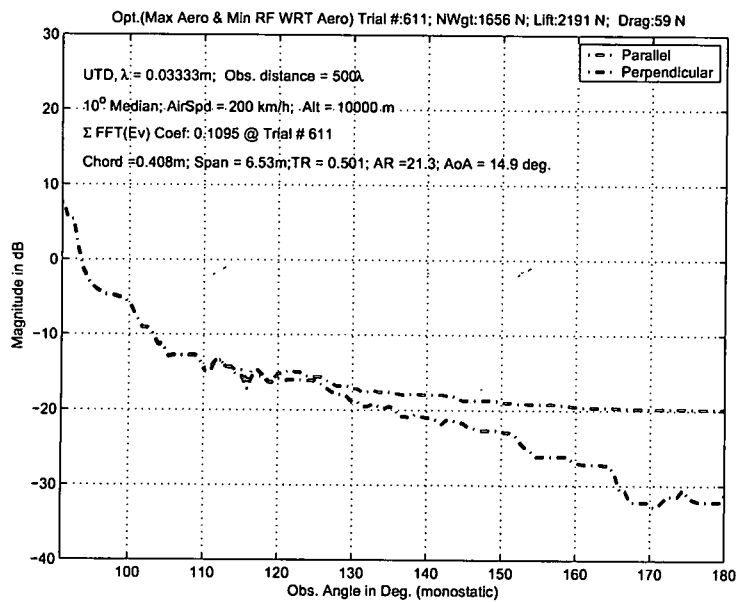


Figure 6.60: Optimal: $\text{Max}(L_i)$ & $\text{Min}(R_i)$ w/ 10° median WRT Aero Discipline of a tapered wing; TapProbSet3

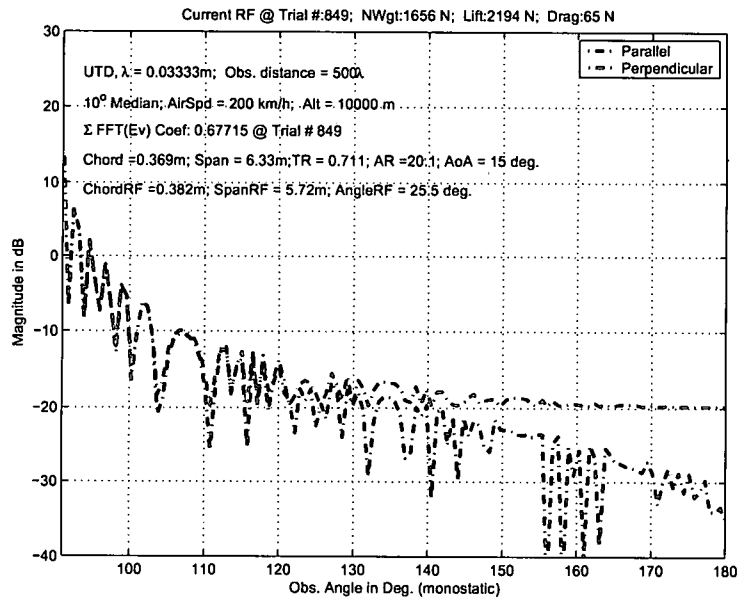


Figure 6.61: Current $\text{Min}(R_i)$ @ $\text{Max}(L_i)$ WRT EM Discipline of a tapered wing; TapProbSet3

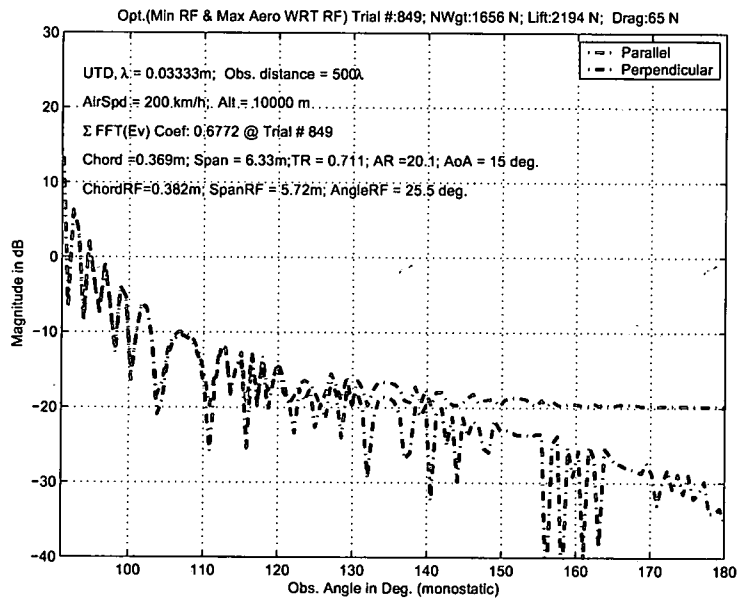


Figure 6.62: Optimal: $\text{Min}(R_i)$ & $\text{Max}(L_i)$ WRT EM Discipline of a tapered wing; TapProbSet3

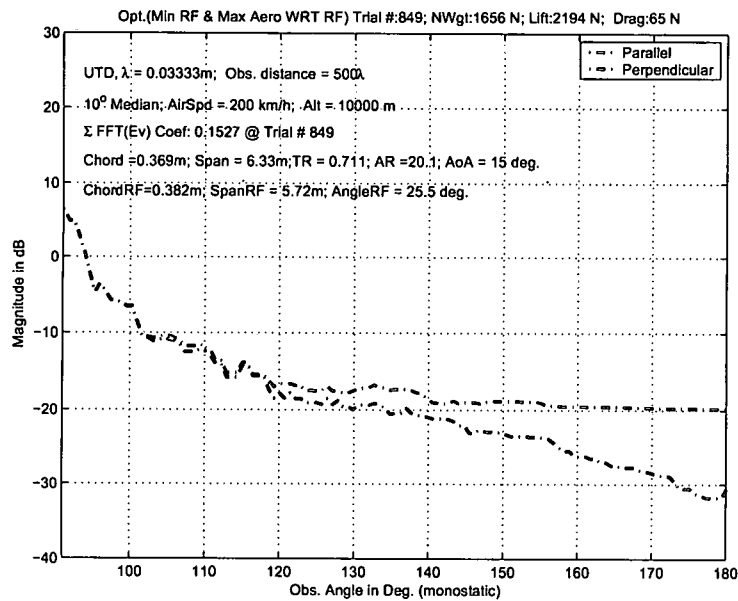


Figure 6.63: Optimal: $\text{Min}(R_i)$ w/10° median & $\text{Max}(L_i)$ WRT EM Discipline of a tapered wing; TapProbSet3

disciplines concurrently, the Aero performance takes the lead role in setting up the lift force threshold.

Comparing the data sets among the rectangular and tapered wing planform in various test cases shown in Tables 6.2, 6.4, 6.6, 6.8, 6.10, and 6.12, one assumption can be made that the rectangular wing planform actually generates less induced drag force than the tapered wing planform under the same environmental parameters, and by increasing the wing aspect ratio, the drag-due-to-lift is reduced, thus improving range for a given wing payload.

Table 6.12: Simulated Tapered Wing Data of TapProbSet3 (Table 6.11)

TapProbSet3	Trial i^{th}	TR	AR	α°	L_i (N)	D_i (N)	γ°	R_i
Run #1	76	0.370	7.49	14.8	2076	145	0	0.077 [‡]
Run #1	646	0.626	19.7	14.9	2187	65	23.0	0.166 [†]
Run #2	3	0.908	20.3	12.1	1808	46	0	0.082 [‡]
Run #2	47	0.351	16.5	14.0	2047	65	10.4	0.220 [†]
Run #3	611	0.501	21.3	14.9	2191	59	0	0.110 [‡]
Run #3	849	0.711	20.1	15.0	2194	65	25.5	0.153 [†]
Run #4	20	0.493	19.1	12.0	1800	44	0	0.199 [‡]
Run #4	117	0.815	14.6	14.1	2058	79	14.8	0.048 [†]
Run #5	22	0.474	2.97	14.1	1803	274	0	0.117 [‡]
Run #5	807	0.728	20.0	14.9	2185	65	28.3	0.298 [†]
Run #6	7	0.512	6.34	12.9	1827	133	0	0.069 [‡]
Run #6	8	0.766	5.22	13.4	1853	168	23.9	0.045 [†]
Run #7	25	0.891	20.3	12.2	1824	46	0	0.073 [‡]
Run #7	507	0.218	16.8	14.9	2175	73	18.5	0.205 [†]
Run #8	30	0.508	7.63	14.8	2027	143	0	0.233 [‡]
Run #8	249	0.700	16.5	14.8	2158	76	8.47	0.051 [†]
Run #9	50	0.254	15.8	13.1	1933	61	0	0.289 [‡]
Run #9	797	0.563	16.8	15.0	2180	74	0.87	0.221 [†]
Run #10	33	0.364	14.1	12.7	1867	63	0	0.363 [‡]
Run #10	192	0.563	15.0	14.8	2154	81	11.4	0.246 [†]

‡ Max L_i & Min R_i with respect to Aero discipline

† Min R_i & Max L_i with respect to EM discipline

CHAPTER 7

CONCLUSION AND ADDITIONAL RESEARCH

Aircraft design and the multidisciplinary optimization among aerodynamics is a complex and computationally intensive problem. Various algorithms, such as Generic Algorithms (GA) and Evolutionary Algorithms (EA) have been utilized to solve complex numerical problems, whereas Multidisciplinary Design Optimization (MDO) is a methodology for the design of complex coupled disciplines [108] in which the synergistic effects yield an optimal solution. Recent high speed data processing tools ease the computational cost for small scale MDO issues. However, large scale MDO remains an issue for complex design problems among those interactive disciplines. In Collaborative Optimization (CO) [109] the traditional approach attempts to collapse the analysis of sub-systems into a single functional block representing the design goal within the framework environment. Multidisciplinary design methodology has been employed in spacecraft design where the system performance depends on the interaction of many disciplines and multiple objectives whose behavior is governed by a large set of design parameters of coupled performance functions. In practical engineering applications, these functions are partitioned or non-linearly decomposed [110] for a large engineering problem into subsets corresponding to various disciplines of the same subject, such as aerodynamics, structural integrity, payload, safety, fuel efficiency, flight mission

controls, weapon system, propulsion, speed, production cost, maintainability, life cycle cost, etc... However, the partitioning process that couples the aerodynamic function and electromagnetic backscattered field return poses a new challenge, in part due to the cross-discipline of two distinctive subjects where the environmental control parameters have more profound effects on Aero performance than the return of the electromagnetic backscattered field.

A complex system often can be represented by the design optimization flow shown in Figure 7.1 involving iterative analysis. The challenges of multidisciplinary design are apparent in the design of spacecraft, a process that involves complex iterative analyses, multiple disciplines associated with a large design space, and great computational expense. Multidisciplinary optimization referred to in this research seeks to obtain a concurrent optimal solution coupled among two distinctive subjects. The analytical data provides a trade-off scenario at the design conceptual stage as well as detail-level input information necessary for a system engineering decision.

The incorporation of the EM discipline early in the context of aerodynamic performance improves the MDO process. The interaction, or the lack thereof, among the electromagnetic (EM) and aerodynamic (Aero) disciplines has been a challenge for high performance aircraft design. The geometrical shape is sensitive to both the EM and Aero disciplines, and design objectives may sometimes conflict with each other. The backscattered field return of a geometrical shape must be taken into consideration early to yield the full benefit of MDO. This paper has illustrated that the coupling effects among the Aero and EM disciplines can be analyzed concurrently using the SMA method. The preliminary data presented in

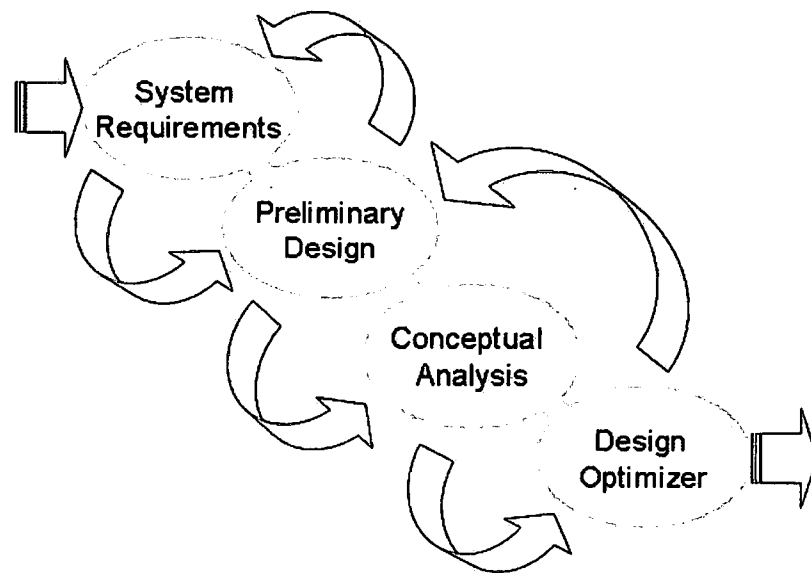


Figure 7.1: System design optimization flow

previous chapter described a simplified geometry wing planform. It provided trade-offs among the aerodynamic and electromagnetic disciplines, and helped to re-define design requirements and constraint conflicts. Also a conceptual missile shape was studied using multi-objective genetic algorithm (MOGA) [111] to determine suitable tradeoffs to maximize the lift-drag ratio and minimize the backscattered field value. The criteria of electromagnetic performance by means of backscattered echo width reduction by shape modification in terms of physical shape, size, orientation, and material, is frequency dependent, whereas the aerodynamic performance is influenced by environmental parameters beyond the wing planform, and added environmental variables increase complexity in optimizing each discipline accurately within the all-in-one MDO approach.

Further study is needed regarding numerical analysis and mathematical methods such as disciplinary and system analysis, investigation in sensitivity analysis [112], the finite difference in the derivation of the independent design variables, the trade-offs on formalized optimization methods, quantitative analysis, and parametric assessment. Advanced information technology plays a vital role in data processing, storage, visualization, and management. Mathematical modelling tools are essential for conceptual design and analysis, conducting trade-off studies, approximation, and sensitivity analysis. A well structured MDO may also include sub-level (hierarchic) decomposition, priority procedures, and concurrent data processing to reduce computation cycle time [113].

In addition to the traditional design process employing mathematical models or engineering decision, MDO provides an alternate method that explores all possible outcomes in designing complex systems [114] with the aid of advanced computing tools and techniques.

Designing a complex engineering system that coherently exploits the mutual benefit (optimal performance outcomes) of coupled interacting disciplines is the primary objective of MDO. The interacting disciplines/phenomena are explored and exploited at all possible stages of the design process. Oftentimes, multi-disciplinary optimization is referred as a design methodology to obtain optimal solutions in various disciplines within the same subject or sector, such as structural integrity, fuel efficiency, payload, safety, maintainability, airspeed, range, etc.

MDO in terms of crossing two or more distinctive subjects or disciplines has posed new challenges in concurrent data processing. High speed computer aided design workstations and powerful signal analysis tools are essential to broadening

MDO development beyond aircraft design. Since many computer programs and data are application specific, integrating programming data and moving them between applications is not practical. Integrated databases would eliminate the need for manual data conversion, a time consuming and error-prone activity. Issues in sharing data between disciplines and within disciplines must be addressed with respect to quality, consistency, and integrity.

7.1 CHALLENGES

Large-scale complex MDO problems involve the coordination of multiple disciplinary simulations or analysis to carry out the interaction among them. The requirements of large-scale MDO analysis are computationally expensive, where a huge number of trials is necessary for analysis of coupled disciplines. Additional hurdles in algorithm software coding, computer aided design (CAD) tools, data interchange format, system integration, and complexity in analytical organization are key issues that need careful planning to ensure compatibility and flexibility.

In addition to many CAD tools and advanced computing machines, the central role of MDO is to enhance the complex design process within the context of a concurrent engineering environment. MDO is not an alternative to traditional knowledge based engineering practice; rather, it complements the human factor and permits large variations in the design of experiments. Multi-fidelity design optimization using relatively inexpensive Multi-Disciplinary Analysis (MDA) for the preliminary conceptual design of supersonic jets [115] has shown promising results. Subspace design approaches or surrogate subsystem models are alternate solutions to resolve many of the computational challenges associated with MDO. Quadratic

programming algorithms [116] show promise in numerical optimizers in parallel processing, but remains a challenge in concurrent MDO.

Progress in the techniques for search and optimization in the design space is also important for the overall effectiveness and efficiency of MDO methodology, as are procedures for tying multiple disciplines together. Increasing the detail analysis will greatly increase the number of iterations required. As a consequence, it requires extra computing power and increased cost. However, investigation into search techniques, such as search with analysis, sensitivity analysis, approximate analysis, etc... will improve the optimization process among multiple disciplines in identifying multiple local maxima and minima.

In practical applications, MDO needs to satisfy design requirements of accuracy in multi-objective solutions and affordability. The constraint in inequality variable constraints and parametric models for conceptual design may be problematic for high fidelity complex systems. Despite the availability of high-speed computing machines and algorithms in fine-tuning MDO processes, high-performance aircraft design and the concepts of coupling the aerodynamic discipline to include electromagnetic solution and the integration aspects remain the greatest challenge. The quest to develop an optimization algorithm that is suitable for general applications is a challenging task in the context of design optimization.

The most challenging task with respect to the EM discipline would be the difficulty in solving Maxwell's equations boundary conditions, geometry description, physical size, and orientation of an electrically large object. The computation or prediction of backscattered field of an air vehicle at X-band (8 - 12 GHz) is feasible but computationally intensive.

7.2 CONTRIBUTIONS

Due to the needs driving a new methodology to meet the requirements for a robust MDO in future spacecraft design, ASTROS [8] was developed for airframe design that includes integration of aerodynamics, structures, controls, and mathematical optimization. Bringing an electromagnetic solution, or the return of backscattered field, into wing planform design constitutes an expansion of the scope of MDO. The development of MDO is not strictly limited to the aerospace industry; the utility can be expanded to marine systems, propulsion systems, the automotive industry, smart structures development, and many other military applications.

During the course work of MDO, it was noted that having a formal system configuration would be beneficial in the process of optimization; knowledge increases with time, and the freedom to act on that knowledge decreases with time. The prudence of a robust design lies in the attribute of preventing problems from occurring late in the service cycle which may be too costly to correct. The MDO design structure employing the mutation method embedded in the algorithm can be utilized as a problem solving tool to troubleshoot a given particular solution set that yields an undesirable performance function (ie: low-cost in production yields a high life service cycle cost). An optimal robust design should prevent problems from occurring late in the product that may sometimes be futile to correct.

Mathematical approximation [117] in the engineering process of optimization utilizing stochastic algorithm (SA) provides design flexibility, which is essential for large-scale MDO and high priority disciplines where organization structure for high speed computing machines, database format, functional/mathematical model compatibility, and system integration are crucial components in MDO concurrent

processes. In addition, approximation mitigates the computational expense issues of using high-fidelity models in optimization.

A mutation technique utilizing Genetic Algorithm [118] depicts the convergence of performance function becomes monotonic. Unlike Genetic Algorithms which mimic evolution's selection on offspring crossover, SMA evaluates design space at each trial, and derives a converged optimal solution. Aircraft design is engineering a system whose performance depends on the interaction of many disciplines and is governed by a large design space of coupled equations corresponding to the Aero and EM disciplines. Clearly, the goal of multidisciplinary integration is to reduce system development time and lower cost while attaining a broader selection of optimized alternative solutions to the traditional design process.

A review of current development in numerical analysis and design methodology has shown great improvement in design optimization processes. The objective of this paper is to augment MDO process by deriving a technique for cross-discipline numerical analysis to complex problems with the goal of enhancing the design process and improving efficiency. The framework of MDO has greatly extended optimization algorithms, including concurrent subspace optimization (CSSO) [119], the ability to handle multi-objective optimization problems in MDO, Collaborative Optimization (CO) [120] for loosely coupled MDO problems, and Multidisciplinary Feasible (MDF) approach in multidisciplinary design synthesis.

APPENDIX A

SOFTWARE CODES

A.1 Fresnel Integral

$$f(t) = \int_0^u \frac{e^{-jt}}{\sqrt{2\pi t}} dt \quad (\text{A.1})$$

```
function y = fresnel(u)
```

```
a = [1.595769140; 0.000001702; -6.808568854; -0.000576361;  
     6.920691902; -0.016898657; -3.050485660; -0.075752419;  
     0.850663781; -0.025639041; -0.150230960; 0.0344044779];
```

```
b = [-0.000000033; 4.255387524; -0.000092810; -7.7800204;  
     -0.009520895; 5.075161298; -0.138341947; -1.363729124;  
     -0.403349276; 0.702222016; -0.216195929; 0.019547031];
```

```
c = [0.000000000; -0.024933975; 0.000003936; 0.005770956;  
     0.000689892; -0.009497136; 0.011948809; -0.006748873;  
     0.000246420; 0.002102967; -0.001217930; 0.000233939];
```

```
d = [0.199471140; 0.000000023; -0.009351341; 0.000023006;  
     0.004851466; 0.001903218; -0.017122914; 0.029064067;  
     -0.027928955; 0.016497308; -0.005598515; 0.000838386];
```

```
ab = a + j*b;
```

```
cd = c + j*d;
```

```
m=length(u);
```

```

y=[ ];
for m1=1:m;
    uma = u(m1);
    if uma<=4
        ua = .25*uma;
        ca = sqrt(ua).*exp(-j*uma);
        ub = ua;
        ur=[1];
        for k = 1:11;
            ur = [ur; ub];
            ub = ub.*ua;
        end
        ra = ab.'*ur;
        y1 = ca*ra;
    else
        ua = 4./uma;
        ca = sqrt(ua).*exp(-j*uma);
        ub = ua;
        ur=[1];
        for k = 1:11;
            ur = [ur; ub];
            ub = ub.*ua;
        end
        ra = cd.'*ur;
        y1 = .5*(1-j)+ca.*ra;
    end
    y=[y y1];
end

```

A.2 Induced Drag Factor

$$\sigma = \sum_2^N n \left(\frac{A_n}{A_1} \right)^2 \geq 0 \quad (\text{A.2})$$

```

rad=pi/180;
phi=90;
alp=15;
p=256;
s=10;
C4=2;
b=4;
alphaL=-1.20;
ao=2*pi;

for m=1:p
    cr(m)=C4/(1+m/p);
    ct(m)=cr(m)*m/p;
    lam4(m)=ct(m)/cr(m);
    c(m)=0.5*cr(m)*(1+lam4(m));
    AR4(m)=(b^2)/(b*c(m));
    Ao(m)=ao/(1+(ao/pi*AR4(m))*(1+.25));
    alpha(m)=m/p*alp;
    alphaD(m)=alpha(m);

    for n=1:s

        mu(n)=(ao/(2*(1+lam4(m))*AR4(m)))*[1+(lam4(m)-1)*...
            cos(n/s*phi*rad)];
        X(n)=mu(n)*((alpha(m)-alphaL)*rad)*sin(n/s*phi*rad);
        A1(n)=sin(1*n/s*phi*rad)*(1*mu(n)+sin(n/s*phi*rad));
        A2(n)=sin(3*n/s*phi*rad)*(3*mu(n)+sin(n/s*phi*rad));
        A3(n)=sin(5*n/s*phi*rad)*(5*mu(n)+sin(n/s*phi*rad));
        A4(n)=sin(7*n/s*phi*rad)*(7*mu(n)+sin(n/s*phi*rad));
        A5(n)=sin(9*n/s*phi*rad)*(9*mu(n)+sin(n/s*phi*rad));
        A6(n)=sin(11*n/s*phi*rad)*(11*mu(n)+sin(n/s*phi*rad));
        A7(n)=sin(13*n/s*phi*rad)*(13*mu(n)+sin(n/s*phi*rad));
        A8(n)=sin(15*n/s*phi*rad)*(15*mu(n)+sin(n/s*phi*rad));
        A9(n)=sin(17*n/s*phi*rad)*(17*mu(n)+sin(n/s*phi*rad));
        A10(n)=sin(19*n/s*phi*rad)*(19*mu(n)+sin(n/s*phi*rad));
    end

    A=[A1;A2;A3;A4;A5;A6;A7;A8;A9;A10];
    An=X/A;
    Aa=An(1)^2;
    sig4(m)=(3*An(2)^2/Aa)+(5*An(3)^2/Aa)+(7*An(4)^2/Aa)+...
        (9*An(5)^2/Aa)+(11*An(6)^2/Aa)+(13*An(7)^2/Aa)+...
        (15*An(8)^2/Aa)+(17*An(9)^2/Aa)+(19*An(10)^2/Aa);

```

```

cl4(m)=An(1)*pi*AR4(m);
Cl4(m)=cl4(m)/(1+cl4(m)/(pi*AR4(m)));
Cd4(m)=[Cl4(m)^2/(pi*AR4(m))]*(1+sig4(m));
Cld4(m)=sqrt(Cd4(m)*(pi*AR4(m))/(1+sig4(m)));

end

```

A.3 Geometrical Optics / Geometrical Theory of Diffraction

```

f=12e9;
c=3e8;
lambda=c/f;
ko=2*pi/lambda;
d=3*lambda;
n=2;
phi=75;
pts=361;
b1=[exp(-i*(ko*d+(pi/4)))*(1/n)]/(sqrt(2*pi*ko*d));

for q=1:pts;
    Vdi(q)=b1*sin(pi/n)/[cos(pi/n)-cos((2*pi/n)*((q-1)-phi)/pts)];
    Vdr(q)=b1*sin(pi/n)/[cos(pi/n)-cos((2*pi/n)*((q-1)+phi)/pts)];
    Voi(q)=exp(i*ko*d*cos(2*pi*((q-1)-phi)/pts));
    Vor(q)=exp(i*ko*d*cos(2*pi*((q-1)+phi)/pts));
end

for r=1:pts;

    if r < 105;
        V1(r)=Vdi(r)+Vdr(r)+Voi(r)+Vor(r);
        Vd1(r)=Vdi(r)+Vdr(r);
    else
        V1(r)=0;
        Vd1(r)=0;
    end

    if r==105;

```

```

        V1a(r)=5;
        Vd1a(r)=5;
    else
        V1a(r)=0;
        Vd1a(r)=0;
    end

    if (105 < r) & (r < 255);
        V2(r)=Vdi(r)+Vdr(r)+Voi(r);
        Vd2(r)=Vdi(r)+Vdr(r);
    else
        V2(r)=0;
        Vd2(r)=0;
    end

    if r==255;
        V2a(r)=5;
        Vd2a(r)=5;
    else
        V2a(r)=0;
        Vd2a(r)=0;
    end

    if r > 255;
        V3(r)=Vdi(r)+Vdr(r);
        Vd3(r)=Vdi(r)+Vdr(r);
    else
        V3(r)=0;
        Vd3(r)=0;
    end
end

Vt=V1+V1a+V2+V2a+V3;
Vd=Vd1+Vd1a+Vd2+Vd2a+Vd3;

```

BIBLIOGRAPHY

- [1] R. Ross, "Radar cross section of rectangular flat plates as a function of aspect angle," *IEEE Transactions of Antenna and Propagation*, vol. AP-14, pp. 392-335, May 1966.
- [2] J. Bertin, *Aerodynamics for Engineers*. Prentice-Hall, 4th ed., 2002.
- [3] P. Hanley, *3D Air Foil Analysis Tools*. www.3DFoil.com, 2005.
- [4] B. McCormick, *Aerodynamics, Aeronautics and Flight Mechanics*. John Wiley and Sons, 2nd ed., 1995.
- [5] J. Korte, R. Weston, and T. Zang, "Multidisciplinary optimization methods for preliminary design," in *ADARD Interpanel Symposium*.
- [6] J. Walsh, K. Young, J. Pritchard, H. Aelman, and W. Mantay, "Multilevel decomposition approach to integrated aerodynamic/dynamic/structural optimization of helicopter rotor blades," in *American Helicopter Society Aeromechanics Specialists Conference: San Francisco, California.*, January 19-21 1994.
- [7] J. Sobieszczanski-Sobieski and R. Haftka, "Multidisciplinary aerospace design optimization: Survey of recent developments," in *34th AIAA Aerospace Sciences Meeting and Exhibit: Reno, Nevada.*, vol. AIAA Paper No. 96-071, January 15-18 1996.
- [8] V. Venkayya, D. Neill, and D. Herendeen, "Astros enhancements," usaf, contract no. f33615-87-3216, Wright Laboratory, Wright Patterson Air Force Base, May 1995.
- [9] I. Kroo, S. Altus, R. Braun, P. Gage, and I. Sobieski, "Multidisciplinary optimization methods for aircraft preliminary design," in *5th AIAA/USAF/NASA/ISSMO Symposium on Multidisciplinary Analysis and Optimization: Panama City, Florida.*, September 7-9 1994.

- [10] J. Weston, J. Townsend, T. Eidson, and R. Gates., "A distributed computing environment for multidisciplinary design," in *5th AIAA/USAF/NASA/ISSMO Symposium on Multidisciplinary Analysis and Optimization: Panama City, Florida.*, vol. AIAA 94-4372, September 7-9 1994.
- [11] I. Kroo, S. Altus, R. Braun, P. Gage, and I. Sobieski, "Multidisciplinary optimization methods for aircraft preliminary design," in *5th AIAA/USAF/NASA/ISSMO Symposium on Multidisciplinary Analysis and Optimization*, Sept. 1994.
- [12] R. Grandhi, G. Bharatram, and V. Venkayya, "Multiobjective optimization of large-scale structures," *AIAA Journal*, vol. 31, No. 7, July 1993.
- [13] R. Unal, "Multidisciplinary design optimization using genetic algorithms," *1994 NASA-HU American Society for Engineering Education (ASEE) Summer Faculty Fellowship Program: Hampton University*, December 1994.
- [14] P. Frank, A. Booker, T. Caudell, and M. Healy., "A comparison of optimization and search methods for multidisciplinary design," in *4th AIAA/USAF/NASA/OSI Symposium on Multidisciplinary Analysis and Optimization: Cleveland, Ohio*, September 21-23 1992.
- [15] C. Reddy and M. Deshpande, "Application of awe for rcs frequency response calculation using method of moment," *NASA CR-4758*, October 1996.
- [16] C. Cockrell and F. Beck, "Asymptotic waveform evaluation technique (awe) for frequency domain electromagnetic analysis," *NASA TM*.
- [17] C. Reddy and M. Deshpande, "Application of awe along with a combined fem/mom technique to compute rcs of a cavity-backed aperture in an finite ground plane over a frequency range," *NASA CR-97-206261*, December 1997.
- [18] C. Reddy, "Application of model based parameter estimation for rcs frequency response," *NASA CR-1998-206951*, March 1998.
- [19] C. Furse, O. Ghandi, and S. Mathur, "Improvements to the finite difference time domain method for calculating the radar cross section of a perfectly conducting target," *IEEE Transactions on Microwave Theory and Techniques*, vol. 38, pp. 919-927, July 1990.
- [20] J. Volakis, A. Chatterjee, D. Ross, M. Casciato, and J. Gong, "Electromagnetic characterization of aircraft scattering and antennas," tech. rep., University of Michigan, 1994-95.

- [21] O. James and V. Venkayya, "Finite element models of usaf aircraft structures," in *AFWAL, Proceedings of the 1987 Aircraft/Engine Structural Integrity Program Conference*, 1987.
- [22] J. Sobieszczanski-Sobieski and R. Haftka, "Multidisciplinary aerospace design optimization: Survey of recent developments," in *34th AIAA Aerospace Sciences Meeting and Exhibit*, Jan. 1996.
- [23] V. Venkayya, "Structural optimization - a review and some recommendations," *International Journal for Numerical Methods in Engineering*, vol. 13, No 2, Pg 203-228, May 1978.
- [24] L. Rowell, R. Braun, J. Olds, and R. Unal, "Multidisciplinary conceptual design optimization of space transportation systems," *Journal of Aircraft*, vol. 36, No 1, Pg 218-226, 1999.
- [25] S. Obaysashi, D. Sasaki, Y. Takeguchi, and N. Hirose, "Multiobjective evolutionary computation for supersonic wing-shape optimization," *IEEE Transaction on Evolutionary Computation*, vol. 4, No 2, Pg 182-187, July 2000.
- [26] K. Hulme and C. Bloebaum, "A comparison of solution strategies for simulation-based multidisciplinary design optimization," in *7th AIAA/NASA/ISSMO Symposium on Multidisciplinary Analysis and Optimization*, Sept. 1998.
- [27] E. Cramer, J. D. Jr., P. Frank, R. Lewis, and G. Shubin, "Problem formulation for multidisciplinary optimization," *SIAM Journal of Optimization*, vol. 4, No 4, Pg 754-776, Nov. 1994.
- [28] R. Haftka, J. Sobieszczanski-Sobieski, and S. Padula, "On options for interdisciplinary analysis and design optimization," *SIAM Journal of Optimization*, vol. 4, No 2, Pg 65-74, June 1992.
- [29] E. Cramer, P. Frank, G. Shubin, and J. D. Jr., "On alternative problem formulations for multidisciplinary design optimization," in *4th AIAA/USAF/NASA/OAI Symposium on Multidisciplinary Analysis and Optimization*, Sept. 1992.
- [30] Q. Chen and J. Dai, "Distributed coevolutionary multidisciplinary design optimization: A flexible approach," in *9th AIAA/ISSOM Symposium on Multidisciplinary Analysis and Optimization*, Sept. 2002.
- [31] J. Sobieszczanski-Sobieski, S. Kodiyalam, and R. Yang, "Optimization of car body under constraints of noise, vibration, and harshness (nvh), and crash,"

in *41st AIAA/ASME/ASCE/AHS/ASC Structures, Structural Dynamics, and Materials Conference and Exhibit*, April 2000.

- [32] S. Hong, G. Thiele, and V. Venkayya, "Computation of radar cross section with the coupling of aerodynamic performance in a multidisciplinary design optimization of aircraft," in *AIAA, 24th Annual Dayton-Cincinnati Aerospace Science Symposium*, April 1999.
- [33] F. Rabinowitz, "A stochastic algorithm for global optimization with constraints," *ACM Transactions on Mathematical Software*, vol. 21, Issue 2, Pg 194-213, June 1995.
- [34] J. Nelder and R. Mead, "A simplex method for function minimization," *The Computer Journal*, vol. 7, Pg 308-313, 1965.
- [35] S. Masri, G. Bekey, and F. Safford, "Global optimization algorithm using adaptive random search," *Applied Mathematic and Computer*, vol. 7, No. 4, Pg 353-376, 1980.
- [36] A. Corana, M. Marchesi, C. Martini, and S. Ridella, "Minimizing multimodal function of continuous variables with the,"
- [37] S. Hong, R. Kissell, and R. McRaven, "Stochastic algorithm improves electronic counter/countermeasures development and attains jamming waveform optimization," in *16th Annual Electronic Combat Technical Interchange Meeting*, Nov. 2003.
- [38] C. Balanis, *Advanced Engineering Electromagnetics*. John Wiley and Sons, 1989.
- [39] W. Stutzman and G. Thiele, *Antenna Theory and Design*. John Wiley and Sons, 1981.
- [40] C. Balanis, *Antenna Theory: Analysis and Design*. John Wiley and Sons, 1982.
- [41] R. Harrington, *Field Computation by Moment Methods*. New York: Macmillan, 1968.
- [42] K. Yee, "Numerical solution of initial boundary value problems involving maxwell's equations in isotropic media.," *IEEE Transactions on Antenna and Propagation*, May 1966.
- [43] B. Engquist and A. Majda, "Radiation boundary conditions for acoustic and elastic wave calculations," *Commun. Pure Appl. Math.*, vol. 32, pp. 313-357, 1979.

- [44] G. Mur, "Absorbing boundary conditions for finite difference approximation of the time domain electromagnetic field equations," *IEEE Transactions on Electromagnetic Compat.*, vol. EMC, pp. 1073-1077, 1981.
- [45] K. Yee, J. Chen, and A. Chang, "Conformal finite difference time domain with overlapping grids," *IEEE Transactions on Antenna and Propagation*, vol. AP-40, no. 9, pp. 1068-1075, 1992.
- [46] A. Taflov, K. Umashankar, and T. Jurgens, "Validation of fd-td modelling of the radar cross section of three-dimensional structures spanning up to nine wavelengths," *IEEE Transactions on Antenna and Propagation*, vol. 33, pp. 662-666, 1985.
- [47] P. Silvester, "Finite-element solution of homogeneous waveguide problems," *Alta Frequenza*, vol. 38, Pg 313-317, 1969.
- [48] J. Wu and B. Jiang, "A least-squares finite element method for electromagnetic scattering problems," in *NASA CR-202313*, Dec. 1996.
- [49] M. Botha and J. Jin, "Adaptive finite element-boundary integral analysis for electromagnetic fields in 3-d," *IEEE, Transactions on Antennas and Propagation*, vol. 53, No 5, Pg 1710-1720, May 2005.
- [50] J. Webb, "Finite element analysis of dispersion in waveguides with sharp metal edges," *IEEE, Transactions on Microwave Theory and Techniques*, vol. 36, Pg 1819-1824, 1998.
- [51] Z.J. Cendes and P. Silvester, "Numerical solution of dielectric loaded waveguides: I -finite element analysis," *IEEE, Transactions on Microwave Theory and Techniques*, vol. MTT-18, Pg 1124-1131, 1970.
- [52] A. Peterson and R. Baca, "Error in the finite element discretization of the scalar helmholtz equation over electrically large regions," *IEEE, Microwave and Guided waves Letters*, vol. 1, Pg 219-222, 1991.
- [53] P. Ufimtsev, "Approximate computation of diffraction of plane electromagnetic waves at certain metal bodies: Part i. diffraction patterns at a wedge and a ribbon," *Zh. Tekhn. Fiz. (USSR)*, vol. 27, no. 8, pp. 1708-1718, 1957.
- [54] J. Keller, "The geometrical theory of diffraction," in *Proc. Symposium on Microwave Optics: Eaton Electronics Research Laboratory, McGill University, Montreal, Canada.*, June 1953.
- [55] J. Keller, "The geometrical theory of diffraction," *Journal Optical Society of America*, vol. 52, no. 2, pp. 116-130, February 1962.

- [56] R. Kouyoumjian and P. Pathak, "A uniform geometrical theory of diffraction for an edge in perfectly conducting surface," *Proc. IEEE*, vol. 62, pp. 1448-1461, November 1974.
- [57] S. Lee, "Comparison of uniform asymptotic theory and ufmtsev's theory of em diffraction," *IEEE Transactions on Antenna and Propagation*, vol. AP-25, no. 2, pp. 162-170, 1977.
- [58] Y. Lo and S. Lee, *Antenna Handbook: Theory, Applications, and Design*. Van Nostrand Reinhold Company, 1988.
- [59] R. Kouyoumjian, "Asymptotic high-frequency methods," *Proc. IEEE*, vol. 53, pp. 864-876, August 1965.
- [60] P. Russo, R. Rudduck, and J. L. Peters, "A method for computing e-plane pattern of horn antenna," *IEEE Transactions on Antenna and Propagation*, vol. AP-13, pp. 219-224, 1965.
- [61] A. Sommerfield, *Optics*. New York: Academic Press, 1954.
- [62] W. Pauli, "On asymptotic series for functions in the theory of diffraction of light," *Phys. Rev.*, vol. 54, pp. 924-931, 1938.
- [63] J. Keller, "Diffraction by an aperture," *Journal Applied Physics*, vol. 28, pp. 426-444, April 1957.
- [64] S. Karp and J. Keller, "Multiple diffraction by an aperture in a hard screen," *OPTICA ACTA (Paris)*, vol. 8, pp. 61-72, January 1961.
- [65] L. McCuller, "Aircraft configuration optimization including optimized flight profiles," *NASA, Langley Research Center, Recent Experiences in Multidisciplinary Analysis and Optimization*, pp. Part 1, 18, 1984.
- [66] W. C. Engelund, D. O. Stanley, R. A. Lepsch, M. M. McMillin, and R. Unal, "Aerodynamic Configuration Design Using Response Surface Methodology Analysis," *NASA STI/Recon Technical Report A*, vol. 94, Aug. 1993.
- [67] R. Stengel, *Flight Dynamics*. Princeton University Press, 2004.
- [68] J. Anderson, *Fundamentals of Aerodynamics*. McGraw-Hill Co., 2nd ed., 1984.
- [69] J. Bertin and M. Smith, *Aerodynamics for Engineers*. Prentice-Hall, 2nd ed., 1989.
- [70] J. Anderson, *Introduction to Flight*. McGraw-Hill Book Co., 3rd ed., 1990.

- [71] C. Dole and J. Lewis, *Flight Theory and Aerodynamics*. John Wiley and Sons, 2000.
- [72] J. Katz and A. Plotkin, *Low-Speed Aerodynamics*. Cambridge University Press, 2000.
- [73] M. Cook, *Flight Dynamics Principles*. John Wiley and Sons, 1997.
- [74] C. A. Martin and D. H. Thompson, "Scale Model Measurements of Fin Buffer due to Vortex Bursting on F/A-18," *AGARD Manoeuvring Aerodynamics*, Nov. 1991.
- [75] I. Abbott and A. von Doenhoff, *Theory of Wing Sections*. Dover Publication, 4th ed., 1949.
- [76] J. Sivells, "Experimental and calculated characteristics of three wings of naca 64-210 and 65-210 airfoil sections with and without washout," *TN 1422, National Advisory Committee for Aeronautics*, 1947.
- [77] H. Glauert, *The Elements of Aerofoil and Airscrew Theory*. Cambridge University Press, 1926.
- [78] A. Kuethe and C. Chow, *Fundations of Aerodynamics*. John Wiley and Sons, 3rd ed., 1976.
- [79] S. Hoerner, *Fluid-Dynamic Drag*. Practical Information on Aerodynamic Drag and Hydrodynamic Resistance, 1965.
- [80] S. Obayashi, "Multidisciplinary design optimization of aircraft wing planform based on evolutionary algorithms," in *IEEE International Conference on Systems, Man, and Cybernetics, USA*, Oct. 1998, pg 3148-3153, vol. 4.
- [81] E. Taylor, "Evaluation of multidisciplinary design optimization techniques as applied to spacecraft design," in *IEEE Aerospace Conf. Proceedings, USA*, March 2000, pg 371-384, vol. 1.
- [82] D. Shi, J. Yin, G. Chen, and J. Dong, "A workflow-based distributed multidisciplinary design optimization framework," in *The 9th International Conference on Computer Supported Cooperative Work in Design Proceedings*, May 2005, pg 497-502, vol. 1.
- [83] T. Coleman and Y. Li, *Large-Scal Numerical Optimization*. October 1989.
- [84] W. Chen and K. Lewis, "Robust design approach for achieving flexibility in multidisciplinary design," in *7th AIAA/USAF/NASA/ISSMO Symposium on Multidisciplinary Analysis and Optimization*, Sept 1998, pg 1833-1842.

- [85] J. Sobieszcanski-Sobieski, "Optimization by decomposition: A step from hierarchic to non-hierarchic systems," in *2nd NASA/USAF Symposium on Recent Advances in Multidisciplinary Analysis and Optimization*, Sept 1989, pg 51-78.
- [86] J. Balling and J. Sobieszcanski-Sobieski, "An algorithm for solving the system-level problem in multilevel optimization," in *5th AIAA/USAF/NASA/ISSMO Symposium on Multidisciplinary Analysis and Optimization*, Sept 1994, pg 794-809.
- [87] C. Nelson, "Effects of wing planform on hsct off-design aerodynamics," *10th AIAA Applied Aerodynamic Conference*, June 1992.
- [88] S. Obayashi, T. Tsukahara, and T. Nakamura, "Multiobjective genetic algorithm applied to aerodynamic design of cascade airfoils," *IEEE Transaction on Electronics*, vol. 47, No.1 Pg 211-216, Feb. 2000.
- [89] K. Chiba, S. Obayashi, K. Nakahashi, and H. Morino, "High-fidelity multidisciplinary design optimization of aerostructural wing shape for regional jet," in *23rd AIAA Applied Aerodynamics Conference*, June 2005.
- [90] S. Obayashi, K. Nakahashi, A. Oyama, and N. Yoshino, "Design optimization of supersonic wings using evolutionary algorithms," in *4th ECCOMAS Computational Fluid Dynamics Conference*, Sept. 1998.
- [91] D. Sasaki, S. Obayashi, and K. Nakahashi, "Navier-stokes optimization of supersonic wings with four objectives using evolutionary algorithm," *Journal of Aircraft*, vol. 39, No. 4 Pg 621-629, 2002.
- [92] S. Obayashi, D. Sasaki, and Y. Takeguchi, "Evolutionary computation of supersonic wing shape optimization," in *4th ECCOMAS Computational Fluid Dynamics Conference*, Sept. 1998.
- [93] S. Wakayama and I. Kroo, "Subsonic wing planform design using multidisciplinary optimization," *Journal of Aircraft*, vol. 32, No 4, Pg 746-753, 1995.
- [94] E. Jumper, S. Schreck, and R. Dimmick, "Life-curve characteristics for an airfoil pitching at constant rate," *AIAA, Journal of Aircraft*.
- [95] J. Spreiter and A. Alksne, "Thin airfoil theory based on approximate solution of the transonic flow equation," *NACA Report 1359*, 1958.
- [96] M. Drela, "Low-reynolds-number airfoil design for the m.i.t. daedalus prototype: A case study," *AIAA, Journal of Aircraft*, vol. 25, No 8, Dec 1987.

- [97] W. Houston, "The viscosity of air," *The American Physical Society*, August 1937.
- [98] B. Thurow, M. Samimy, and W. Lempert, "Compressibility effects on turbulence structures of axisymmetric mixing layers," *Physics of Fluids*.
- [99] E. Arian and V. Vatsa, "A preconditioning method for shape optimization governed by the euler equations," *NASA/CR 1998-206926 ICASE Report No. 98-14*, February 1998.
- [100] A. Jameson, "Aerodynamic design via control theory," *Journal of Scientific Computing*, vol. 3, No 3, Sept. 1988.
- [101] J. Sacks, W. Welch, T. Mitchell, and H. Wynn, "Design and analysis of computer experiments," in *Statistical Science, Vol 4, No 4*, 1989, pg 409-435.
- [102] L. Yuan, C. Teng, and S. Kang, "Statistical estimation of average power dissipation in sequential circuits," in *34th ACM IEEE Design Automation Conference*, Sept 1997, pg 377-382.
- [103] C. Huang and C. Bloebaum, "Multi-objective pareto concurrent subspace optimization for multidisciplinary design," *42th AIAA Aerospace Sciences Meeting and Exhibit*, Jan. 2004.
- [104] M. DeHaan, "Induced drag of wings with highly swept and tapered wing tips," in *AIAA, 8th Applied Aerodynamics Conference*, Aug. 1990.
- [105] I. Kroo, "Drag due to lift concept for prediction and reduction," *Annual Review of Fluid Mechanics*, vol. 33, Pg 587-617, July. 2001.
- [106] S. Smith and I. Kroo, "Computation of induced drag for elliptical and crescent-shaped wings," *AIAA Journal of Aircraft*, vol. 30, Pg 446-452, July. 1993.
- [107] J. Horn, N. Nafplitis, and D. Goldberg, "A niched pareto genetic algorithm for multiobjective optimization," *1st IEEE Conference on Evolutionary Computation Proceedings*, vol. 1, Pg 82-87, June 1994.
- [108] R. Balling and J. Sobieszczanski-Sobieski, "Optimization of coupled systems: A critical overview of approaches," *AIAA Journal*, vol. 34, No 1, pg 6-17, 1996.
- [109] C. McCallister, T. Simpson, and M. Yukish, "Goal programming applications in multidisciplinary design optimization," in *8th AIAA/NASA/USAF/ISSMO Symposium on Multidisciplinary Analysis and Optimization*, Sept 2000.

- [110] G. Wrenn and A.R.Dovi, "Multilevel decomposition approach to the preliminary sizing of a transport aircraft wing," *AIAA Journal of Aircraft*, vol. 25, No 7, pg 632-638, July 1988.
- [111] L. Hong, "Multiobjective evolutionary computation for noncircular missile shape optimization," *42th AIAA Aerospace Sciences Meeting and Exhibit*, Jan. 2004.
- [112] J. Sobieszczanski-Sobieski, "Sensitivity analysis and multidisciplinary optimization for aircraft design: Recent advances and results," *International Council for Aeronautical Science*, vol. volume 2, pp. pg 963-964, Aug.-Sept. 1988.
- [113] J. Rogers, "Reduceing design cycle time and cost through process resquencing," in *11th International Conference on Engineering Design*, Aug 1997.
- [114] J. Rogers, "Tools and techniques for decomposing and managing complex design projects," *AIAA Journal of Aircraft*, vol. 36, No 1, pg 266-274, Jan 1999.
- [115] S. Choi, J. Alonso, S. Kim, and I. Kroo, "Two-level multi-fidelity design optimization studies for supersonic jets," in *43rd AIAA Aerospace Sciences Meeting and Exhibit*, Jan. 2005.
- [116] P. Gill, W. Murray, and M. Wright, *Practical Optimization*. Academic Press, 1981.
- [117] N. Alexandrov, "On using approximations in engineering optimization," in *16th International Symposium Mathematical Programming*, Aug 1997.
- [118] S. Hong, R. Kissell, and R. McRaven, "Utilizing genetic algorithm mutation technique in the context of multidisciplinary design optimization of aerodynamic performance and radar cross section of aircraft," in *AIAA, 25th Annual Dayton-Cincinnati Aerospace Science Symposium*, March 2000.
- [119] J. Renaud and G. Gabriele, "Improved coordination in non-hierarchic system optimization," *AIAA Journal*, vol. 31, No. 12, Pg 2367-2373, 1993.
- [120] R. Braun, A. Moore, and I. Kroo, "Use of the collaborative optimization architechture for launch vehicle design," in *6th AIAA/USAF/NASA/ISSMO Symposium on Multidisciplinary Analysis and Optimization*, Sept. 1996.

VITA

Seng Muy Hong was born on April 25, 1957 in Canton, China. In 1958, his family escaped from the Communist China and resided in Phnom Penh, Cambodia till 1975. Mr. Hong survived the Khmère Rouge Regime period 1975 - 1979 and migrated to United States in August 1979 as a refugee from Cambodia.

Mr. Hong, a registered Professional Engineer (P.E.), is currently employed by the Air Force Research Laboratory (AFRL), Radio Frequency (RF) Sensors Technology Division (AFRL/SNR), conducting electronic warfare (EW) countermeasures techniques assessment at Wright-Patterson Air Force Base, Ohio. Mr. Hong came to AFRL in October 2002 with 17 years of experience as a defense contractor.

Mr. Hong and his wife came to Louisville, Mississippi, as refugees from Cambodia in August 1979. He began his education at a local high school at night to study English and received his General Educational Development (GED) certificate in June 1981. He attended Wood Junior College at Mathiston, MS, studying English composition and other college preparatory courses from August 1981 to July 1982 part-time while working full-time at Taylor Machine Works in Louisville, MS. In August 1982, Mr. Hong attended Mississippi State University (MSU) and received his B.S.E.E. in December 1985 while holding three part-time jobs, including a Courier Service for a local regional Merchant & Farmers Bank. His senior class research project was to design and construct a Transverse Electromagnetic (TEM) cell for measuring the interference and susceptible radiation of electromagnetic waves of electronic devices.

Mr. Hong continued his graduate course work in January 1986 at University of Texas at Arlington and Southern Methodist University while employed at General Dynamics (Fort Worth Division). In January 1990 he was promoted to Senior Hardware Design Engineer in the EW Simulation Design Group, leading a \$2M plus hardware project. In February 1991, Mr. Hong relocated to Dayton and worked for MacAulay-Brown, Inc. (MacB), a defense contractor/consultant company. He matriculated at University of Dayton in August 1991, and received his M.S.E.E. concentrated in electromagnetic and microwave engineering in May 1994. His

M.S.E.E. thesis was to develop and implement a non-real time homogenous clutter signal generator, sponsored in part by Tyndall Air Force Base.

While working as a defense contractor/consultant at MacB, Mr. Hong continued his graduate studies towards a Ph.D. in Electrical Engineering in electromagnetics, antenna design and theory, and radar cross section computation. In October 2002, Mr. Hong accepted a research position with AFRL, Sensors Directorate and leads a technical staff conducting in-house research & development activities at the Radio Frequency Countermeasures Test Facility. He expects to complete his Ph.D. research and graduate in May 2006.

R702032632

The HF Group

Indiana Plant

T 052546 F 19 00



6/8/2006